

Material Characterization of InGaAs/InP PIN Photodetectors

By

Pit Ho Patrio Chiu

Electrical & Computer Engineering Department McGill University, Montreal, Canada

July 2002

A thesis submitted to the Faculty of Graduate Studies and Research in partial fulfillment of the requirements of the degree of Master of Engineering



National Library of Canada

Acquisitions and Bibliographic Services

395 Wellington Street Ottawa ON K1A 0N4 Canada Bibliothèque nationale du Canada

Acquisisitons et services bibliographiques

395, rue Wellington Ottawa ON K1A 0N4 Canada

> Your file Votre référence ISBN: 0-612-85884-7 Our file Notre référence ISBN: 0-612-85884-7

The author has granted a nonexclusive licence allowing the National Library of Canada to reproduce, loan, distribute or sell copies of this thesis in microform, paper or electronic formats.

The author retains ownership of the copyright in this thesis. Neither the thesis nor substantial extracts from it may be printed or otherwise reproduced without the author's permission.

L'auteur a accordé une licence non exclusive permettant à la Bibliothèque nationale du Canada de reproduire, prêter, distribuer ou vendre des copies de cette thèse sous la forme de microfiche/film, de reproduction sur papier ou sur format électronique.

L'auteur conserve la propriété du droit d'auteur qui protège cette thèse. Ni la thèse ni des extraits substantiels de celle-ci ne doivent être imprimés ou aturement reproduits sans son autorisation.



ABSTRACT

InGaAs/InP PIN photodetectors have been fabricated in the laboratory. Several material characterization techniques are performed to characterize the material. They include current-voltage (I-V) measurements, capacitance-voltage (C-V) measurements, electron beam induce current (EBIC) measurements and deep level transient spectroscopy (DLTS) measurements. It is found that sample V1A and V1B have a higher n⁻ region doping concentration then that of sample V2A. The measurements also indicate that the recombination currents in the devices are small. Depletion width of one of the photodetector in sample V1B is measured and has a value of 0.798 um under zero bias. Using EBIC measurement technique, the maximum electric field within the device is determined and has a value of 12.53 kV/cm under zero bias. It is found that there are minimum measurable majority deep states in the n⁻ intrinsic region of the photodetectors using DLTS measurement technique while deep states are found in the InP buffer layer. They have an energy level of 0.34 eV below the conduction band.

ABSTRAIT

Des détecteurs photoélectrique InGaAs/InP PIN ont été fabriqués dans le laboratoire. Plusieurs techniques de characterization ont été appliqués sur les matériaux. Ces techniques incluent les measures de courant-tension (I-V), de capacité-tension (C-V), de courant induit par faisceaux d'électrons (EBIC) et de la spectroscopie transitoire à niveaux profonds (DLTS). Les résultats montrent que les échantillons V1A et V1B ont une concentration enduisante dans la région n° supérieure à celle de l'échantillon V2A. Ils indiquent également que les courants de recombinaison dans le dispositif sont petits. La largeur d'épuisement du dispositif de l'échantillon V1B a été mesurée et a une valeur de 0.798 um. En utilisant la technique EBIC, la valeur maximale du champ électrique à l'intérieur du dispositif est de 12.53 kV/cm sous la polarization nulle. Des valeurs mesurables des états profonds de majorité ont été trouvées dans l'intrinsèque region n° des détecteurs photoélectrique en utilisant la technique de DLTS. Un état profond a été trouvé dans la couche de l'amortisseur de InP. Le niveau d'energie est 0.34 eV audessous de la bande de conduction.

ACKNOWLEDGMENT

I am grateful to my supervisor, Dr. I. Shih, for his excellent supervision for the past two years. His knowledgeable advice, kindness patience and helpful assistance in teaching are deeply appreciated.

I would like to thank all the graduate students in the Electronic Devices and Materials group for all the assistances and discussions.

I am deeply appreciated to my parents and sister, their unquestionable support in my life.

Thank to Lynn for the past six years.

CONTENTS

ABSTRACT	I		
ABSTRAIT			
ACKNOWLEDGMENT			
CONTENTS			
Chapter 1. INTRODUCTION	1		
1.1. MATERIALS			
1.2. PHOTODETECTORS			
Chapter 2. SEMICONDUCTOR PHOTODIODES	4		
2.1. BASIC PHOTODETECTOR PARAMETERS			
2.2. PIN PHOTODETECTORS			
2.2.1. DC CURRENT RESPONSE & QUANTUM	A EFFICIENCY		
2.2.2. AC CURRENT RESPONSE			
2.2.3. IMPULSE RESPONSE			
2.2.4. NOISE PERFORMANCE			
2.2.5. HETEROJNCTION PHOTODETECTORS			
Chapter 3 DEVICE FARRICATION	20		

Chapter 4	. CURRENT-VOLTAGE MEASUREMENTS 23	3
4.1.	THEORY	
	4.1.1. ZERO BIAS	
	4.1.2. REVERSE BIAS	
	4.1.3. FORWARD BIAS	
	4.1.4. PERIMETER RECOMBINATION CURRENT	
	4.1.5. MINORITY CARRIER LIFETIME EXTRACTION	
4.2.	MEASUREMENTS	
4.3.	SUMMARY	
Chapter 5	. CAPACITOR-VOLTAGE MEASUREMENTS 38	3
5.1.	THEORY	
	5.1.1. JUNCTION CAPACITANCE	
	5.1.2. ONE-SIDED JNCTIONS	
	5.1.3. DIFFUSION CAPACITANCE	
5.2.	MEASUREMENTS	
5.3.	SUMMARY	
Chapter 6	. ELECTRON BEAM INDUCED CURRENT MEASUREMENTS	48
6.1.	THEORY	
	6.1.1. GENERATION VOLUME	
	6.1.2. ELECTRON RANGE	
	6.1.3. ELECTRIC FIELD DISTRIBUTION	

	6.1.5. SURFACE RECOMBINATION VELOCITY	
6.2.	MEASUREMENTS	
	6.2.1. ELECTRIC FIELD DISTRIBUTION	
	6.2.2. DIFFUSION LENGTH	
	6.2.3. SURFACE RECOMBINATION VELOCITY	
6.3.	SUMMARY	
Chapter 7	7. EXCESS CARRIER DISTRIBUTION SIMULATION	63
7.1.	THEORY	
	7.1.1. P ⁺ REGION MODELLING	
	7.1.2. BOUNDARY CONDITIONS	
	7.1.3. PHOTON-INDUCED CARRIER GENERATION	
7.2.	SIMULATIONS	
7.3.	SUMMARY	
Chapter 8	B. DEEP LEVEL TRANSIENT SPECTROSCOPY	72
8.1.	THEORY	
	8.1.1. SHALLOW STATES	
	8.1.2. DEEP STATES	
	8.1.3. DEEP STATE STATISTICS	
	8.1.4. DEEP STATES IN A PIN PHOTODETECTOR	
	8.1.5. TRANSIENT CAPACITANCE	

6.1.4. ELECTRON (MINORITY CARRIER) DIFFUSION LENGTH

8.2.	MEASUREMENTS	
	8.2.1. DLTS SYSTEM	
	8.2.2. MEASUREMENT RESULTS	
8.3.	SUMMARY	
Chapter	9. SUMMARY	90
9.1.	FUTURE WORK	
APPEND RESULTS	IX A: S OF REVERSE I-V MEASUREMENTS UNDER ILLUMINATION	92
APPEND RESULTS	IX B: S OF DIFFUSION LENGTH COMPUTATION USING METHOD 2	93
APPEND RESULTS	IX C: S OF DIFFUSION LENGTH COMPUTATION USING METHOD 3	94
APPEND EXCESS	IX D: CARRIER DISTRIBUTION SIMULATION CODE	95
REFERE	NCES	96

8.1.6. DEEP LEVEL TRANSIENT SPECTROSCOPY

1. INTRODUCTION

In today's high-speed optical fiber communication networks, state of art optoelectronic devices are required to fulfill the increasing data bit rate. Photodetector is one of the key components in a high-speed optical communication network. It is the first element in an optical receiver. A photodetector senses the optical signal incident on it and converts the variation of the optical power into a corresponding electric current. Since the optical signal is usually weakened and distorted when it propagates to the receiver, the photodetector must meet very high performance requirements thus the quality of photodetector has a direct impact on the performance of the whole network [1.1]. In the present work, several material measurement techniques are performed to characterize the InGaAs/InP PIN photodetectors. Physical basis of the photodetector is also studied.

1.1. PHOTODETECTORS

Different types of photodetectors exist: they are photomultipliers [1.2] [1.3] [1.4], pyroelectric detectors [1.5], semiconductor-based photoconductors such as phototransistors and photodiodes [1.6]. However, most of these photodetectors are unsuitable for used in optical fiber communication networks due to various reasons. Photomultiplier consists of a photocathode and an electron multiplier packaged in a vacuum tube. The device can achieve very high gain and low noise, however the large size of the structure and high voltage requirements make it unsuitable for the optical fiber network. Pyroelectric detector absorbs photon energy and converts it into heat. As the material heat up, the dielectric constant changes which can be measured as a capacitance changes, thus the optical signal can be retrieved. However the device performance is limited by the detector's cooling rate after it has been heated up and is not feasible to use

in high-speed networks. Semiconductor-based photodiodes are used exclusively for optical fiber communication networks because of their small size, suitable material, high sensitivity and fast response time. The two most popular types of photodiode used are PIN photodetectors and avalanche photodetectors (APD).

1.2. MATERIALS

There are several materials suitable to fabricate photodetectors over different ranges of communication wavelengths. Silicon is the most practical material for use at 0.8 um wavelength due to the bandgap energy, mature and low cost process. Both germanium and InGaAs can be used in the 1.3 um and 1.55 um regions because of their small bandgap energy values. Parameters for typical PIN and APD photodetectors fabricated using these materials are summarized in Table 1.1 [1.7].

Table 1.1: Parameters for typical PIN and APD photodetectors.

Material	Bandgap	Mobility	Wavelength	Structure	Wavelength	Peak	Gain
	Energy	(electron	of Peak		Range (um)	Responsivity	
	(eV)	/hole)	Response			(A/W)	
		(cm^2/Vs)	(um)				
Si	1.12	1350/	0.8	PIN	0.3 - 1.1	0.6	1
	(indirect)	480		APD	0.4 - 1.0	75	20-400
Ge	0.66	3900/	1.55	PIN	0.8 - 1.7	0.5	1
	(indirect)	1900	:	APD	1.0 - 1.6	35	50-200
$In_{0.53}Ga_{0.47}$	0.75	7000/	1.7	PIN	0.9 - 1.7	0.95	1
As	(direct)	300		APD	1.0 - 1.7	12	10-40

For the communication wavelength at 1.55 um, InGaAs is used exclusively to fabricate optoelectronic devices instead of Ge due to its direct bandgap energy, high responsivity and high electron mobility value [1.8]. Another advantage of InGaAs over Ge is the ability to fabricate heterojunction photodetectors to enhance the device performance. Details on the heterojunction photodetectors are discussed in Chapter 2. The main disadvantages for InGaAs material are the cost and the process difficulty. The cost of an InP epi-wafer where InGaAs material is to be grown on is high compared to germanium

and silicon materials. The processes used to grown the InGaAs layer, such as metal-organic chemical vapor deposition (MOCVD) [1.9] and molecular beam epitaxy (MBE) [1.10], require high level of control and expertise. In addition, InP is a very fragile material and is easy to be damaged during device fabrication processes, thus production cost is usually high for InP based devices.

2. SEMICONDUCTOR PHOTODIODES

A photodetector is an optoelectronic device that converts photon energy into electrical energy using photodetection process. A photodetection process usually consists of three steps [2.1]: 1) absorption of optical energy and generation of electron-hole pairs, 2) transportation of the photogernerated electron-hole pairs across the absorption and/or transit region, with or without gain, and 3) carrier collection and generation of a photocurrent, which flows through external circuitry. Semiconductor photodiodes are widely used in optical fiber communication networks. The performance requirements from the detector are high sensitivity, high gain, low noise, wide bandwidth, high reliability and low cost. Usually gain and bandwidth are fundamental physical trade-offs. Depending on the application requirements, different photodetector structures are used for different applications. There are two main types of photodiodes used in optical fiber communication networks; they are PIN diodes and avalanche photodiodes (APD) [2.2]. Photodetectors are also classified into intrinsic and extrinsic types. An intrinsic

Photodetectors are also classified into intrinsic and extrinsic types. An intrinsic photodetector detects light with wavelengths close to the bandgap energy of the semiconductor. An extrinsic photodetector detects light of energy smaller than the bandgap energy of the material. These devices usually involve introducing impurity and defect levels within the band gap. PIN photodetector and APD photodetector are intrinsic type photodetectors [2.3]. In this chapter, the principle of PIN photodetector is discussed in details.

2.1. BASIC PHOTODECTOR PARAMETERS

When light is incident on a photodetector, not all the photons can be absorbed by the solid and generate electron-hole pairs. The parameter external quantum efficiency η_{ext} is

an indicator of how many electron-hole pairs generated for a given amount of input optical power. It is defined by the number of electron-hole pairs collected at the photodetector terminals divided by the number of incident photons. It is also an indication of how good the device is in terms of sensitivity. The general equation for the external quantum efficiency is expressed as:

$$\eta_{ext} = \frac{I_{ph}/q}{P_{inc}/hv} \quad (2.1)$$

where I_{ph} is the photocurrent, P_{inc} is the input optical power. The external quantum efficiency of a photodetector also depends on the absorption coefficient α of the material and the thickness of the absorbing region. A general relationship between these parameters is shown below:

$$n_{ext} \infty (1 - e^{-\alpha x}) \tag{2.2}$$

where α is the absorption coefficient and x is the thickness of the active region. Table 2.1 shows the absorption coefficient of several commonly used photodetector materials [2.4].

Table 2.1: Absorption coefficient of several commonly used photodetector materials.

Material/		$\lambda = 0.8 \text{ um}$	$\lambda = 1.33 \text{ um}$	$\lambda = 1.5 \text{ um}$	
	Absorption coefficient (cm ⁻¹)	70.0 din	70 1.55 4111	70 115 4111	
	Si	$1x10^{3}$	NA	NA	
	Ge	5x10 ⁴	$1x10^{4}$	$5x10^{2}$	
	InGaAs	NA	2x10 ⁴	$1x10^{4}$	

There is another related material characterization parameter called internal quantum efficiency η_i . The internal quantum efficiency is defined as the number of electron-hole pairs created divided by the number of photons absorbed. The value is usually close to 1 in pure, defect-free materials. The responsivity \Re of a detector is defined as the photocurrent induced divided by the incident photon power and is expressed as:

$$\Re = \frac{I_{ph}}{P_{inc}} = \frac{\eta_{ext}q}{hv} = \frac{\eta_{ext}\lambda(um)}{1.24}(A/w) \qquad (2.3)$$

A high responsivity detector is a high sensivity detector. The above equation indicates that η_{ext} and \Re are linearly related. However, η_{ext} is dependent on the absorption coefficient α (Eq. 2.2) which is dependent on the wavelength λ (Table 2.1). As a result, the responsivity spectral response of a detector is bandgap dependent [2.5]. An illustration of the responsivity spectral response of ideal and real photodetectors are shown below:

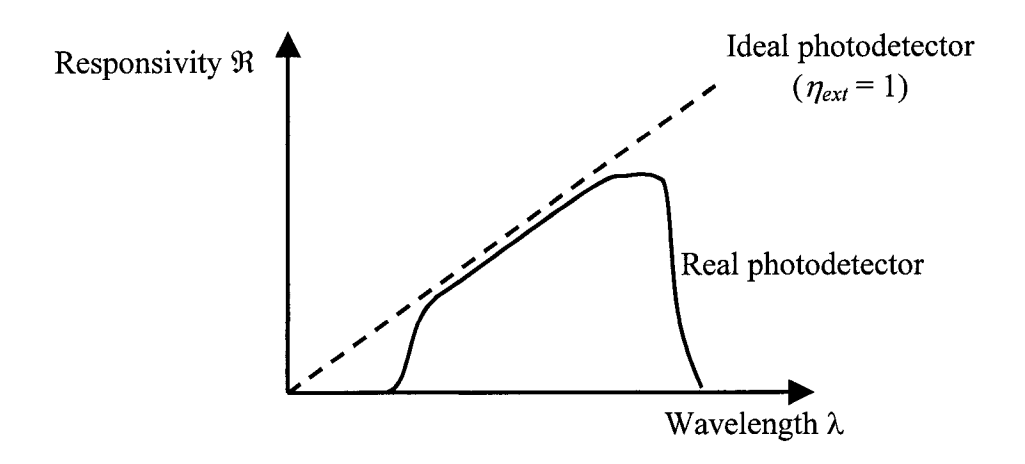


Figure 2.1: Responsivity spectral response of ideal and real photodetectors.

2.2. PIN PHOTODETECTORS

PIN photodiode is a junction diode in which an undoped or lightly doped intrinsic region is inserted between p⁺ and n⁺ regions. A PIN photodiode operates under reverse bias condition in an optical receiver. A schematic of PIN photodetector is shown in Figure 2.2. Because of the very low free carrier density in the intrinsic region, applied bias voltage drop almost entirely across the intrinsic region which is fully depleted under reverse bias.

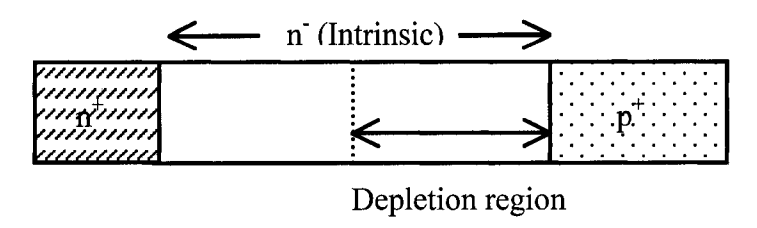


Figure 2.2: Schematic of a PIN photodetector.

When an incident photon has energy greater than or equal to the bandgap energy of the semiconductor material, the photon can give up its energy and excites an electron from the valance band to the conduction band. This process generates free electron-hole pairs, which are known as photogenerated carriers. If the free electron-hole pairs are generated within the depletion region, then they will be swept away by the large electric field in the region almost instantly. The transit time that the electron-hole pairs required to travel through the depletion region depends on the width and the carrier velocity which is usually the saturation velocity due to the high electric field. Current due to this carrier drifting motion is the drift current J_{dr} . If the free electron-hole pairs are generated outside the depletion region, then they might diffuse to the edge of the depletion region and be swept by the electric field. However this diffusion motion usually slows down the response speed of the photodetector. Current due to this motion is the diffusion current This diffusion effect can be minimized by fabricating the junction close to the illuminated surface. Figure 2.3 shows the carrier drifting and diffusion motion in an energy band diagram for a PIN photodetector. For a high-speed PIN photodetector, the depletion layer width should be small to minimize the carrier travel time in the region. For devices of high quantum efficiency or high responsivity, the depletion width should be large in order to absorb as many photons as possible. There is no internal optical gain in a PIN photodetector due to space charge limitation.

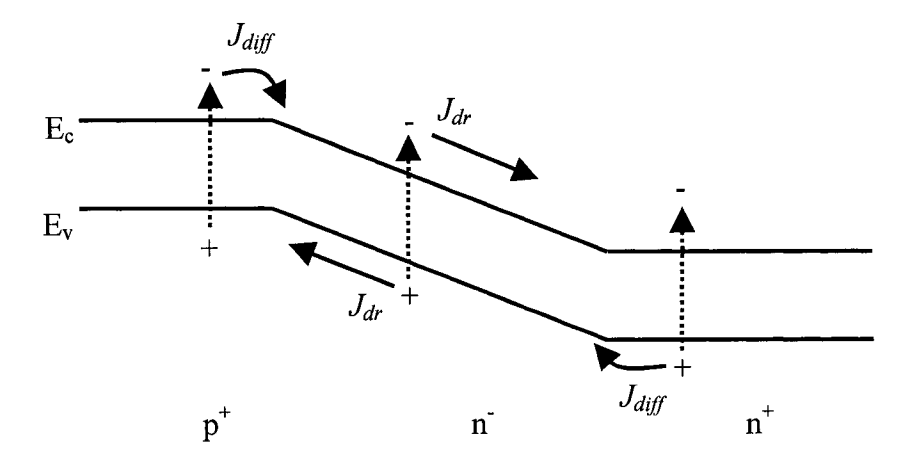


Figure 2.3: Carrier drifting and diffusion motion in an energy band diagram for a PIN photodetector.

2.2.1. DC CURRENT RESPONSE & QUANTUM EFFICIENCY

Since the photogenerated carriers in different regions of a PIN photodetector experience motions due to different forces, either drifting or diffusion, the total photocurrent density through the reverse-biased photodetector is expressed as:

$$J_{ph}=J_{dr}+J_{diff}$$
 (2.4)

The photogenerated carrier density can be computed by assuming the p^+ region width is much smaller than the inverse of absorption coefficient α^{-1} and the thermal generation within the device is negligible [2.6]. Assuming the internal quantum efficiency η_i to be equal to 1, the electron-hole pair generation rate is expressed as:

$$G(x) = \Phi_o \alpha e^{-\alpha x} = \frac{P_{inc}(1 - \Theta_R)}{Ahv} \alpha e^{-\alpha x} \quad (2.5)$$

where α is the absorption coefficient (cm⁻²), Φ_0 is the incident photon flux (photons/sec/cm²), Θ_R is the reflectivity of the top surface, P_{inc} is the input optical power and A is the active area of the detector. In practice, the value of Θ_R is made as small as

possible by depositing an antireflection coating on the photodetector. The drifting component of the photocurrent can be computed by integrating the generated carriers within the depletion region and is expressed as:

$$J_{dr} = -q \int_{0}^{w} G(x) dx = -q \Phi_{o} (1 - e^{-\alpha w})$$
 (2.6)

where w is the width of the depletion region and G(x) is the carrier generation rate in Equation 2.5. The diffusion component of the total photocurrent can be found by computing the minority hole carrier concentration gradient at the end of the depletion region adjacent to the p^+ region and is expressed as:

$$J_{diff} = -qD_h \left(\frac{\partial P_n}{\partial x}\right)_{x=W} = -q\Phi_o \frac{\alpha L_h}{1 + \alpha L_h} e^{-\alpha w} - qP_{no} \frac{D_h}{L_h}$$
 (2.7)

where L_h is the hole diffusion length, P_{no} is the hole thermal equilibrium concentration and D_h is the hole diffusion coefficient. The gradient of the minority hole carrier concentration is computed by solving the ambipolar equation (Eq. 4.2) and is discussed in details in Chapter 4. The photocurrent density is obtained by adding Equations 2.6 and 2.7 together and is expressed as:

$$J_{ph} = J_{dr} + J_{diff} = -q\Phi_o \left(1 - \frac{e^{-\alpha w}}{1 + \alpha L_h}\right) - qP_{no} \frac{D_h}{L_h} \quad (2.8)$$

Since the thermal equilibrium minority hole carrier concentration is very low, thus the second term in the photocurrent density is negligible. As a result, the photocurrent density is mainly dependent on the incident photon flux Φ_o as expected. The quantum efficiency of the PIN diode can be expressed as:

$$\eta_{ext} = \frac{\left| J/q \right|}{P_{inc}/Ahv} = (1 - \Theta_R) \left(1 - \frac{e^{-\alpha w}}{1 + \alpha L_n} \right) \quad (2.9)$$

According to the equation, high device quantum efficiency requires a low reflection coefficient, large α , w and L_n . If the internal quantum efficiency is less than 1 and diffusion length is small, then the external quantum efficiency can be rewritten as:

$$\eta_{ext} = \eta_{in} (1 - \Theta_R) (1 - e^{-\alpha w}) \qquad (2.10)$$

2.2.2. AC CURRENT RESPONSE

The AC response, or bandwidth, of a PIN photodetector is determined by transit time effects [2.7]. This is because the photogenerated electron-hole pairs require a finite time to traverse the depletion region. If the incident light is modulated at high frequency, then a phase difference between the photon flux and the photocurrent will be created. The AC response of a PIN photodetector can be modeled by assuming: 1) carriers travel at saturation velocity in the depletion region, 2) the transit time of carriers is much shorter than the bulk recombination lifetime, 3) electric field is large so that the diffusion current can be neglected and 4) the incident photon flux is assumed to be of the form:

$$\Phi_{inc} = \Phi_o(1 + e^{j\omega t}) \qquad (2.11)$$

The corresponding electron-hole pair generation rate and carrier densities are given by:

$$G(x,t) = G_o(x) + G_{oc}(x)e^{j\omega t}$$
 (2.12)

$$p(x,t) = p_{dc}(x) + p_{ac}(x)e^{j\omega t}$$
 (2.13)

$$n(x,t) = n_{dc}(x) + n_{ac}(x)e^{j\omega t}$$
 (2.14)

The ambipolar equation for the AC components can be expressed as:

$$\frac{\partial J_{eac}}{\partial x} - j\omega \frac{J_{eac}}{\upsilon_e} = -qG_{ac}$$
 (2.15)

$$\frac{\partial J_{hac}}{\partial x} - j\omega \frac{J_{hac}}{\upsilon_h} = -qG_{ac}$$
 (2.16)

where v_e and v_h are the hole and electron saturation velocities and $G_{ac} = \alpha \Phi_o e^{-\alpha x}$. With boundary conditions $J_{eac}(0) = 0$ and $J_{hac}(w) = 0$, the solutions for the equations are:

$$J_{eac}(x) = -\alpha q \Phi_o \left[\frac{e^{\frac{j\omega x}{v_h}} - e^{-\alpha x}}{\alpha + j\omega/v_e} \right]$$

$$J_{hac}(x) = -\alpha q \Phi_o \left[\frac{e^{-\alpha w} - e^{-\alpha w + \frac{j\omega(w - x)}{v_h}}}{\alpha - j\omega/v_h} \right]$$
(2.17)

The AC signal of the photodetector can be obtained by using Equation 2.19:

$$J(\omega) = \frac{1}{w} \int_{0}^{w} (J_{eac}(x) + J_{hac}(x)) dx$$
 (2.19)

Substituting Equations 2.17 and 2.18 into Equation 2.19 and solve for the integral give the AC current response, which is expressed as:

$$J(\omega) = q\Phi_o \alpha w \left[\frac{e^{-\alpha w} - 1}{\alpha w (\alpha w - j\omega t_{tr}^h)} + \frac{e^{-\alpha w} (e^{j\omega t_{ht}^h} - 1)}{j\omega t_{tr}^h (\alpha w - j\omega t_{tr}^h)} \right]$$

$$+ q\Phi_o \alpha w \left[\frac{1 - e^{j\omega t_{tr}^e}}{j\omega t_{tr}^e (\alpha w + j\omega t_{tr}^e)} + \frac{1 - e^{j\omega t_{tr}^e}}{\alpha w (\alpha w + j\omega t_{tr}^e)} \right]$$

$$(2.20)$$

where t^e_{tr} and t^h_{tr} are the electron and hole transit times. The above AC current equation models the intrinsic frequency response of the PIN diode due to the high frequency modulated photon flux only. In order to model a practical PIN photodetector, other extrinsic circuit parameters, such as junction capacitance, diode shunt resistance, contact resistance...etc, have to be included in the circuit model. A practical equivalent circuit of a PIN photodiode is shown in Figure 2.4.

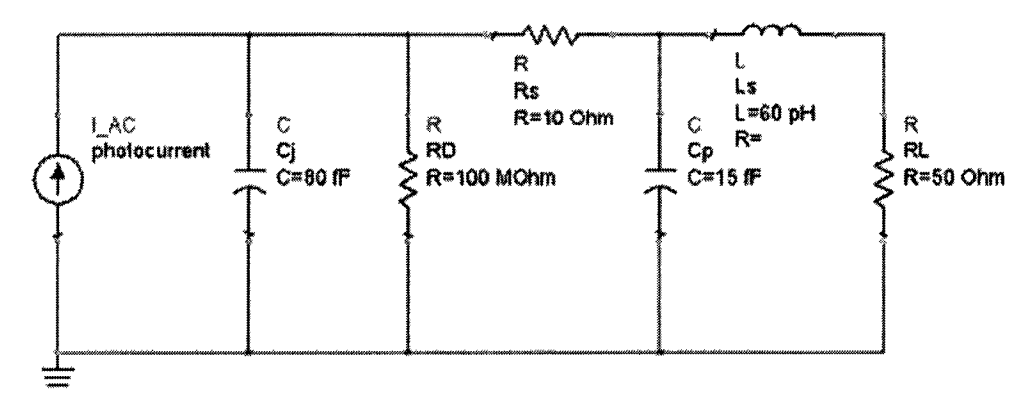


Figure 2.4: Equivalent circuit of a PIN photodiode.

where photocurrent I_AC is the intrinsic AC response photocurrent, C_j is the junction capacitance, C_p is the parasitic capacitance, L_s is the total series inductance, R_D is the diode shunt resistance, R_s is the series resistance and R_L is the load resistance. Typical extrinsic component values are shown in the. The frequency response of the circuit model becomes:

$$J_0(\omega) = J(\omega)H(\omega)$$
 (2.21)

where $J_o(\omega)$ is the output current across the load. $H(\omega)$ is the transfer function of the equivalent circuit which is represented by the following equation:

$$H(\omega) = \frac{R_D}{a + j\omega(b - c\omega^2) - d\omega^2}$$
 (2.22)

$$a = R_S + R_L + R_D$$

$$b = R_s R_L C_p + L_S + (R_S + R_L) R_D C_j + R_L R_D C_P$$

$$c = R_S L_S C_P R_D C_j$$

$$d = (R_S R_L C_P + L_S) R_D C_j + R_S L_S C_P + R_D C_P L_S$$

According to Equation 2.20, the depletion width plays an important role in the AC response of the PIN photodetector. Increasing the depletion width can increase the AC response magnitude. A calculated AC response of a hypothetical PIN photodetector for different depletion widths and different frequencies plot is shown in Figure 2.5.

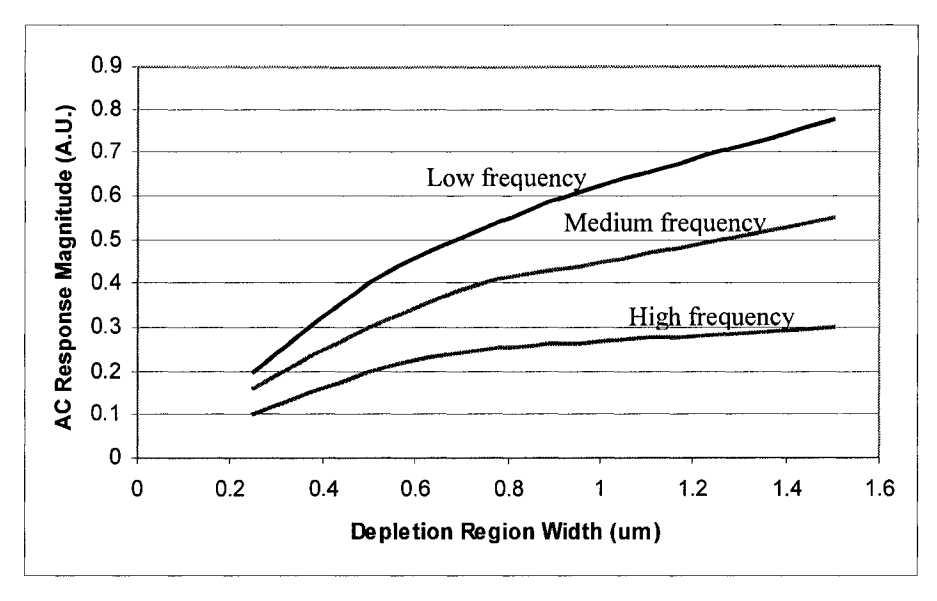


Figure 2.5: AC response of a hypothetical PIN photodetector for different depletion widths and different frequencies.

The calculated AC response plot indicates that a PIN photodetector with a small depletion width has a small AC response signal but it is less subject to frequency. On the other hand, a PIN photodetector with a large depletion width has a large AC response signal but the signal magnitude is more frequency dependent.

2.2.3. IMPULSE RESPONSE

PIN photodetector is usually used in a digital optical network where data are transmitted in pulses form. Thus the impulse response is an important parameter for high-speed PIN photodetectors. The theoretical impulse response can be obtained simply by solving the discrete Fourier transform of the photocurrent in the frequency domain (Eq. 2.21). This transformation of photocurrent from frequency domain to time domain gives an ideal, symmetrical photocurrent plot shown in Figure 2.6.

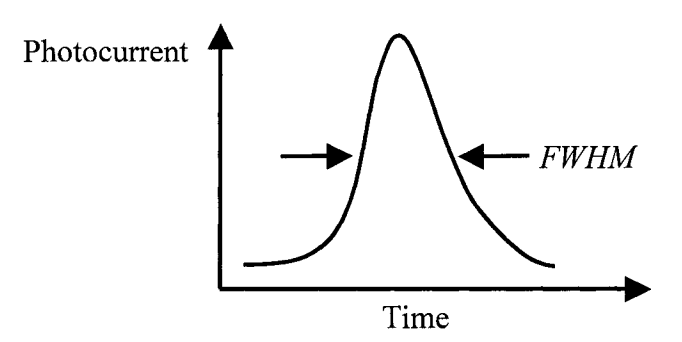


Figure 2.6: Computed temporal response of a PIN photodetector.

From the computed temporal response and the corresponding frequency response, the 3 dB frequency can be related to the rise time of the device and is expressed as:

$$f_{3dB} = \frac{1.4}{\pi t_r} \qquad (2.23)$$

where t_r is the rise time of the device and is defined as the time that requires for the total output current of the photodetector to rise from 10% to 90% of its peak value when an optical power is applied. The 3 dB frequency is the frequency at which the response of the photodetector drops to half of its peak value. It can also be expressed in terms of full-width-at-half-maximum (FWHM) using the following equation:

$$f_{3dB} = \frac{1}{2(FWHM)}$$
 (2.24)

FWHM is defined as the width of the photocurrent in a temporal response where the current magnitude is greater than the half peak value of the response. FWHM is indicated in Figure 2.6.

In a practical PIN photodetector, electron-hole pairs will be generated outside the depletion region and the ideal temporal response shown in Figure 2.6 is not accurate. Because the electron-hole pairs generated outside the depletion region can diffuse to the

edge of the depletion region and contribute to photocurrent, additional photocurrent components have to be considered [2.8]. A modified temporal plot considering the diffusion current is shown in Figure 2.7. Due to the fact that carrier diffusion motion is much slower than carrier drifting motion, by approximately 1000 times, a tail of photocurrent is shown in the temporal plot.

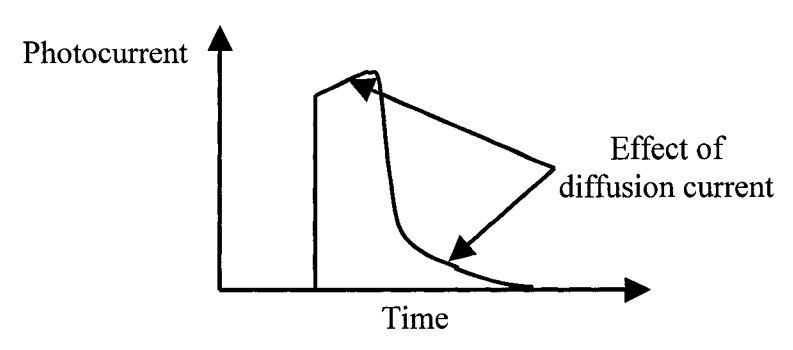


Figure 2.7: Computed temporal response with the consideration of diffusion current of a PIN photodetector.

One can deduce that the long tail in the temporal response due to the diffusion current is the main performance limitation in high-speed photodetector. A well-designed high-speed photodetector should have a controlled depletion width which is wide enough to absorb all the photons but short enough to minimize the carrier transit time. A rule of thumb to design the depletion width is:

$$w \ge [\alpha(\lambda)]^{-1} \qquad (2.25)$$

Where w is the depletion region width and $\alpha(\lambda)$ is the absorption coefficient of the wavelength of operation.

2.2.4. NOISE PERFORMANCE

Shot noise:

Shot noise is the noise due to the fluctuations in the generation and recombination processes inside the semiconductor material. Shot noise causes a fluctuation in carrier

concentration and hence fluctuation in current (noise) if a current is passing thought the device. Shot noise is also known as generation noise because of its origin [2.9]. For a PIN photodetector, there are several current components which may lead to shot noise. They are photocurrent I_{ph} , dark current I_D and background current I_B . The photocurrent is due to illumination of light, dark current is due to the leakage current of the device and background current is due to the radiation in the environment. The equivalent shot noise current due to these three current components in a PIN photodetector can be expressed as:

$$\overline{i_S^2} = 2q(I_{ph} + I_B + I_D)B$$
 (Assuming $f = 1/2\pi\tau$) (2.26)

where *B* is the bandwidth of the device.

Thermal noise:

Apart from the shot noise, there is another noise component in a PIN photodetector called thermal noise or Johnson noise. The origin of the thermal noise is the random motion of carriers that contribute to the current. According to the device model in Figure 2.4, there are three resistance components in a PIN photodetector; they are series resistance R_s , shunt resistance R_D and the load resistance R_L . Since the series resistance is usually small, it is often neglected in the thermal noise. If the photodetector is connected to an external circuit, then the input resistance R_i of the external circuit has to be considered. The mean-square noise current due to thermal noise is expressed as:

$$\overline{i_J}^2 = \frac{4kTB}{R_{eq}}$$
 (2.27)
$$R_{eq} = \left(\frac{1}{R_D} + \frac{1}{R_L} + \frac{1}{R_i}\right)^{-1}$$
 (2.28)

where T is temperature in Kevin (K) and k is the Boltzmann constant.

The total noise current of a PIN photodetector can be computed by combining Equations 2.26 and 2.27. It is expressed below:

$$\overline{i_N^2} = \overline{i_S^2} + \overline{i_J^2}$$
 (2.29)

The Signal-to-noise (power) ratio of the photodetector is defined as:

$$\frac{S}{N} \approx \frac{signal - power}{noise - power} = \frac{\overline{i_{ph}^2}}{\overline{i_N^2}} = \frac{\frac{1}{2} \left(\frac{q \eta p_{inc}}{hv}\right)^2}{2q(I_{ph} + I_B + I_D)B + \frac{4k_B TB}{R_{eq}}}$$
(2.30)

A complete circuit model of a PIN photodetector with consideration of parasitic components and noise components is shown in Figure 2.8.

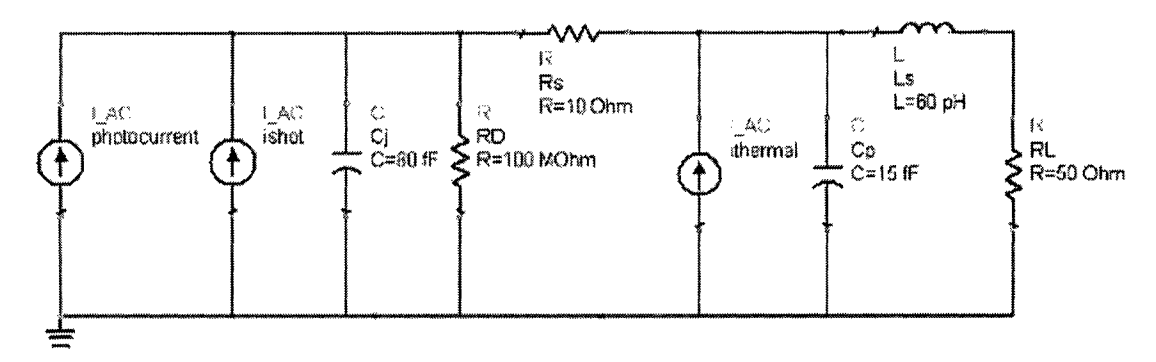


Figure 2.8: A complete circuit model of a PIN photodetector with consideration of parasitic components and noise component

Noise Equivalent Power:

The sensitivity of a photodetector is an important parameter and is defined as the minimum optical input power needed to achieve a signal-to-noise ratio greater than certain value. Noise equivalent power (NEP) is a standard way to measure the sensitivity of a device. It is defined as the rms optical signal power at bandwidth B=1 Hz required to produce the photocurrent magnitude equals to the noise current magnitude and the signal-to-noise ratio equal to unity. The NEP of a PIN photodetector is expressed as:

$$NEP = \frac{hv}{q\eta_{ext}} \left[2q(I_{ph} + I_B + I_D) + \frac{4k_BT}{R_{eq}} \right]^{1/2} (W.Hz^{-1/2}) \quad (2.30)$$

For a high sensitivity PIN photodetector, the I_B and I_D should be small while the R_{eq} should be large. The NEP is also known as a measure of the minimum detectable power $(P_{inc})_{min}$. Another parameter which can be derived from the NEP is the detectivity D. It is defined as:

$$D = \frac{1}{NEP} (W^{-1} \cdot Hz^{1/2})$$
 (2.31)

The detectivity indicates how sensitive a detector is. The larger the detectivity, the higher the sensitivity. It is more convenient to include the device size and bandwidth when comparing sensitivity of photodetectors. Thus specific detectivity D^* [2.10] is defined as:

$$D^* = \frac{A^{1/2}B^{1/2}}{NEP}(cm \cdot Hz^{1/2}W^{-1})$$
 (2.32)

where A is the area of the photodetector and B is the bandwidth.

2.2.5. HETEROJNCTION PHOTODETECTORS

For a optical fiber communication network, a semiconductor photodiode always operates under reverse bias. Homojunctions make of materials such as InGaAs ($E_g = 0.74 \, \text{eV}$) or InGaAsP ($E_g = 0.74 \, \text{eV}$) have a small energy bandgap, a low breakdown voltage and a high reverse leakage current. These factors are undesired for a high-speed photodetector. In addition, according to Section 2.2.3 a high-speed photodetector should have a minimum diffusion current component and a controlled depletion region width. All these factors can be compensated by a heterojunction photodetector.

A heterojunction is formed by joining together two different materials with different doping concentrations and energy band gaps [2.11]. By putting a heterojunction in a PIN photodetector using small energy bandgap material as the intrinsic layer, a photodetector with better performance can be obtained. It is because photons will not be absorbed in the large energy bandgap regions and will be absorbed only in the intrinsic layer where the energy bandgap matches with the photon energy. Since there is almost no electronhole pair generates outside the intrinsic region, thus the diffusion current component in the photodetector is minimum. A typical heterojunction PIN photodetector structure is shown in Figure 2.9.

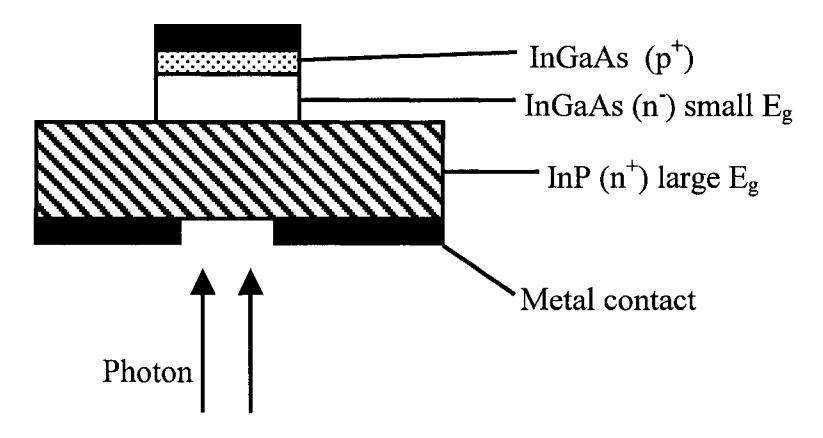


Figure 2.9: Typical heterojunction PIN photodetector.

From Figure 2.9, one can see that light is incident on the photodetector from the InP substrate. It is because the InP material has a large energy bandgap and acts as a transparent window to the photons. Photons travel across the substrate and are absorbed in the InGaAs intrinsic region only. In addition, the substrate metal contacts act as a window to limit the active area of the photodetector in order to minimize the junction capacitance and hence achieve higher performance.

3. DEVICE FABRICATION

Mesa type PIN InGaAs/InP photodetectors were fabricated in the lab by Dr. I. Shih. The InP epi-wafer used has the following characteristics: 350 um InP Silicon doped (n⁺) substrate, 0.5 um InP buffer layer and 2.5 um InGaAs intrinsic layer. In order to create a PIN doping profile, Zn diffusion process [3.1] was performed to produce the p⁺ region in the intrinsic layer. The diffusion process was performed in ultra clean environment to prevent contaminations. A three-zone furnace Model MB71 from Thermco Products Corperate was used to perform the diffusion process. Diffusion temperature and time were carefully determined by both theoretical computation and previous experiments. A schematic showing the diffusion process is displayed in Figure 3.1.

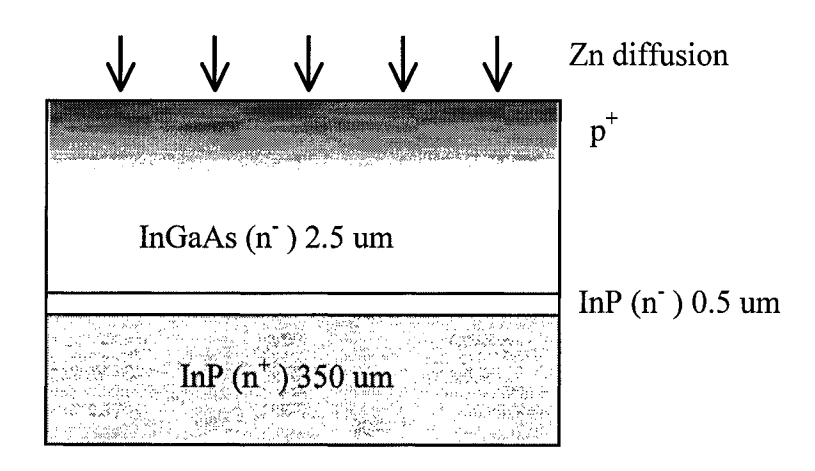


Figure 3.1: Schematic of Zn diffusion process.

Photodetector active area was defined using lithography process [3.2]. Lift-off process was used to form the device structures. The fabricated photodetector had an active area of 300 um x 300 um. Gold and chrome were deposited on top of the p^+ region of the device using physical vapor deposition technique [3.3] to form the anode metal contact. The metal contact had a size of 100 um x 100 um. Figure 3.2 shows two pictures of the

fabricated photodetectors. Four samples were fabricated in the lab; each sample contained thirty-six devices (six columns and six rows). They were named as V-1, V-2, V-3 and V-4. Sample V-3 was a failure while others contained 5 to 20 good devices each.

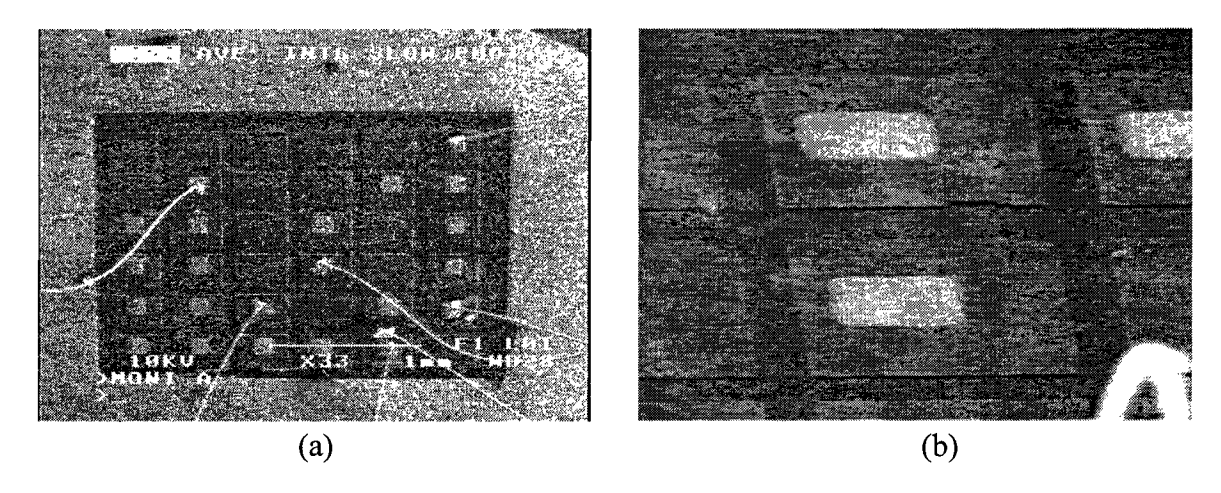


Figure 3.2: Fabricated InGaAs/InP PIN photodetectors. (a) A picture of sample V-2-A with wire bonded to selected devices. (b) A picture of two of the photodetectors. The white areas are the metal contacts.

InP is a very fragile material and is prompted to damaged when mishandled. In order to perform device measurement effectively without damaging the sample, each sample was mounted on a metal patterned glass substrate. The metal patterns on the glass substrate served as cathode and anode terminals to the photodetectors. The measuring equipment probed on the metal patterns instead of making direct contact with the fragile material during measurement. Figure 3.3 shows the schematic of a patterned glass substrate.

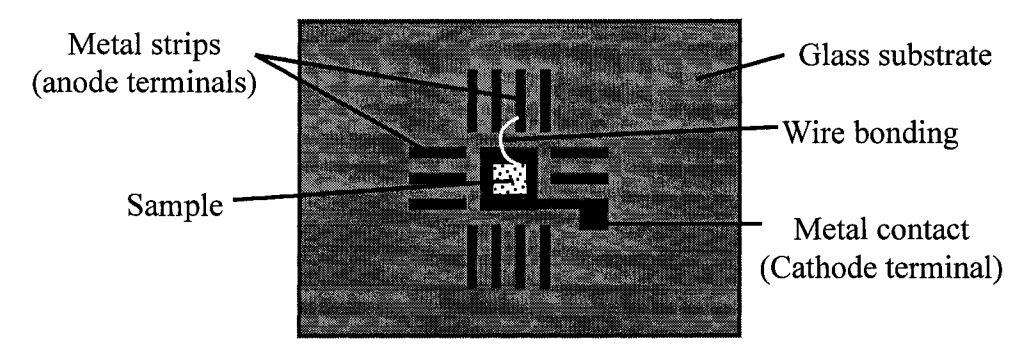


Figure 3.3: Metal patterned glass substrate.

Sample was mounted in the middle of the metal pad on the glass substrate using silver epoxy. Silver epoxy provided a low resistance ohmic contact to connect the metal pad to the sample n⁺ substrate to form the cathode terminal of the photodetectors. The glass substrate also provided metal strips for wire bonding to the anode terminals of the devices.

4. CURRENT-VOLTAGE MEASUREMENTS

The method of current-voltage (I-V) measurement is a simple technique to characterize the function of a PIN photodetector. Carrier distribution and carrier transport in the device vary as the applied voltage changes based on the device structures and material properties. By studying the I-V plot of a PIN photodetector, important device characteristics can be extracted.

4.1. THEORY

The theory of PN junction is well developed and is derived base on the solid-state physics theory [4.1]. The PN junction theory can be universally applied to PIN photodetectors with different doping concentrations. According to the theory, the motion of majority carriers in a semiconductor is govern by the motion of minority carriers. By studying the distribution of minority carriers in a junction, one can learn the transport of majority carriers and hence understand the current response of the junction. The carrier concentration and distribution in an equilibrium semiconductor is described by quantum mechanics [4.2], which explains that energy states are quanta and the density of states are estimated by Fermi-Dirac probability function (Eq. 4.1).

$$f_F(E) = \frac{1}{1 + \exp(\frac{E - E_F}{kT})}$$
 (4.1)

E: State energy

 E_F : Fermi energy

k: Boltzmann's constant

T: Temperature

For a non-equilibrium semiconductor, ambipolar transport equation (Eq. 4.2) [4.3] is used to describe the behavior of excess carriers in time and space. The Ambipolar equation is derived from the continuity equation (Eq. 4.3) and the drift and diffusion equation (Eq.

4.4). The continuity equation describes the flow of carriers and the generation/recombination rate of excess carriers while the drift and diffusion equation describes the flow of carriers due to concentration gradient and electric field.

$$D_{p} \frac{\partial^{2}(\delta p)}{\partial x^{2}} - \mu_{p} E \frac{\partial(\delta p)}{\partial x} + g_{p'} - \frac{\delta p}{\tau_{po}} = \frac{\partial(\delta p)}{\partial t} \quad \text{(for excess holes) (4.2)}$$

 D_p : Hole diffusion coefficient

 δp : Excess minority carrier hole concentration

 μ_p : Hole mobility

 g_p ': Excess hole generation rate

 τ_{po} : Hole lifetime under low injection

$$\frac{\partial p}{\partial t} = -\frac{\partial F_p^-}{\partial x} + g_p - \frac{p}{\tau_{po}} \qquad \text{(for holes)} \qquad (4.3)$$

 F_p : Hole-particle flux

 g_p : Hole generation rate

p: Hole concentration

$$J_p = e\mu_p p\varepsilon - eD_p \frac{\partial p}{\partial x}$$
 (for holes) (4.4)

 ε : Electric field

In the following three sections, the carrier distribution and carrier transport of a PIN photodetector is discussed using the concept of the Fermi-Dirac probability function, and the ambipolar equation under different biasing conditions: zero bias, reverse bias and forward bias.

4.1.1. ZERO BIAS

A PIN photodetector is formed by joining p⁺, n⁻ and n⁺ regions together. When zero voltage is applied to the device, the device is in thermal equilibrium and the Fermi energy level is constant throughout the entire system. Figure 4.1 shows the energy-band diagram of a PIN photodetector in thermal equilibrium.

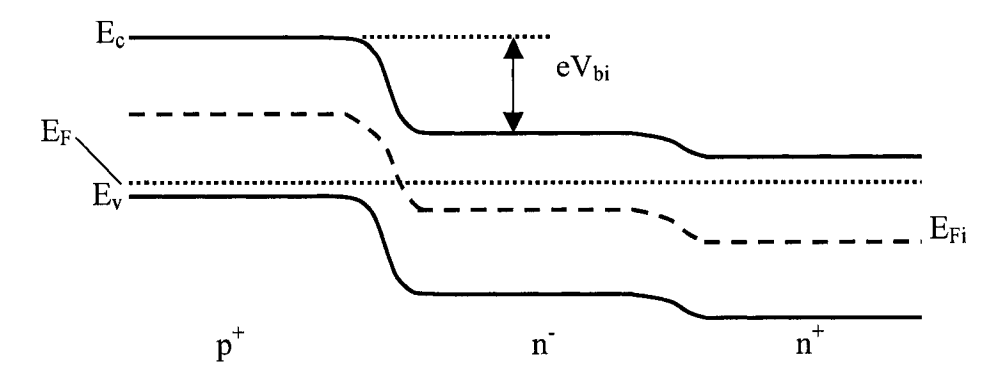


Figure 4.1: Energy-band diagram for a PIN photodetector in thermal equilibrium. E_F is the Fermi energy, E_{Fi} is the intrinsic Fermi energy, E_c is the conduction bend energy and E_v is the valence bend energy.

The conduction and valance band must be bent in the depletion regions between junctions in such system. Electrons in the n^- region see a potential barrier when trying to move in the conduction band of the p^+ region. This potential barrier is known as the built-in voltage (V_{bi}) . Similarly, electrons in the n^+ region also see a potential barrier when trying to enter the conduction band of the n^- region, however this potential barrier is very small and is insignificant in room temperature. The built-in voltage of the device can be computed using the following equation:

$$V_{bi} = \frac{kT}{e} \ln(\frac{N_a N_d}{n_i^2}) = V_t \ln(\frac{N_a N_d}{n_i^2})$$
 (4.5)

where N_a is the acceptor concentration in the p^+ region, N_d is the donor concentration in the n^- region, n_i is the intrinsic carrier concentration and V_t is the thermal voltage. The establishment of build-in voltage, hence build-in electric field, prevents most of the majority carrier from moving out of the region. A few majority carriers with high-energy can over come the potential barrier and diffuse to the opposition region result in a majority carrier diffusion current. At the same time, a few minority carriers in the edge of the depletion opposite region are swept by the electric field result in a minority carrier

drift current. Under thermal equilibrium condition, the magnitude of the majority carrier diffusion current is same as the minority carrier drift current, therefore the total external current is zero and the majority and minority carrier distribution in each region is constant. A carrier distribution diagram of a PIN photodetector is shown in Figure 4.2.

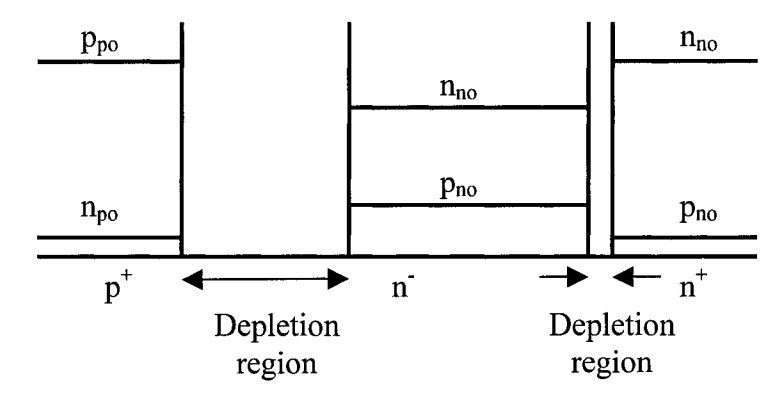


Figure 4.2: Carrier distribution diagram of a PIN photodetector under zero bias.

4.1.2. REVERSE BIAS

When a potential is applied to the p⁺ and n⁺ regions, the photodetector is no longer be in an equilibrium condition and the Fermi energy level is not constant through the device. Figure 4.3 shows an energy-bend diagram of a PIN photodetector under reverse bias condition.

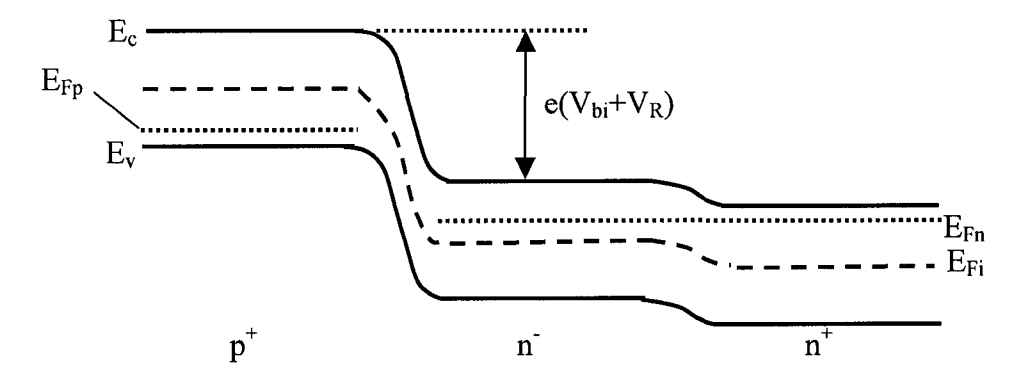


Figure 4.3: Energy-band diagram for a PIN photodetector under reverse bias condition. E_{Fn} is the Fermi energy in the n region, E_{Fp} is the Fermi energy in the p region, V_R is the applied reverse bias voltage.

When a reverse bias is applied to a PIN photodetector, potential across the p⁺/n⁻ junction increases and the electric field strength also increases. As a result, fewer majority carriers can overcome the potential barrier and the majority carrier diffusion current is reduced to less than its thermal equilibrium value. However, the minority carriers can still be swept by the electric field and maintaining its thermal equilibrium value. The minority carrier drift current is dependent only on the generation rate. The reductions of majority carrier drift current leads to a decrease of minority carrier concentration in the edge of the depletion region and resulted in an external current. This external current is the result of minority carrier drift current and is known as the "saturation current". The saturation current is described by the following equation:

$$J_{s} = \left[\frac{eD_{p}p_{no}}{L_{p}} + \frac{eD_{n}n_{po}}{L_{n}} \right] \quad (4.6)$$

where L_p and L_n are the hole and electron diffusion length. The saturation current equation (Eq. 4.6) is independent of reverse voltage which suggests that the current remain constant with different reverse bias in this ideal case. In steady state, the minority carrier concentration at the edge of the depletion region is very close to zero.

Under low injection condition, the density of minority carriers injected to the opposite side is very small compared to the majority carrier density. As a result, the concentration of majority carrier does not change. A carrier distribution diagram of a PIN photodetector under reverse bias condition is shown in Figure 4.4.

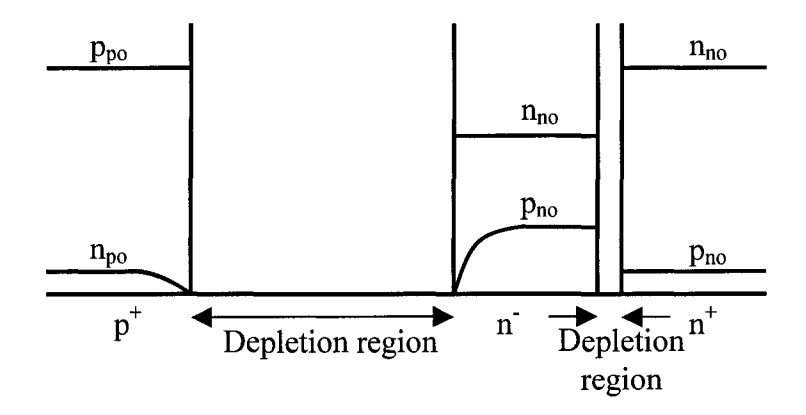


Figure 4.4: Carrier distribution diagram of a PIN photodetector under reverse bias. The increase of the depletion width is due to the applied reverse voltage and low doping concentration in the n region.

In the depletion regions of a PIN photodetector, since electric field exists in the region, therefore no free carrier is allowed to stay. However free carriers can be generated at room temperature via the trap levels. These free carriers are swept away by the electric field almost instantly when they are generated and resulted in a thermal generation current. The thermal generation current is described by the following equation:

$$J_{gen} = \frac{en_i w}{2\tau_o} \quad (4.7)$$

where w is the depletion width, n_i is the intrinsic concentration, $\tau_o = \tau_{po} + \tau_{no}$ where τ_{po} and τ_{no} are the lifetime for holes and electrons. The total reverse-bias current is the sum of the reverse saturation current (Eq. 4.6), the thermal generation current (Eq. 4.7) and the photogenerated current if the device is illuminated. Equation 4.8 describes the total

reverse-bias current, which is a function of depletion width, thus a function of applied reverse bias.

$$J_{\text{Re}\,\nu} = J_{s} + J_{\text{gen}} + J_{\text{photo}} = \left[\frac{eD_{p}p_{no}}{L_{p}} + \frac{eD_{n}p_{po}}{L_{n}} \right] + \frac{en_{i}w}{2\tau_{o}} + J_{\text{photo}}$$
 (4.8)

4.1.3. FORWARD BIAS

When a forward bias is applied to a PIN photodetector, the thermal equilibrium condition of the system is distorted. The built-in potential barrier is reduced by the applied voltage and the energy band bending is also reduced. An energy-band diagram of a PIN photodetector under forward bias is shown below:

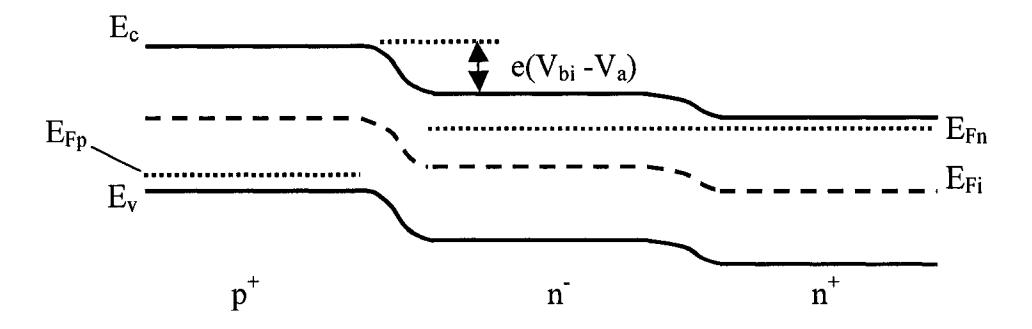


Figure 4.5: Energy-band diagram for a PIN photodetector under forward bias condition. V_a is the applied forward bias voltage.

Since the built-in potential barrier is reduced, more majority carriers can overcome the potential barrier and diffuse to the opposite side. The result is a majority carrier diffusion current which is larger than its thermal equilibrium value. However, the minority carrier drift current does not change since it is independent of the applied voltage. The total external current increases as the applied forward bias increases and can be derived based

on the minority carrier distribution [4.4]. The ideal diode forward current is expressed by the following equation:

$$J_D = J_s \left[\exp \left(\frac{eV_a}{kT} \right) - 1 \right] \quad (4.9)$$

where J_s is the saturation current defined in Equation 4.6. Under forward bias conditions, majority carriers from both side of the junction are injected across the depletion region and become minority carriers in the opposite region. Due to the nature of semiconductor, there is a possibility that the electrons recombine with holes in the depletion region and do not contribute to the minority carrier distribution. Therefore, an addition recombination current component has to be calculated in order to compensate for the carriers lose due to recombination. The recombination current is derived based on the probability of the trap capturing electrons and holes and is expressed as the following equation:

$$J_{rec} = \frac{ewn_i}{2\tau_o} \exp(\frac{eV_a}{2kT}) = J_{ro} \exp(\frac{eV_a}{2kT}) \quad (4.10)$$

where $\tau_o = \tau_{po} = \tau_{no}$. The total forward-bias current under low injection and dark conditions for a PIN photodetector is expressed as:

$$J_{forward} = J_{rec} + J_D = J_{ro} \exp\left(\frac{eV_a}{2kT}\right) + J_s \left[\exp\left(\frac{eV_a}{kT}\right) - 1\right]$$
(4.11)

The total forward-bias current is usually simplified to:

$$J_{forward} \sim J_s \left[\exp \left(\frac{eV_a}{mkT} \right) - 1 \right]$$
 (4.12)

where m is called the ideality factor. Under high injection conditions, large amount of minority carrier built up in the depletion region edges. The bulk regions need to maintain

charge neutrality and the majority carrier concentration has to increase above its equilibrium value. A carrier distribution plot for a forward biased PIN photodetector under low injection and high injection conditions is shown in Figure 4.6.

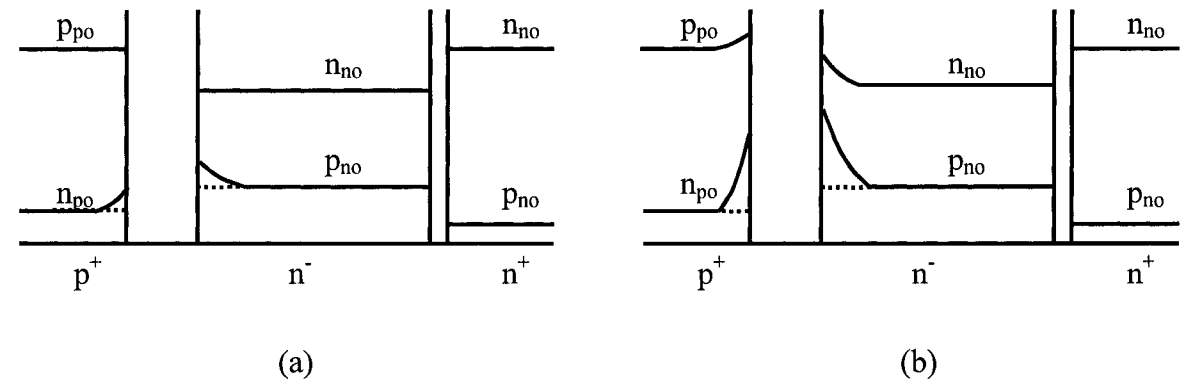


Figure 4.6: Carrier distribution for a forward biased PIN photodetector: a) Low injection, b) High injection.

Under high injection condition, the total diode current is lower than the ideal value due to the increase of recombination rate caused by the increase of excess majority and minority carriers in the depletion edges. A log scale plot for the ideal diode current (J_D) , recombination current (J_{rec}) and total forward current $(J_{forward})$ is shown in Figure 4.7. The plot shows that under low forward-bias voltage, the recombination current dominates and under high forward-bias voltage, the ideal current dominates. It also indicates that under high injection, ideality factor increases above 1.

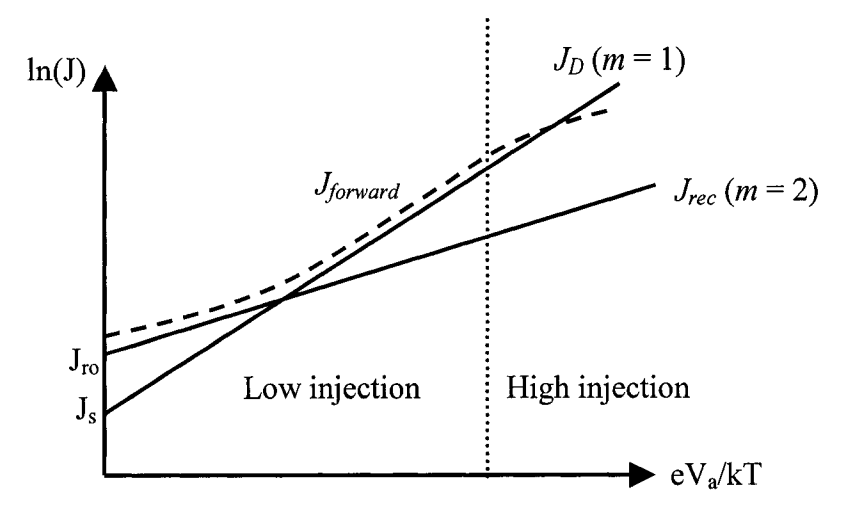


Figure 4.7: Ideal diode current (J_D) , recombination current (J_{rec}) and total diode current (J_{total}) in a forward-biased PIN photodetector.

4.1.4. PERIMETER RECOMBINATION CURRENT

The above theories consider only the carrier transport in the bulk region of the device. However in a mesa type PIN photodetector, perimeter recombination occurs in the edges of the device and contributes to an additional recombination current. This perimeter recombination current is dependent on the perimeter of the device and the total forward current equation is given below:

$$I_{forward} = J_{rec}A + J_DA + J_PP = J_{rec}A + J_DA + J'_{on}P\left[\exp\left(\frac{eV_a}{mkT}\right) - 1\right]$$

where J_{rec} and J_D are the bulk recombination current and bulk diffusion current given in Equation 4.11, J_p is the perimeter recombination current, J'_{on} is the perimeter recombination coefficient. A is the junction area and P is the junction perimeter. It is obvious that the perimeter recombination current becomes significant only in a large perimeter-to-area P/A ratio device. Research work has been done by other authors on the study of the orientation dependent perimeter recombination current [4.6]. However, this is not within the script of the thesis and the theory is not discussed in this work.

4.1.5. MINORITY CARRIER LIFETIME EXTRACTION

Minority carrier lifetime for a diode can be extracted from I-V measurements. For a PIN photodetector with a measurable reverse current, the minority carrier lifetime (generation lifetime) can be computed using Equation 4.8. Under dark condition, the equation can be rewritten as:

$$\tau_{o} = \frac{0.5en_{i}w}{J_{\text{Re}v} - \left[\frac{eD_{p}p_{no}}{L_{p}} + \frac{eD_{n}n_{po}}{L_{n}}\right]}$$
(4.13)

For a small size device, the reverse current may be too small to be measured accurately and therefore extraction of the minority carrier lifetime from the reverse current is difficult. J. Vanhellemont, E. Simoen and C. Claeys have proposed a method to extract the minority carrier lifetime from forward bias characteristics [4.5]. They suggested that the minority carrier lifetime could be calculated from a forward current (I_F) extrapolated to zero bias (I_{Fo}). In a first-order approximation, I_{Fo} for a p⁺n junction is given by:

$$J^{d}_{Fo} = e \sqrt{\frac{D_{n}}{\tau_{o}}} \frac{n_{i}^{2}}{N_{D}}$$
 (4.14)

where N_D is the doping concentration of the n⁻ region and J^d_{Fo} is the corrected value for bulk diffusion current which can be expressed by the following equation:

$$J^{d}_{Fo} = J_{D} \frac{0.5m}{1 - 0.5m} \quad (4.15)$$

where m is the ideality factor given in Equation 4.12 and J_D is the ideal diode current given in Equation 4.9.

4.2. MEASUREMENTS

Forward and reverse I-V measurements were performed on all the samples fabricated. The measurements were carried out under dark conditions unless otherwise specified. A semiconductor parameter analyzer model HP4145A was used in the measurements. I-V measurement results were consistence in all the good devices. Since large area devices (300 um x 300 um) were used and the corresponding P/A ratio were small, thus the perimeter recombination current was small and was neglected in the interpretation of Two set of the reverse current data for sample V1B are shown in measured results. Figure 4.8. From the measured results, it is evident that the generation current is significant at high reverse bias voltages (> 4 V) since the depletion width was large. At the low reverse bias region (< 4 V), the total current variation was small. The fact suggested that the generation current is small and the total reverse current is dominated by the saturation current. The measured results yield a saturation current in the order of 0.1 nA. The reverse current under illumination condition were also measured and the results show different current responses at different optical powers. The reverse current under illumination plot is shown in Appendix A.

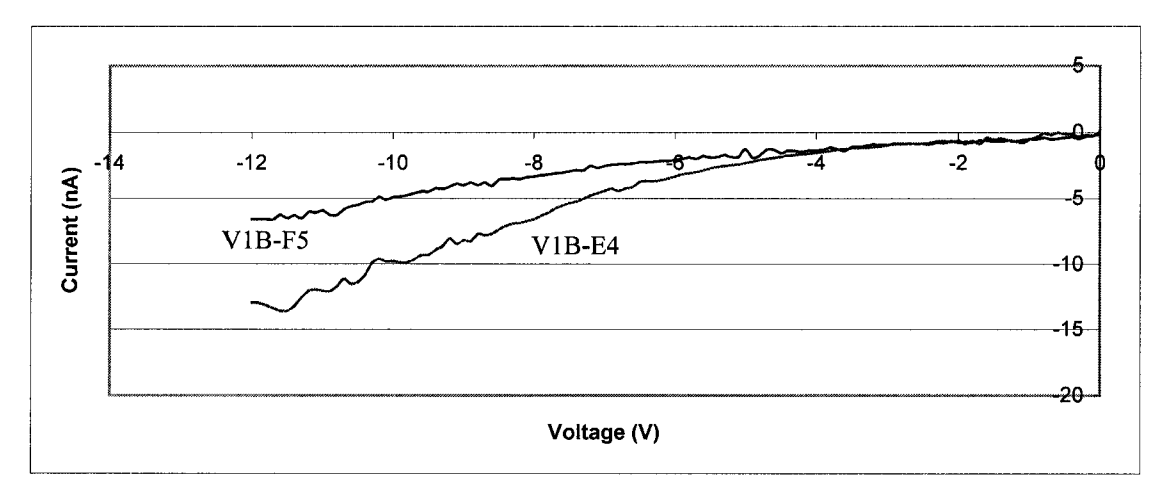


Figure 4.8: Selected reverse current vs. voltage data.

Forward I-V measurements showed a slightly different result among the samples V1A, V1B and V2A. Selected I-V data from the three samples are shown in Figure 4.9.

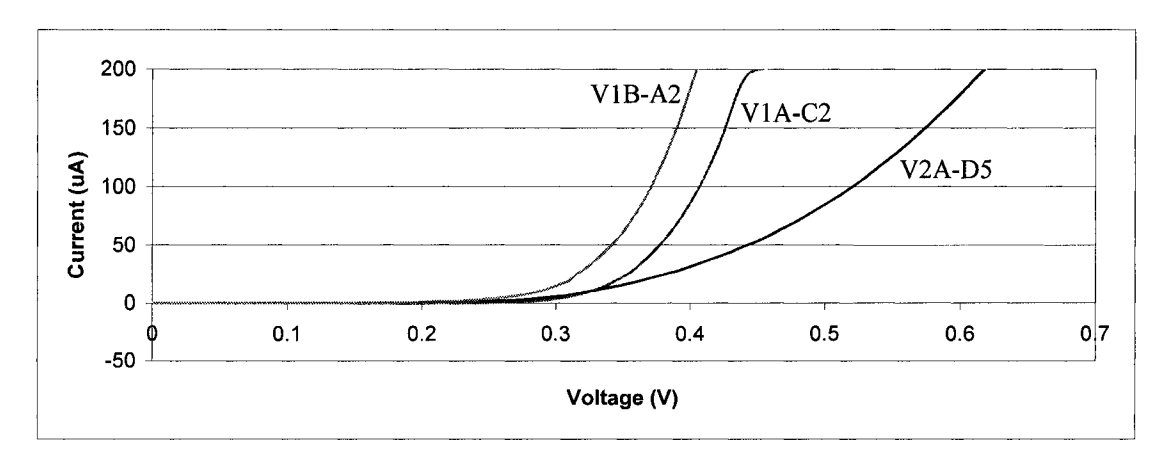


Figure 4.9: Selected forward IV data from sample V1A, V1B and V2A

The forward I-V results show that devices in V2A sample have a larger turn-on voltage than those in V1A and V1B. Hence, the saturation currents in the V2A sample are smaller. Since the saturation current was related to the doping concentration of the one-sided junction, thus the doping concentration in the n⁻ region of the sample V2A should have a lower concentration than those in sample V1A and V1B. The doping concentration in the n⁻ region for all samples is discussed in the C-V section. A log scale forward I-V plot is shown in Figure 4.10.

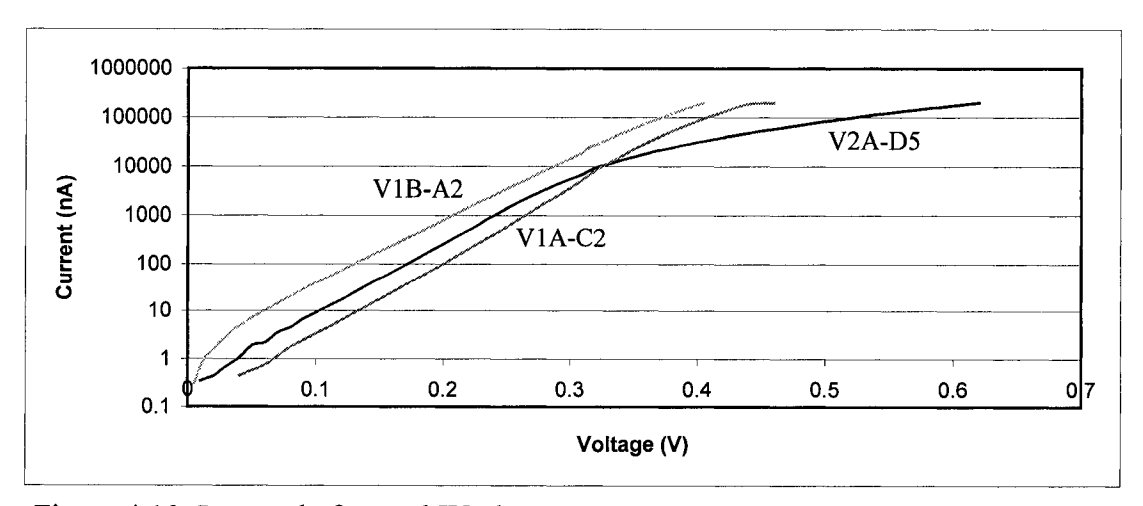


Figure 4.10: Log scale forward IV plot.

The measured data showed that the ideality factors m of all three samples were close to 1 in the low bias region and were greater in the high bias region (decrease in slope). Table 4.1 shows the value of the ideality factor m for all three samples with different bias conditions.

Table 4.1: Ideality factor (m) with different bias conditions.

Volt /	0.1	0.2	0.3	0.4	0.5	0.6
Ideality factor						
V2A-D5	1.128	1.148	1.581	3.205	4.577	5.821
V1A-C2	1.081	1.102	1.017	1.599	NA	NA
V1B-A2	1.207	1.302	1.372	2.460	NA	NA

The close to 1 ideality factor in the low bias region suggested that the recombination current component (J_{rec}) was small and the defect, recombination center, density was small in all the devices studied. The sample V2B showed a high ideality factor in high bias region corresponding to a high injection condition. Since the high injection condition in the sample V2A occurred earlier than those in samples V1A and V1B, thus the n⁻ region doping concentration in the sample V2A was lower. This predication agrees with the results obtained from the forward I-V measurements and will be verified in the C-V section. The average minority carrier lifetime (τ_0) was found based on the reverse I-V data using Equation 4.13 since the reverse current was measurable. Assuming the depletion width was 1.0 um at $V_R = 2$ V and n_i was 6.31×10^{11} cm⁻³. The computed average minority carrier lifetime (τ_0) was approximately equal to 10 ps.

4.3. SUMMARY

I-V measurement technique is a simple measurement method to characterize a PIN photodetector. From the I-V measurement data, it is found that the doping concentration

in the V1A sample is higher then that in V2A sample. The recombination current in both forward and reverse bias is small or insignificant indicates that the defect densities, recombination centers, are low. Using the I-V measurement technique, one can compare the performance between different photodetectors. It also helps to estimate the material quality of a device such as doping concentration, saturation current and turn-on voltage.

5. CAPACITOR-VOLTAGE MEASUREMENTS

The method of capacitor-voltage (C-V) measurements is a conventional technique to characterize a junction. The total capacitance of a junction changes as the applied bias varies. By studying the change of capacitance with voltage, depletion width and junction doping concentration can be computed [4.3].

5.1. THEORY

The capacitance of a pn junction consists of two components: junction capacitance and diffusion capacitance. Under reverse bias condition, only the junction capacitance is important while under forward bias condition, both components must be considered. In the following two sections, the theories of both junction capacitance and diffusion capacitance of a pn junction are discussed.

5.1.1. JUNCTION CAPACITANCE

The origin of junction capacitance is due to the present of depletion region in a pn junction [4.4]. The depletion region width can be computed using the following equation:

$$w = \left\{ \frac{2\varepsilon_s (V_{bi} + V_R)}{e} \frac{(N_a + N_d)}{N_a N_d} \right\}^{1/2}$$
 (5.1)

where N_a and N_d are the doping concentrations in the p and n region, V_{bi} is the built-in voltage of the junction and V_R is the applied reverse voltage. In the depletion region, positive and negative charges are separated in two regions. When a reverse bias is applied to the junction, the depletion region extends and the total number of storage charges changes. Figure 5.1 shows the change of depletion region of a reverse biased pn junction with the application of additional reverse voltage.

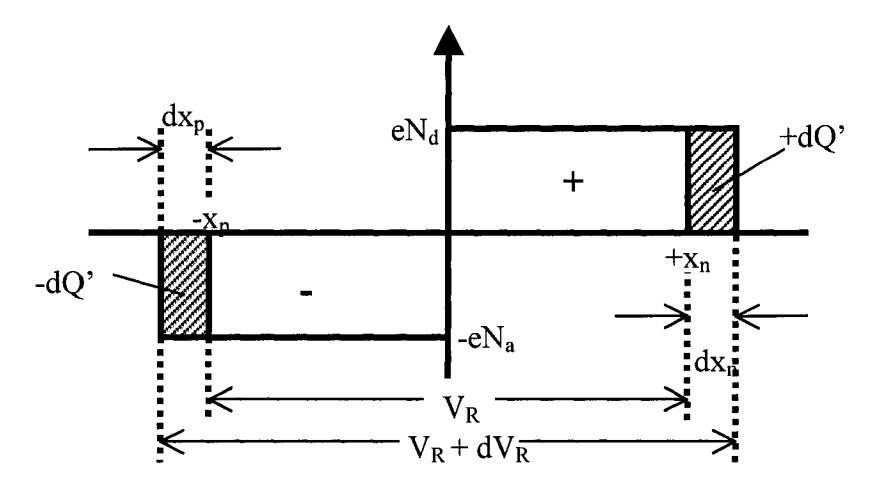


Figure 5.1: The change of depletion region of a reverse biased PN junction with the application of additional reverse voltage. V_R is the reverse bias, dV_R is the additional reverse bias, dQ' is the change of storage charge.

The junction capacitance of the pn junction shown in Figure 5.1 is defined as the change of storage charges due to the changes of applied voltage and is expressed as the following:

$$C' = \frac{dQ'}{dV_R} \qquad (5.2)$$

where

$$dQ' = eN_d dx_n = eN_d dx_p \qquad (5.3)$$

The change of charges dQ' has a unit of Coul/cm² and the junction capacitance C' has a unit of F/cm². It is more convenience to express the junction capacitance as a function of doping concentration and reverse bias. The junction capacitance equation can be rewritten as the following:

$$C' = \left\{ \frac{e \varepsilon_s N_a N_d}{2(V_{bi} + V_R)(N_a + N_d)} \right\}^{1/2}$$
 (5.4)

Since the junction capacitance is due to the existence of depletion region, thus the junction capacitance is also referred to as the depletion layer capacitance. Equation 5.5 is another expression for the junction capacitance when depletion width is known.

$$C' = \frac{\mathcal{E}_s}{w} \quad (5.5)$$

where w is the depletion width. From Equations 5.4 and 5.5, one can see that the junction capacitance is a function of reverse voltage (hence depletion width) and doping concentration.

5.1.2. ONE-SIDED JNCTIONS

One-sided junction is a special pn junction where the doping concentration on one side is much higher (usually 3 order or more) than the opposite side. For a PIN photodetector, one-sided junction exists in the p^+/n^- junction where $N_a >> N_d$. The depletion width of a one-sided p^+/n^- junction can be simplified to:

$$w = \left\{ \frac{2\varepsilon_s (V_{bi} + V_R)}{eN_d} \right\}^{1/2} \tag{5.6}$$

and the junction capacitance is:

$$C' = \left\{ \frac{e\varepsilon_s N_d}{2(V_{bi} + V_R)} \right\}^{1/2} \quad (5.7)$$

According to Equation 5.7, the junction capacitance is a function of the reverse bias voltage and the doping concentration in the lightly-doped region. Rearrangement of Equation 5.7 gives the following:

$$\left(\frac{1}{C'}\right)^2 = \frac{2V_{bi}}{e\varepsilon_s N_d} + \frac{2V_R}{e\varepsilon_s N_d}$$
 (5.8)

Equation 5.8 shows that the inverse squared capacitance is a linear function of applied reverse-bias voltage. Figure 5.2 shows a plot of Equation 5.8.

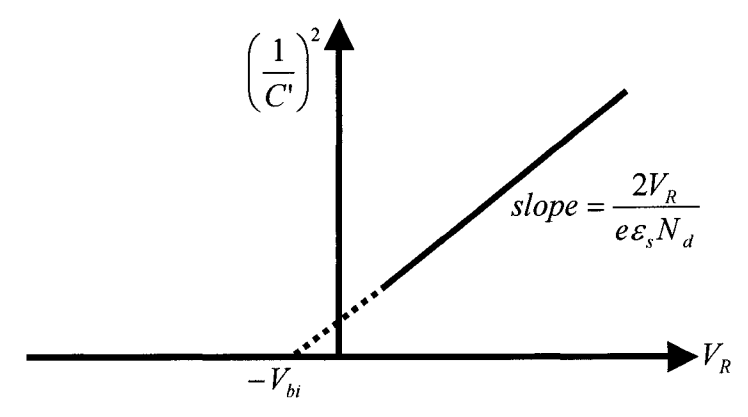


Figure 5.2: Inverse squared capacitance versus reverse-bias voltage for a one-sided junction.

This unique characteristic in a one-sided junction can be used to measure the doping concentration of the low-doped region and to measure the built-in voltage. The doping concentration N_d can be computed from the slope of the $1/C^{2}$ vs. V_R plot and the built-in voltage can be estimated by extending the line to the x-axis. This method can also be applied to Schottky junctions [5.1] and heterojunctions [5.2].

5.1.3. DIFFUSION CAPACITANCE

Diffusion capacitance is present only in a forward biased junction. When a pn junction is under forward biased condition, minority carrier tends to build up near the edge of the depletion region. The distribution of minority carrier density under forward bias in a PIN photodetector is discussed in Section 4.1.3. When an AC signal is applied to the forward biased junction, minority carrier density near the edge of the depletion region increases in the positive cycle while it decreases in the negative cycle. As a result, the junction is being charged and discharged by the AC signal and the total number of storage charges

changes correspondingly. A minority carrier distribution in a PIN photodetector with the application of AC signal is shown in Figure 5.3.

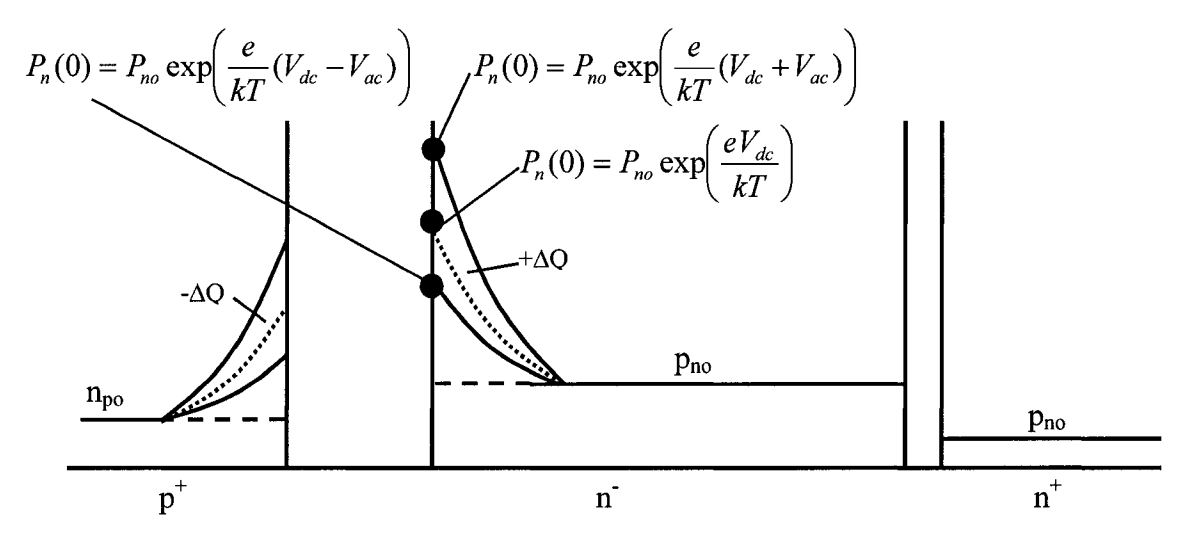


Figure 5.3: Minority carrier distribution in a forward biased PIN photodetector with the application of AC signal.

Since it takes time for the junction to be charged and discharged, the current response of the junction will be leading or lagging the AC signal resulting an imaginary part in the junction admittance [5.3]. The junction admittance is expressed as:

$$Y=g_d+j\omega C_d$$
 (5.9)

where C_d is the diffusion capacitance and is defined as the change in the stored minority carrier charge as a function of the change in voltage. Equation 5.10 gives an expression of C_d whereas the one for g_d (diffusion conductance) is given in Equation 5.11 as follows:

$$C_d = \left(\frac{1}{2V_t}\right) (I_{po}\tau_{po} + I_{no}\tau_{no})$$
 (5.10), and
$$g_d = \frac{I_{po} + I_{no}}{V_t}$$
 (5.11)

where V_t is the thermal voltage, I_{po} and I_{no} is the DC hole and electron current and τ_{po} & τ_{no} is the hole and electron lifetime.

5.2. MEASUREMENTS

C-V measurements were carried out on all samples. A Hewlett Packard model HP4274A multi-frequency LCR meter was used in the measurements. The measurements were performed under dark condition and parasitic capacitance was measured before each measurement. The parasitic capacitances were in the range from 1 to 5 pF. The magnitude of the AC signals for the measurements was set to the kT value (25 mV) and the signal frequency was set at 100 kHz, the highest available value from the equipment. The use of high AC signal frequency was required in order to minimize the effect of series resistance in the capacitance measurement. The DC bias voltage was measured separately by a multimeter model HP 3478A. The circuit mode of the photodetector was set in parallel mode. A schematic of the parallel circuit is shown in Figure 5.4.

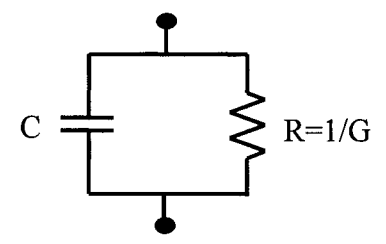


Figure 5.4: Parallel circuit representation of the photodetector used in the C-V measuring equipment.

where C is the capacitance and G is the conductance corresponding to the C_d and g_d given in Equation 5.9. At the beginning of the each measurement, a reverse bias voltage ($V_R = 12 \text{ V}$) was applied to the photodetectors. The reverse bias was then reduced at a small interval (0.2 V) and the capacitance was measured in each interval. In order to avoid the effect of transient capacitance, a one-second-delay time was set for each interval.

Capacitance was measured three times in high-resolution mode for each interval and the average value was recorded. The measured capacitance was in the range of 20 to 60 pF.

Results of C-V measurements from samples V-1-A and V-1-B were consistence while the results from sample V-2-A showed a significant difference. Plots of capacitance versus the reverse bias voltage for the three samples are shown in Figure 5.5.

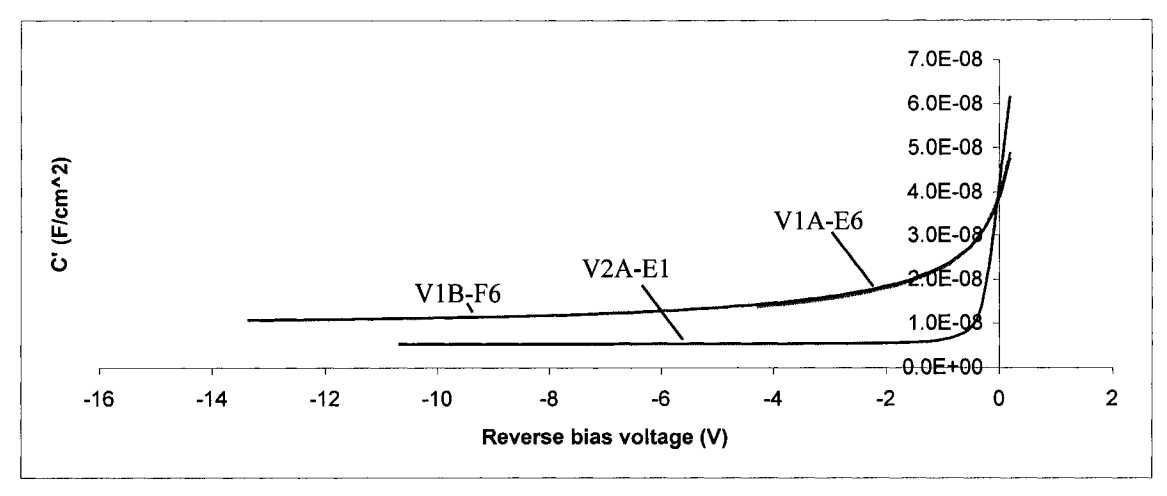


Figure 5.5: Capacitance vs. voltage plot for three samples.

All three samples had similar junction capacitance values (~ 40 nF/cm²) at zero bias. However, the capacitance in sample V2A decreased much faster as the reverse bias voltage increased. This rapid decrease in capacitance indicated that the depletion width in sample V2A increased faster than those in sample V1A and V1B according to Equation 5.5. Inverse squared capacitance versus reverse bias voltage for all the samples is plotted in Figure 5.6. The plot showed a decrease of slope in the high reverse bias region, especially in sample V2A. This change of slope indicated that the depletion region had been extended to the n⁺ region under high reverse bias according to Equation 5.8 and Figure 5.2. Due to the increase of doping concentration in the n⁺ region, the depletion width did not extend as fast as it was in the low doping n⁻ region, thus the change of capacitance decreased.

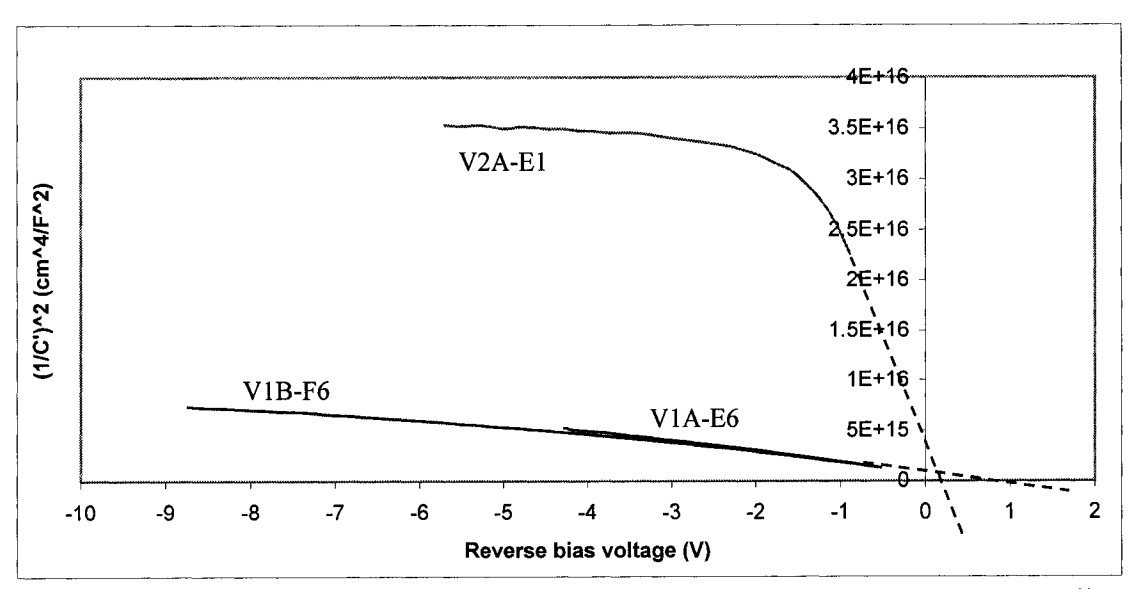


Figure 5.6: Inverse squared capacitance versus reverse bias voltage plot for all three samples.

The curves of $1/C^{2}$ vs. V_{R} plot for all three samples were extended linearly to the x-axis in order to estimate the built-in voltage of the photodetectors. The estimated built-in voltages were summarized in Table 5.1. Since the built-in voltage is a function of doping concentration of the junction (Eq. 4.5), assuming the doping concentration in the heavily doped p^{+} regions were the same for all the samples, from the estimated built-in voltages, one can conclude that the doping concentration of the n^{-} intrinsic region in sample V2A was lower than that of in samples V1A and V1B.

Table 5.1: Built-in voltage for all measured samples.

Sample number	Estimated built-in voltage (V)	
V1A-E6	0.5	
V1B-F6	0.5	
V2A-E1	0.25	

The doping concentrations and the corresponding locations in the intrinsic region of the photodetectors could be computed using the $1/C^{2}$ vs. V_R data. According to Figure 5.2, the slope of the $1/C^{2}$ vs. V_R curve is equal to $\frac{2V_R}{e\varepsilon_s N_d}$. From Equation 5.6, the depletion

width is a function of the doping concentration. Combining these two sets of data, the doping concentrations in the intrinsic region were found. The variation of doping concentrations versus distance for all the samples is plotted in Figure 5.7.

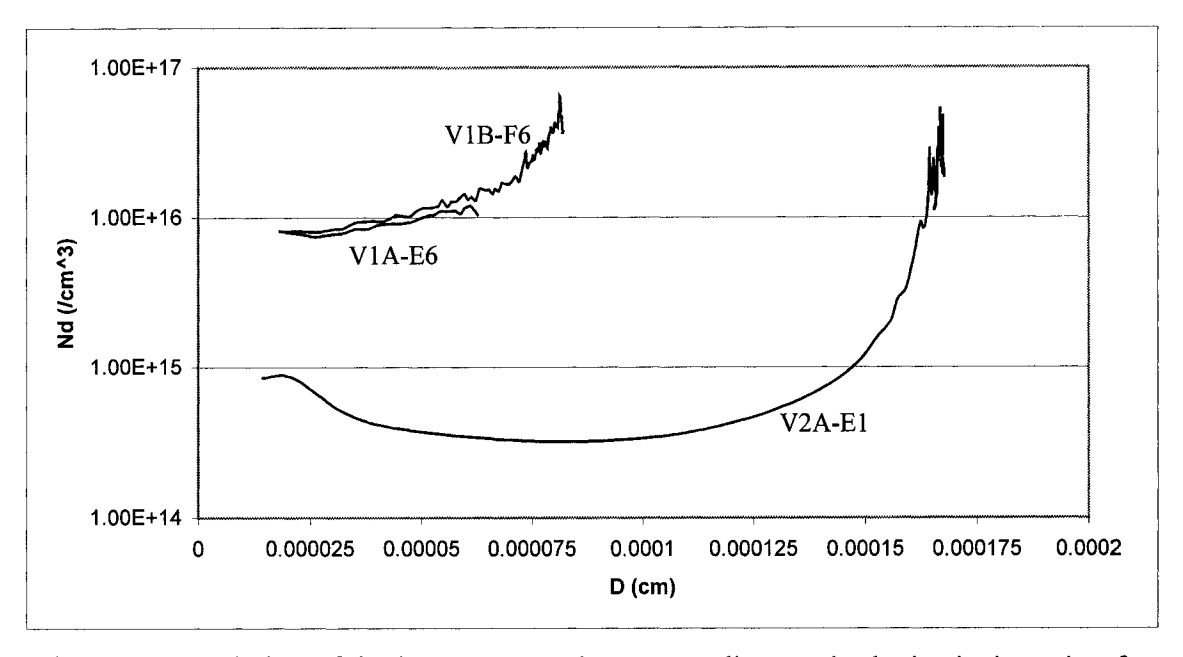


Figure 5.7: Variation of doping concentration versus distance in the intrinsic region for all three samples

According to the present result, the doping concentration in the n⁻ region of the sample V2A was around 15 times less than those in samples V1A and V1B and the n⁻ region width was more than double. Values of doping concentration and width of the n⁻ region are summarized in Table 5.2.

Table 5.2: n region doping concentration and n region width data.

		···
Sample	Minimum n region doping	Approximated n region width
	concentration (cm ⁻³)	(um)
V1A	8x10 ¹⁵	0.75
V1B	9x10 ¹⁵	0.75
V2A	3x10 ¹⁴	1.6

The low doping concentration in the n⁻ region in sample V2A as compared to those in samples V1A and V1B agreed with the measurement results obtained in the I-V section.

The doping concentration in the n⁻ region for the samples was controlled by the

fabrication process such as metal-organic chemical vapor deposition (MOCVD) [1.9] and molecular beam epitaxy (MBE) [1.10]. Using the C-V measurement technique, the characteristic of the n⁻ region, thus the quality of the manufacture processes was examined. According to the measurement result, the epitaxy process performed on sample V-2-A is better because of the well-controlled low doping concentration in the n⁻ region. The width of the n⁻ region was controlled by the Zn (p⁺ region) diffusion process; the deeper the diffusion, the shorter the n⁻ region. From the results of measurement, sample V1A and V1B had a narrow n⁻ region (wide p⁺ region) as compared to sample V2A.

5.3. SUMMARY

C-V measurement technique is a very useful method to characterize the photodetector. Using this technique, the built-in voltage, n⁻ region doping concentration and the depletion width of a PIN photodetector can be measured. In addition, it can also serve as a material quality examination technique for the epitaxy process. From the C-V measurement data, it is found that the n⁻ region doping concentration in sample V1A and V1B are high (close to 10¹⁶ cm⁻³) and it is reasonably low in sample V2A with a value in the order of 10¹⁴ cm⁻³.

6. ELECTRON BEAM INDUCED CURRENT MEASUREMENTS

Electron beam induce current (EBIC) method, also known as charge collection scanning electron microscopy, has been widely used in the semiconductor industry to study the material parameters for many years and is well documented [6.1] [6.2]. In this chapter, the EBIC method is used to determine the electric field distribution, carrier diffusion length and the surface recombination velocity.

6.1. THEORY

In a typical EBIC measurement, a pn junction is placed in a vacuum chamber and is connected to an ammeter in order to measure the induced current. The device has to be in closed circuit but not necessary to be under bias. In the present work, PIN photodetectors are used in the EBIC measurements. An electron beam is focused to the surface of the photodetector and allowed to incident normally. The electron beam is swept from the p⁺ region, across the intrinsic n⁻ region to the n⁺ region. A schematic diagram of the EBIC technique is illustrated in Figure 6.1.

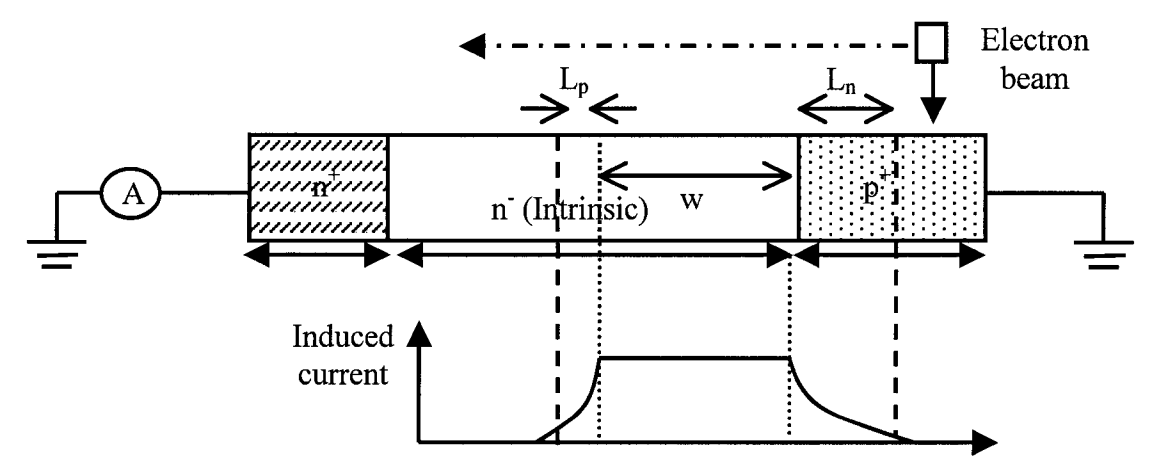


Figure 6.1: A schematic diagram showing the sample used in the EBIC experiment. L_n and L_p are the electron and hole diffusion lengths. w is the depletion region width.

The energetic electrons incident on the semiconductor collide with atoms and create electron-hole pairs along their paths. Since the n⁻/p⁺ junction in a PIN photodetector is a one-sided junction, therefore some of the free electrons created within an electron diffusion length from the metallurgical junction in the p⁺ region of the device will diffuse to the junction and be swept away by the built-in electric field. These free electrons will then drift across the depletion region and recombine in the n⁻ or n⁺ region to result in an induced current. The induced current reaches a maximum when the electron beam is incident on the intrinsic region where most of the electron-hole pairs will be swept by the electric field. The induced current diminishes as the electron beam is swept away from the hole diffusion length distance from the depletion region in the photodetector. Using the EBIC technique, the depletion region width of the PIN photodetector can be measured.

6.1.1. GENERATION VOLUME

The energetic electrons incident in the photodetector, accelerated by the electron gun usually with energy in the order of keV, lose energy during penetration by scattering from valence and core electrons while creating electron-hole pairs in the same time. As a result, these energetic electrons will be slowed down in the material as they lost energy. Furthermore, some of the energetic electrons may collide with the nuclei within the semiconductor atoms and be scattered to a path different from their original trajectories. The result of the slowed down and scattered electrons is creating electron-hole pairs not only under the electron beam focus point, but a generation volume. The generation rate is highest in the area close to the surface directly under the electron beam and is lower in the surrounding regions. The electron-hole pair generation volume is visualized by Cohn

and Caledonia [6.3]. In their experiment, a collimated electron beam is used to ionize a gaseous material and the fluorescent radiation emission caused by the electron beam is measured. A contour plot based on their result is illustrated in Figure 6.2. The contour plot can be universally applied to solid semiconductor with the distance scaled to the electron range R_e , which is the depth that an average electron could penetrate without large angle scattering.

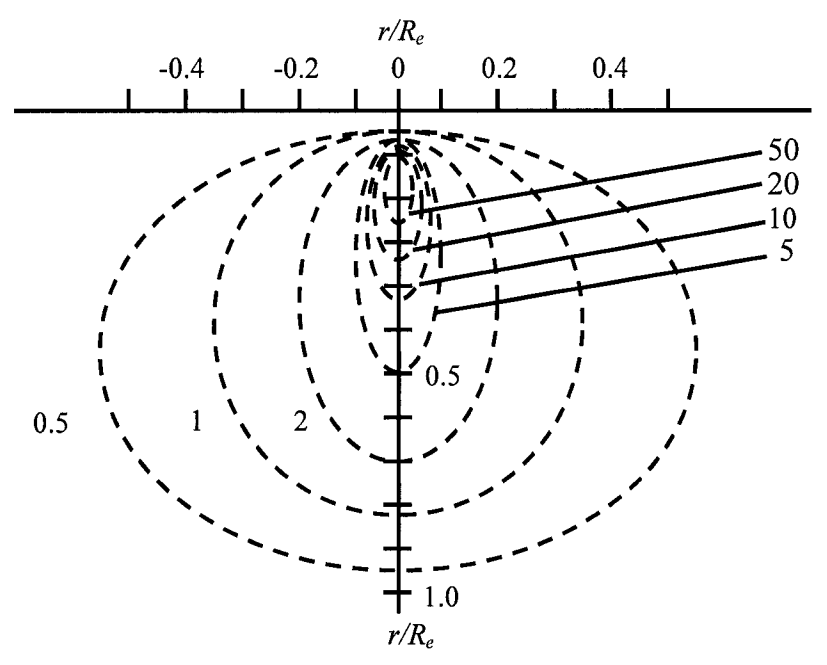


Figure 6.2: A contour plot based on Cohn and Caledonia s' result [6.3] showing the ionization rate of a gaseous material by a focus electron beam. The distance scales are normalized to the electron range $R_{\rm e}$.

6.1.2. ELECTRON RANGE

The electron range (R_e) is dependent on the electron beam energy and the semiconductor density. Several models for the electron range have been proposed by different authors [6.4] [6.5] [6.6]. A complete model for a broader range of electron beam energy is given by Everhart and Hoff [6.7]. The results from their work, the normalized Bohr-Bethe

range (\mathcal{R}_B) equations for different normalized electron energies (ξ) are illustrated in Table 6.1.

Table 6.1: Normalized Bohr-Bethe range equations for different normalized electron energies [6.7].

Normalized electron energy (ξ)	Bohr-Bethe range (\mathcal{H}_B)	
$5 < \xi = \frac{aE}{I} < 50$	$0.95 \cdot \xi^{1.51}$	
$10 < \xi = \frac{aE}{I} < 100$	$0.68 \cdot \mathcal{E}^{1.62}$	
$50 < \xi = \frac{aE}{I} < 500$	$0.34 \cdot \xi^{1.78}$	

In the normalized electron energy equation shown in Table 6.1, E is the electron beam energy in eV. The constant α has a value of 1.1658 [6.8]. I is the mean excitation energy for electron energy loss in the solid and is related to the atomic number (Z) of the material. An empirical formula for I [6.9] is shown below:

$$I = (9.76 + 58.8Z^{-1.19})Z(eV)$$
 (6.1)

 \mathfrak{R}_{B} is the normalized range where $\mathfrak{R}_{B}=R_{B}/K$, R_{B} is the Bohr-Bethe range (g/cm²) and K is equal to:

$$K = 9.40x10^{-12} I^2 A / Z(g/cm^2)$$
 (6.2)

where A is the atomic weight in gram. The electron range (R_e) is equal to:

$$R_e = R_B / \rho(cm) \tag{6.3}$$

where ρ is the material density in gram/cm³.

6.1.3. ELECTRIC FIELD DISTRIBUTION

Since the distribution of electron-hole pairs generated in the photodetector by the electron beam does not behave as a point source but a generation volume with a peak generation rate under the focus point of the electron beam, the ideal induced current

versus location plot shown in Figure 6.1 should be modified. Consider that 95% of the electron-hole pairs are generated within $0.1R_e$ distance horizontally from the focus point, the modified induced current plot should have a metallurgical junction located approximately $0.1R_e$ away from the peak induced current value. A modified induced current versus location plot is shown in Figure 6.3a where w_{lpeak} is the width of the peak induced current. The depletion width (w) in the photodetector can be expressed by the following equation:

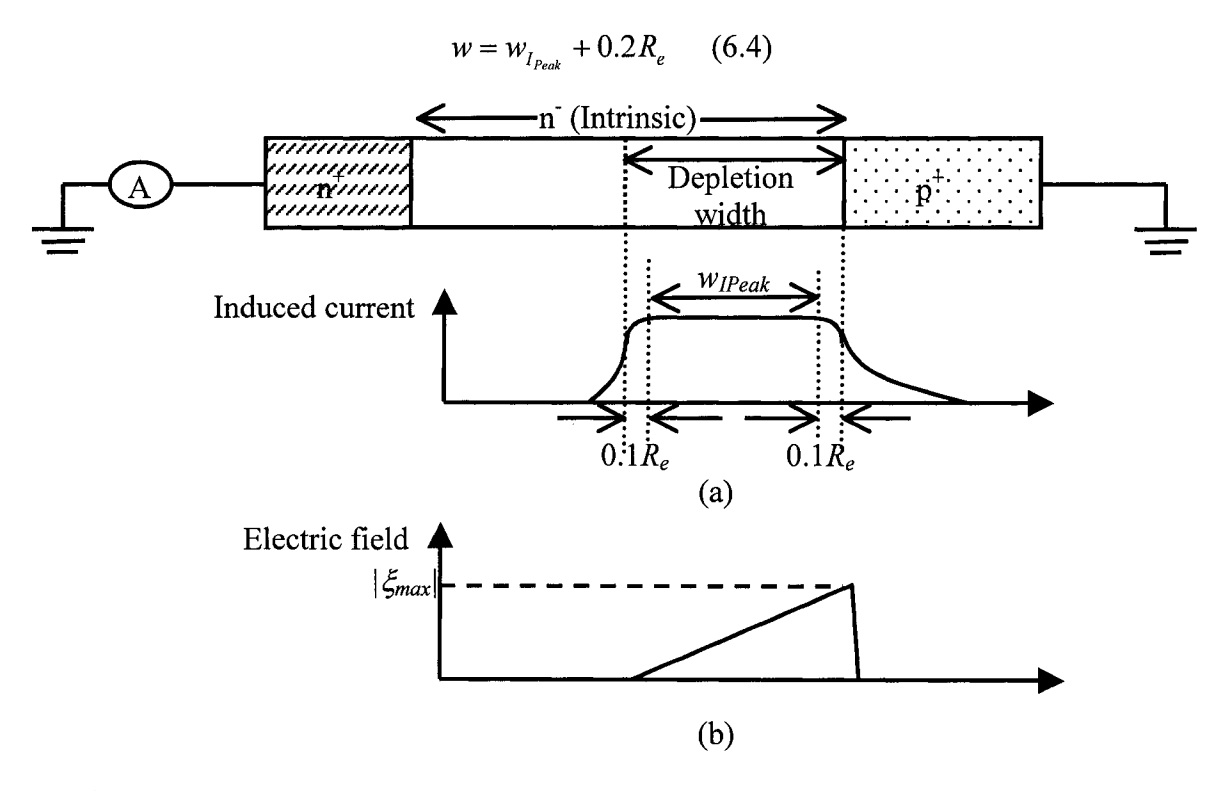


Figure 6.3: (a) A modified induced current versus location plot. (b) Electric field distribution in a PIN photodetector under zero bias.

The electric field of a PIN photodetector distributes entirely in the intrinsic region since the doping concentration of the p⁺ region is usually many orders of magnitude higher than that of the intrinsic region (one sided junction condition). The maximum electric

field ξ_{max} is located at the n⁻/p⁺ interface. The ξ_{max} can be computed once the depletion width is known by using the following equation:

$$\xi_{\text{max}} = 2V_{bi} / w \qquad (6.5)$$

where V_{bi} is the built-in voltage of the junction and can be found using a capacitance-voltage measurement technique discussed in the C-V section. It is noted that the electric field magnitude decreases linearly across the depletion region and reduces to zero at the end of the depletion region. An electric field distribution in a PIN photodetector under zero bias is shown in Figure 6.3b.

6.1.4. ELECTRON (MINORITY CARRIER) DIFFUSION LENGTH

The minority carrier diffusion length (L) is an important parameter in determining the performance of minority carrier devices, such as photodetector. There are many techniques to measure the diffusion length; some rely on photoluminescence [6.11] and some base on direct electron bombardment [6.10] [6.12]. In the present work, line scan EBIC technique is used to determine the electron diffusion length in the p^+ region of a PIN photodetector [6.13]. The EBIC technique has been discussed in the previous sections (Section 6.1.1 - 6.1.3). For diffusion length extraction, data analysis is focused on the rise of induced current close to the n^-/p^+ junction area. Since the rise of induced current is due to the increase of the carrier flux $D_e V \delta n$, assuming surface recombination is negligible, the rise of induced current can be described by the following equation:

$$I = I_{\text{max}} e^{-x/L} \qquad (6.6)$$

where L is diffusion length, I_{max} is the maximum induced current. However, the described model requires line fitting to determine the diffusion length and is heavily subjected to human and/or experimental errors. Improved techniques have been proposed

by different authors to compute the diffusion length directly from the EBIC data. V. K. S. Ong and D. Wu proposed a method to determine the diffusion length by taking the second derivative of the EBIC curve [6.14] using Equation 6.7 while L. L. Keung suggested another method by taking the negative of the inverted slope of the ln function of the EBIC curve [6.15] using Equation 6.8.

$$L = \sqrt{\frac{I_{EBIC}(x)}{\frac{\partial^2 I_{EBIC}(x)}{\partial x^2}}}$$
 (6.7)

$$L = -\left(\frac{\partial}{\partial x} \ln(I_{EBIC}(x))\right)^{-1} \quad (6.8)$$

All three methods mentioned above consider only point source generation within the material and do not consider the generation volume discussed in Section 6.1.1. Different diffusion length computation models with the consideration of different generation volume, ie cubic source, Gaussian source and true generation source, have been established [6.14] [6.15]. Using these computer simulation models, a more accurate diffusion length can be found. However, these methods involve complicated computer simulation software as well as time consuming finite element solving tools, and thus are not used in the present work.

6.1.5. SURFACE RECOMBINATION VELOCITY

In the previous discussion, the photodetector is assumed to have infinite horizontal dimension and the horizontal boundary conditions are not set at the semiconductor surface. In practice, the device has a finite size and surface states exist at the surface. The origin of surface states is due to the abrupt termination of material at the edges which leads to the end of periodic crystal lattice. This termination of crystal lattice results in the

disruption of the periodic-potential function and allows energy states to be positioned within the forbidden bandgap. An energy band diagram showing the deep energy level at the surface is shown in Figure 6.4.

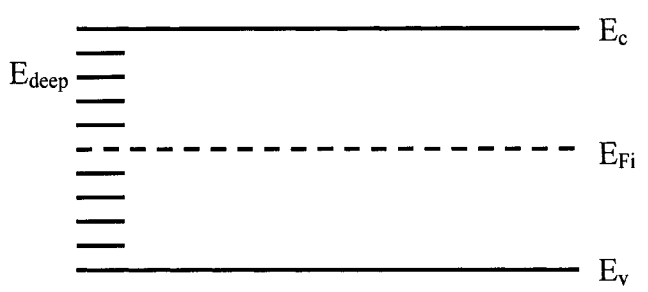


Figure 6.4: An energy band diagram showing the deep energy level at the surface

According to the recombination theory from W. Shockley and W. T. Read [6.16], the excess minority carrier lifetime is inversely proportional to the density of trap states. Since the density of traps or the deep level states is higher at the surface, thus the excess minority carrier lifetime at the surface is smaller than the one in the bulk region. The surface recombination rate is inversely proportional to the lifetime and is expressed as the following:

$$R_s = \frac{\delta n_s}{\tau_{nos}} \quad (6.9)$$

where R_s is the surface recombination rate, δn_s is the excess minority carrier density at the surface and τ_{nos} is the corresponding lifetime. Since the τ_{nos} is smaller than τ_{no} , thus R_s is always smaller than R_{bulk} . Figure 6.5 shows the excess minority carrier distribution at the edge of a material.

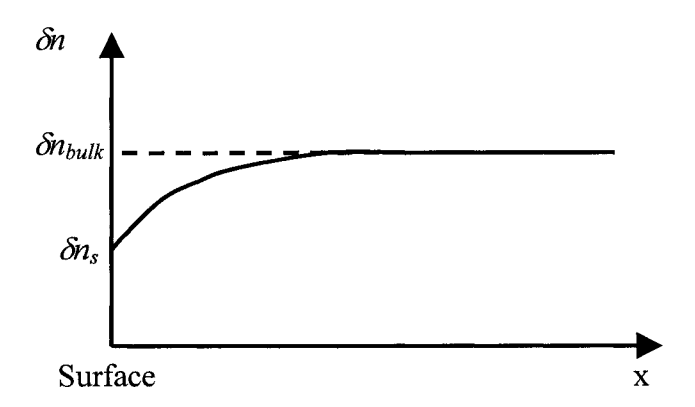


Figure 6.5: excess minority carrier distribution at the edge of a material

Due to the difference in the recombination rate between the surface and the bulk regions, a gradient in the excess carrier concentration exists near the surface as indicated in Figure 6.5. From the ambipolar equation (Eq. 4.2), the gradient in carrier concentration leads to a diffusion current which results in a current flowing from the bulk region to the surface of the material. The minority carrier concentration near the surface can be described by the following equation:

$$D_n \frac{\partial \delta n}{\partial x}\bigg|_{surface} = S \delta n \bigg|_{surface} \quad (6.10)$$

where S is defined as the surface recombination velocity and has a unit of cm/sec. In the EBIC measurements, if the electron range is short (excitation point too close to the surface), then a large number of the generated electron-hole pairs will be lost in the form proportional to the surface recombination velocity. This phenomenon is studied by M. Watanabe et al. [6.17]. They pointed out that the loss of electron-hole pairs in EBIC measurements due to surface recombination could be viewed as a decrease of excess carrier generation. The remaining carrier generation, the effective generation, is equal to

the ideal generation minus the loss in surface recombination and is described in Equation 6.11.

$$G_{eff} = G - G \frac{S}{1+S} \exp(-\frac{x}{L})$$
 (6.11)

where G_{eff} is the effective generation rate, G is the ideal generation rate, S is the surface recombination velocity, L is the diffusion length and x is the distance from the surface. By setting x close to 0, Equation 6.11 can be rewritten as:

$$\frac{\partial}{\partial x} \ln G_{eff} \Big|_{x=0} = \frac{S}{D} \quad (6.12)$$

where D is the diffusion coefficient and is related to the diffusion length. Consider the electron beam induced current is linearly proportional to the effective generation rate; parameter G_{eff} in Equation 6.12 can be replaced by I_{EBIC} . As a result, the surface recombination velocity can be expressed as:

$$S = D \frac{\partial}{\partial x} \ln I_{EBIC} \Big|_{x=0}$$
 (6.13)

Equation 6.13 indicated that the surface recombination velocity could be determined experimentally using EBIC technique by monitoring the change of induced current with different electron ranges.

6.2. MEASUREMENTS

6.2.1. ELECTRIC FIELD DISTRIBUTION

EBIC measurements were performed on the sample V1B using an SEM model number JSM-6100. An electron beam energy with electron energy of 10 keV was used. The EBIC results taken on several devices on the same sample were consistent. Figure 6.6 shows the EBIC results of the device V1B-D4 superimposed on the photodetector image

with a peak induced current of 4.3 nA. The electron range (R_e) was computed using Equation 6.3 and had a value of 0.99×10^{-4} cm using the following data: $Z_{InGaAs} = 36.5$, $A_{InGaAs} = 83.58$ and density = 5.489 g/cm³.

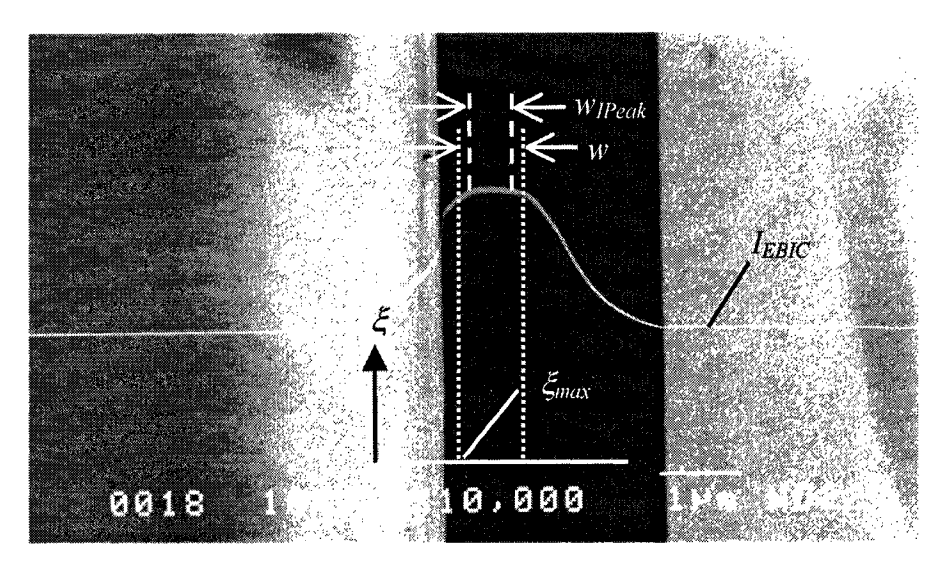


Figure 6.6: EBIC curve superimposed on the photodetector image. Electric field distribution corresponding to the exact location is shown. w is the depletion width. w_{IPEAK} is the induced current plateau.

The width of the induced current plateau of the plot shown in Figure 6.4 is $w_{IPeak} = 0.6$ um. The depletion width w of the detector at zero bias is computed using Equation 6.4 and a value of 0.798 um was obtained. The metallurgical junction was located 1.7 um from the edge of the detector, giving a p^+ region thickness of 1.7 um. The built-in voltage of the n^-/p^+ junction was found by using capacitance-voltage measurement technique and was equal to $V_{bi} = 0.5$ V. The maximum electric ξ_{max} of the device was 12.53 kV/cm computed using Equation 6.5. The electric field distribution corresponding to the exact location in the photodetector is plotted in Figure 6.6.

6.2.2. DIFFUSION LENGTH

Electron diffusion length was computed based on the measured EBIC data. Three methods of diffusion length computation were used. Method 1 employs the ideal induced current based on Equation 6.6. Method 2 uses the second derivative of the EBIC curve based on Equation 6.7. Method 3 relies on the inverted slope of the ln function of the EBIC data and was described by Equation 6.8. Results of diffusion length computation using the method 1 are shown in Figure 6.7. Three ideal induced current curves with different diffusion length were plotted on the same diagram to superimpose on the EBIC data. According to Figure 6.7, ideal induced current curve with diffusion length = 0.6 um matches the EBIC data well compared to others.

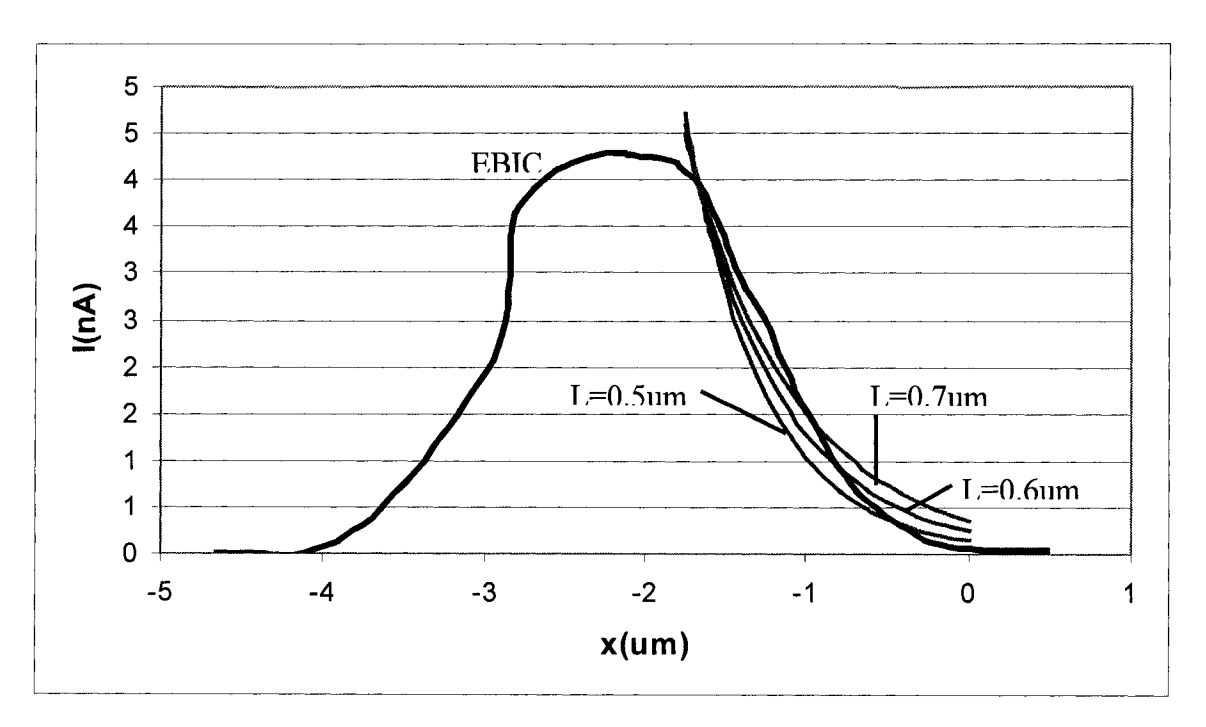


Figure 6.7: Diffusion length computation using method 1. Three ideal induced current curves with different diffusion length are plotted on the same plot superimpose of the EBIC data.

This result obtained was compared to the average diffusion length values obtained using methods 2 and 3. The results of diffusion length computation using methods 2 and 3 are shown in Appendices B and C. A comparison of the results for all three methods was summarized in Table 6.2. According to the computed results, the electron diffusion length should be in the range of 0.52 um to 0.60 um. However, the measured electron diffusion length was shorter than the theoretical value for typical InGaAs material which was in the order of 1 um [2.11]. It is believed that the diffusion length measured is for electrons within the heavily doped p⁺ InGaAs region. The introduction of large number of dopants reduced the mobility in the region and hence reduced the diffusion length.

Table 6.2: Computed diffusion length

Method	Electron Diffusion length (L _e)
Method 1	0.6 um
Method 2	0.56 um
Method 3	0.52 um

6.2.3. SURFACE RECOMBINATION VELOCITY

Several EBIC measurements were performed on sample V1B-D6 in order to gather data to compute the surface recombination velocity. The photodetector was under zero bias during the measurements and the settings for the experiments were the same as those used in Section 6.6.1, except for the electron beam energy. Electron beams with different energy values were used in order to create different electron ranges, thus different effective generation volumes. They were 10 keV, 6 keV and 2 keV. The measured EBIC results superimposed on the photodetector image are shown in Figure 6.8.

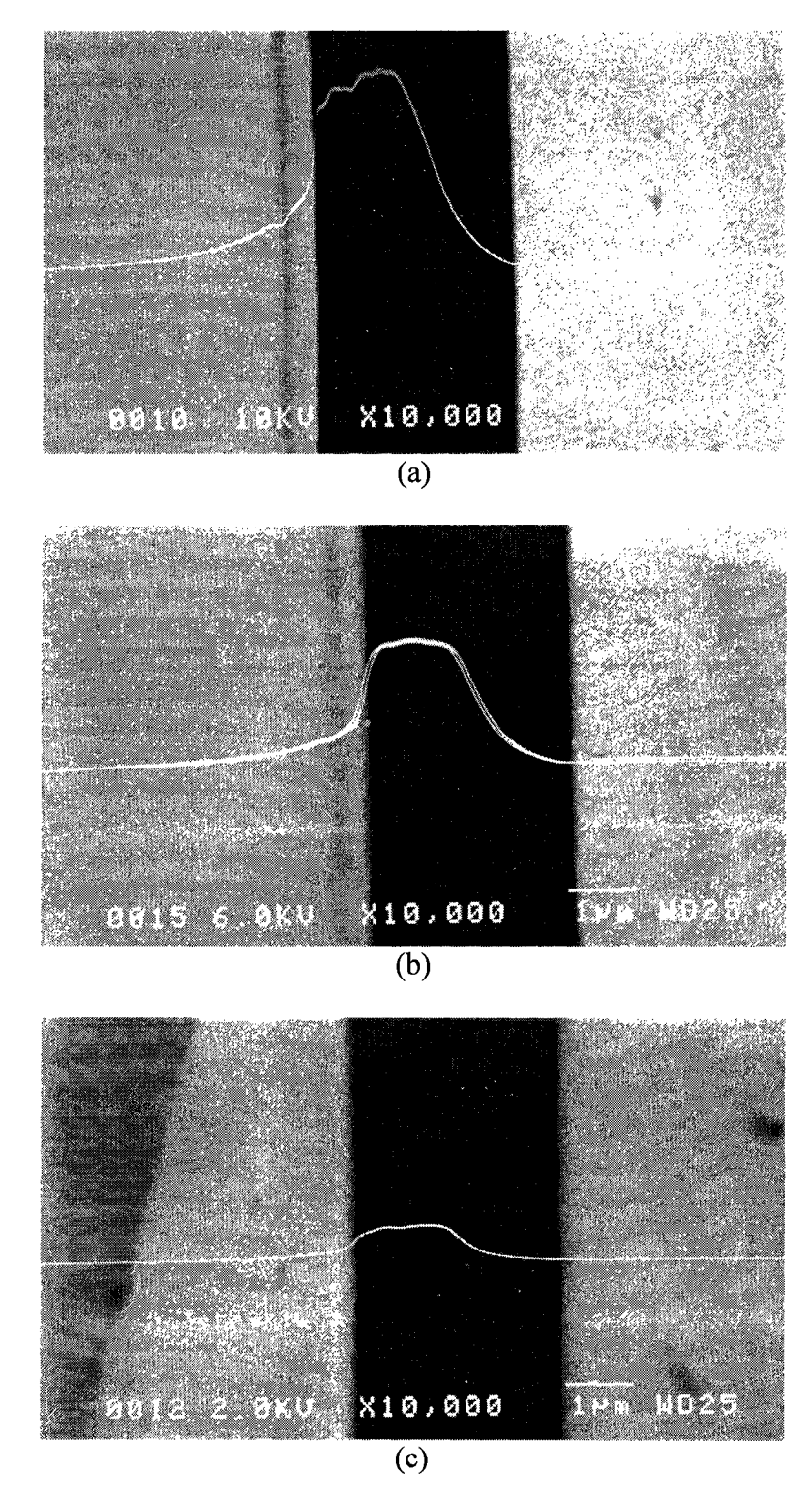


Figure 6.8: EBIC results superimposed on the photodetector image for different electron beam energy. (a) E = 10 keV, (b) E = 6 keV, (c) E = 2 keV.

Values of electron ranges R_e were computed using Equation 6.3 corresponding to each electron beam energy used and were summarized in Table 6.3.

Table 6.3: Values of electron ranges R_e corresponding to each electron beam energy used.

Electron beam energy	Electron range (R _e)	
10 ekV	0.99 um	
6 ekV	0.44 um	
3 ekV	0.084 um	

The center of the generation volume was located at a distance of $0.1R_e$ (Figure 6.2) from the surface and was used in the surface recombination computation. It is noted that the electron diffusion coefficient for InGaAs is $181 \text{ cm}^2/\text{sec}$ [5.3]. The surface recombination was computed using Equation 6.13 and had an average value of 40.2×10^6 cm/s.

6.3. SUMMARY

EBIC measurement technique is a very powerful method to characterize a PIN photodetector. Using this technique, the location as well as the strength of the electric field inside a PIN photodetector can be measured. Also the diffusion length and the surface recombination velocity of the device are retrieved. From the EBIC measurement data, the depletion width in the device V1B-D4 is found to be 0.798 um under zero bias. The diffusion length for the photodetector is retrieved and is in the range of 0.5 to 0.6 um. The surface recombination velocity is 40.2×10^6 cm/s.

7. EXCESS CARRIER DISTRIBUTION SIMULATION

The excess carrier distribution in a PIN photodetector is an indication of carrier transport in the device. By studying the excess carrier distribution, one can understand the effect of material parameters, thus can design an optimal structure to maximize the device performance. For a front illuminated mesa type PIN photodetector, since light is incident on the p⁺ region directly, thus a large number of carriers are generated in this region. These photogenerated carriers will diffuse in different directions and eventually recombine or sweep into the intrinsic region. However, the diffusion motion of carriers is a slow transport motion and it is very often the limitation of designing a high-speed photodetector. In this chapter, the excess carrier distribution in the p⁺ region is modeled in order to better understand the carrier motion in the photodetector. Previous works from other authors have constructed different device models using various approaches: S.P. Wilson et al have constructed a GaAs PIN photodetector model under high illumination conditions [7.1], E. Levy et al have simulated a three-dimensional excess carrier distribution in a semiconductor imaging array [7.2] and P. D. Yoder has built a SPICE model for high-speed PIN photodetectors [7.3]. The first two models are based on solving the ambipolar equation while the last one is constructed by considering the lumped circuit elements. In this work, the simulation method used is similar to the first two models which involve modeling by solving the ambipolar equation (Eq. 4.2). Computation is performed in a two dimensional space. The simulation is focused on the excess minority carrier in the p⁺ region under illumination with a structure similar to the commercial devices. Surface recombination is also considered in the modeling. Mathematical software package FlexPDE 3 from PDE Solutions Inc. [7.4] is used to

perform the simulation. FlexPDE 3 is a finite element model builder and numerical solver. It performs the operations necessary to turn a user input description of a partial differential equations system into a meshed finite element model, solves the system, and presents graphical output of the results.

7.1. THEORY

Carriers in a semiconductor can be transported by two methods: diffusion or drifting. The ambipolar equation (Eq. 4.2) described the carrier transportation according to the diffusion and drifting motion in time domain [4.3]. The equation is rewritten for electrons and is shown below:

$$D_{n} \frac{\partial^{2}(\delta n)}{\partial x^{2}} - \mu_{n} E \frac{\partial(\delta n)}{\partial x} + g_{p}' - \frac{\delta n}{\tau_{po}} = \frac{\partial(\delta n)}{\partial t} \quad (7.1)$$

The first term describes the diffusion motion due to concentration gradient and the section term describes the drifting motion due to electric field. The third and forth term describes the carrier generation and recombination in the material due to external factors (ie. photon) and under thermal equilibrium condition. All four terms are related to the change of carrier concentration in the time domain described in the right hand side of the equation. For steady state, the time domain term is set to zero. The equation can be used in multi dimensions by taking the derivative in the corresponding direction.

7.1.1. P⁺ REGION MODELLING

A p⁺ region of a front illuminated mesa type PIN photodetector is modeled in computer. The region has a circular cross section with a diameter of 5 um and a width of 1 um. Donut shape metal contact is placed on top of the region with an inner diameter of 3 um and outer diameter of 5 um. The p⁺ region structure is shown in Figure 7.1.

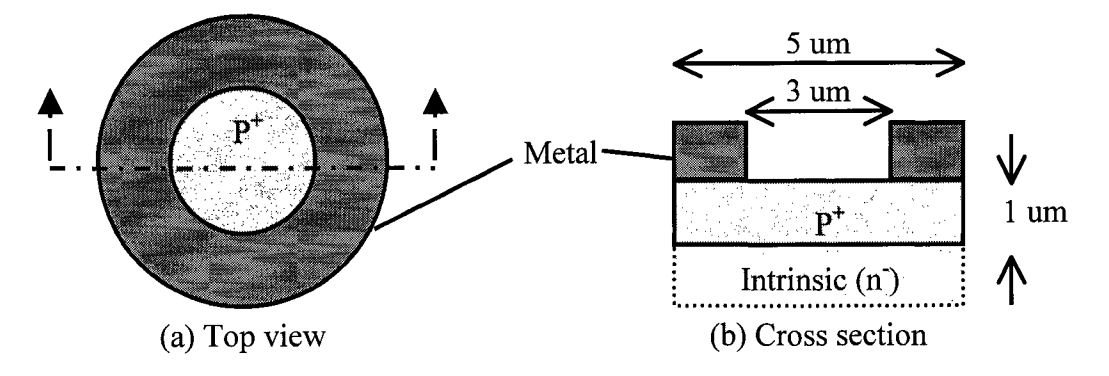


Figure 7.1: Computer modeled p⁺ region structure. (a) Top view, (b) Cross section

7.1.2. BOUNDARY CONDITIONS

Boundary conditions have to be defined in order for the software to solve the ambipolar equation. Since the device is assumed to be operated under reverse bias condition, thus the minority carrier concentration at the edge of the region adjacent to the delpletion region is equal to zero. Detailed explaination on the reverse bias of a photodetector is shown in Section 4.1.2. Assuming ohmic contact and perfect charge collection, minority carrier concentration in the regions with contact to metal is also equal to zero. For the rest of the regions, since they do not make contact with any material, thus the minority carrier concentration is not a fixed value. According to the surface recombination theory desicribed in secion 6.1.5, excess carrier concentration in the surface region is less than that in the bulk region due to the discontinuity of crystal lattice and is decribed by Equation 6.10. The boundary condition in these free regions can be set to a flux condition described by the surface velocity equation (eq 6.10). The boundary conditions in the free regions are expressed in Equation 7.2. A schematic diagram showing all the boundary conditions in the p⁺ region is shown in Figure 7.2.

$$\left. \frac{\partial \delta n}{\partial x} \right|_{surface} = \frac{S \delta n}{D_n} \left(7.2 \right)$$

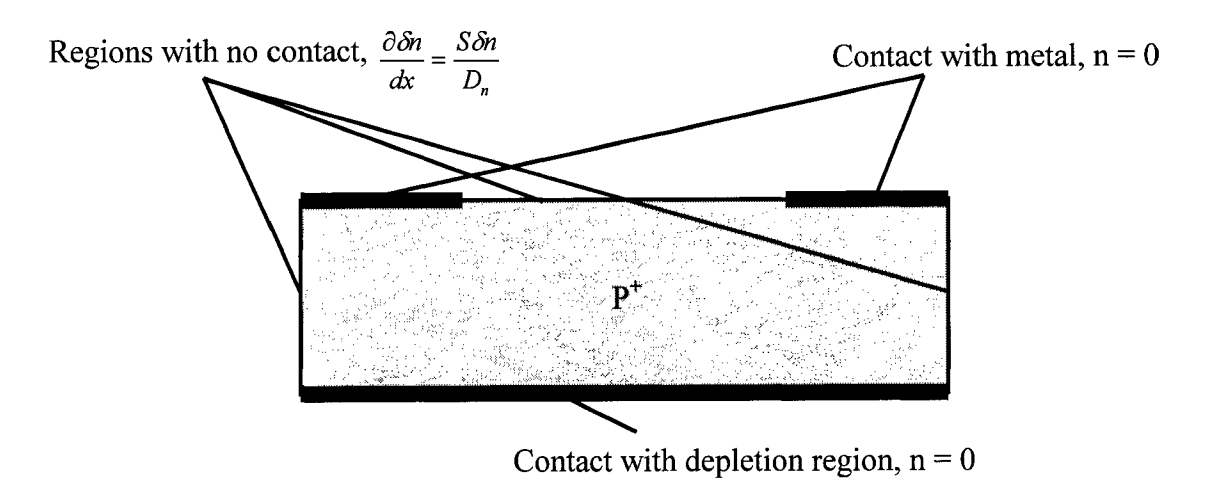


Figure 7.2: A schematic diagram showing all the boundary conditions in the p⁺ region.

7.1.3. PHOTON-INDUCED FREE CARRIER GENERATION

For a front illuminated PIN photodetector, since photons enter the device from the front side (p⁺ region), a large number of free carriers are induced by the incident photons in the region. At the same time, the photons are absorbed by the material as they travel within the solid. As a result, fewer photons can travel deep into the device. Since the free carriers generation is dependent on the number of incident photons, as the number of incident photons reduce in the deeper region, the number of carrier generation also decreases. This photon-induced free carrier generation is described by Equation 7.3:

$$g' = \Phi_o \alpha e^{-\alpha z} \qquad (7.3)$$

where Φ_0 is the incident photon flux (photons/sec/cm²) at the surface of the photodetector (z = 0), α is the absorption coefficient. For InGaAs material, the absorption coefficient for the 1.55 um communication wavelength is 10,000 cm⁻¹ [7.5]. The incident photon flux can be expressed as a function of incident power and wavelength and is described by Equation 7.4.

$$\Phi_o = \frac{P_{inc}}{Ahv} \qquad (7.4)$$

where P_{inc} is the incident optical power, A is the illuminated cross section, h is Planck's constant and v is optical frequency.

7.2. SIMULATIONS

The p⁺ region of a PIN photodetector was modeled in the computer using the description in Section 7.2 with a 5 um width and a 1 um depth. Metal contacts were placed at the top edge of the p⁺ section. The simulation code was included in Appendix D. Figure 7.3 shows the meshed computer model of the p⁺ region. Boundary conditions were set according to the description in Section 7.3 using the parameters measured in the previous sections: surface recombination velocity, $S = 40.2 \times 10^6$ cm/s and diffusion coefficient, $D = 181 \text{ cm}^2/\text{s}$.

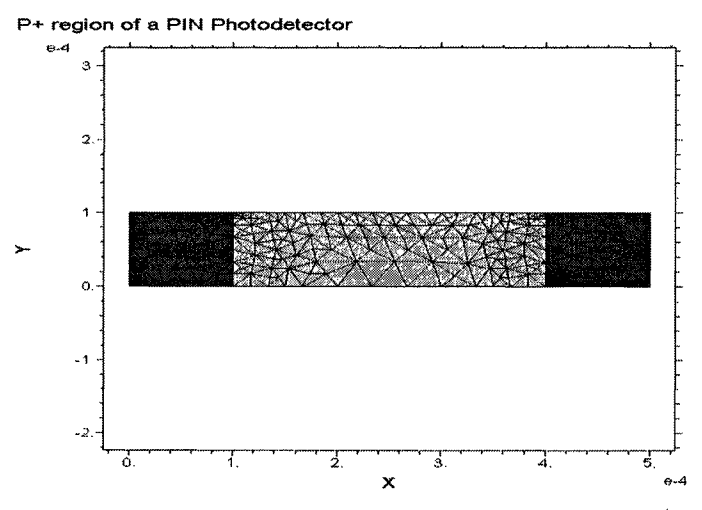


Figure 7.3: Mesh computer model of the p⁺ region. Yellow region is the illuminated region where the photon-induced carriers generated. Blue regions are the dark regions under metal contacts where no photon-induced carrier generated.

Photogenerated carrier concentration was computed using Equation 7.3 with absorption coefficient $\alpha = 10,000 \text{ cm}^{-1}$. The input photons flux Φ_0 was computed using Equation 7.4.

Assuming the incident optical power $P_{inc} = 0.1 \text{ W/cm}^2$ at a wavelength $\lambda = 1.55 \text{ um}$, the photo flux had a value of $7.8 \times 10^{17} \text{ cm}^{-2} \text{s}^{-1}$. Figure 7.4 shows the photogenerated carrier distribution in the p⁺ region. The maximum carrier generation is at the surface of the region with a generation rate equal to $1.429 \times 10^{20} \text{ cm}^{-2} \text{s}^{-1}$. The minimum carrier generation is at the bottom of the region with a generation rate of $5.256 \times 10^{19} \text{ cm}^{-2} \text{s}^{-1}$. Regions under metal contacts where no photon could penetrate do not have any photogenerated carrier.

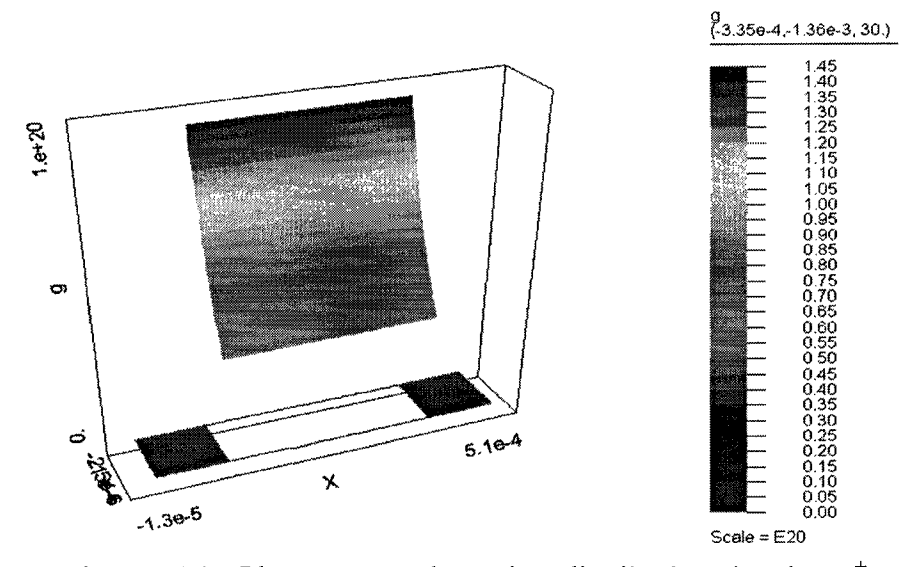


Figure 7.4: Photogenerated carrier distribution in the p⁺ region.

Using the constructed p⁺ region with boundary conditions and the photogenerated carrier data shown in Figure 7.4, a two dimensional excess carrier distribution was obtained. A 3-D excess carrier distribution plot is shown in Figure 7.5 and the corresponding contour plot in Figure 7.6. The excess carrier concentration shows a peak in the upper center of the region. This is due to the large number of excess carriers generated in the centerilluminated region and they diffuse to all other directions.

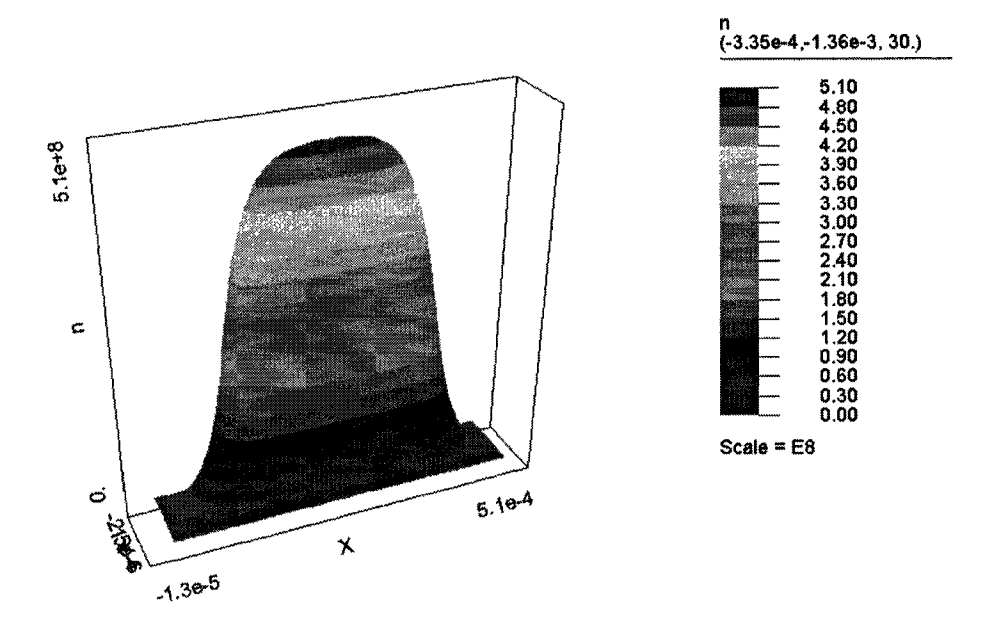


Figure 7.5: A 3-D excess carrier distribution plot.

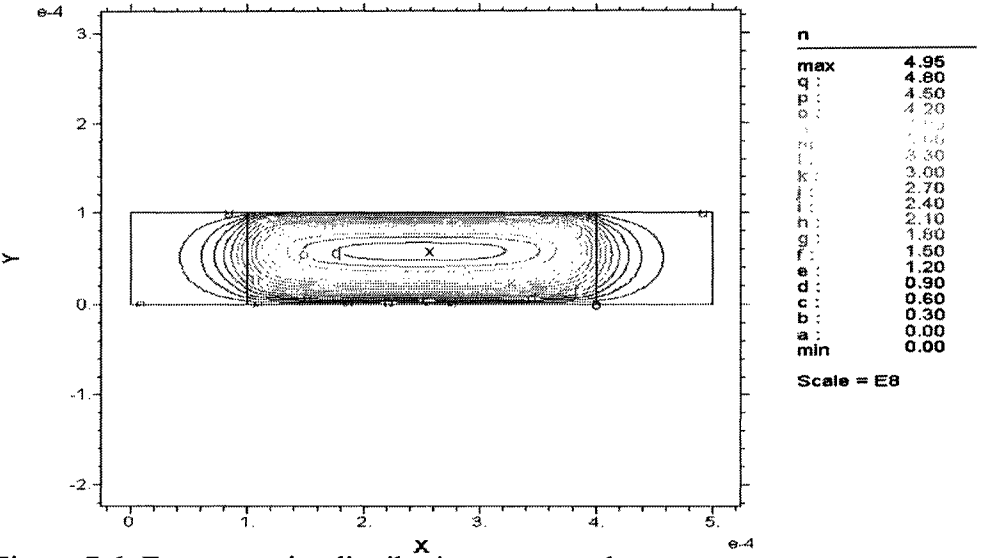


Figure 7.6: Excess carrier distribution contour plot.

Excess carrier concentrations at different horizontal (x) positions in the p^+ region are plotted in Figure 7.7. The maximum excess carrier concentration is located at the middle of the illuminated region (x = 2.5 um) at a depth of 0.4 um from the surface or 0.6 um from the depletion region with a value of $5 \times 10^8 \text{ cm}^{-3}$. The corresponding carrier concentration at the edge of the depletion region is zero and is around $1 \times 10^8 \text{ cm}^{-3}$ at the

surface (1 um from the depletion region) of the illuminated region. This is due to the surface recombination factor. The excess carrier concentration is reduced in regions away from the center. At the edge of the illuminated region (x = 4 um), the peak concentration is 2.5×10^8 cm⁻³ and the value decreases rapidly in the dark region (x > 4 um). The rapid decrease of excess carrier density in the dark region is due to the short lifetime of the carriers which lead to high recombination rate and the absence of photogenerated carriers. There is virtually no excess carrier at the edge of the detector (x = 5 um).

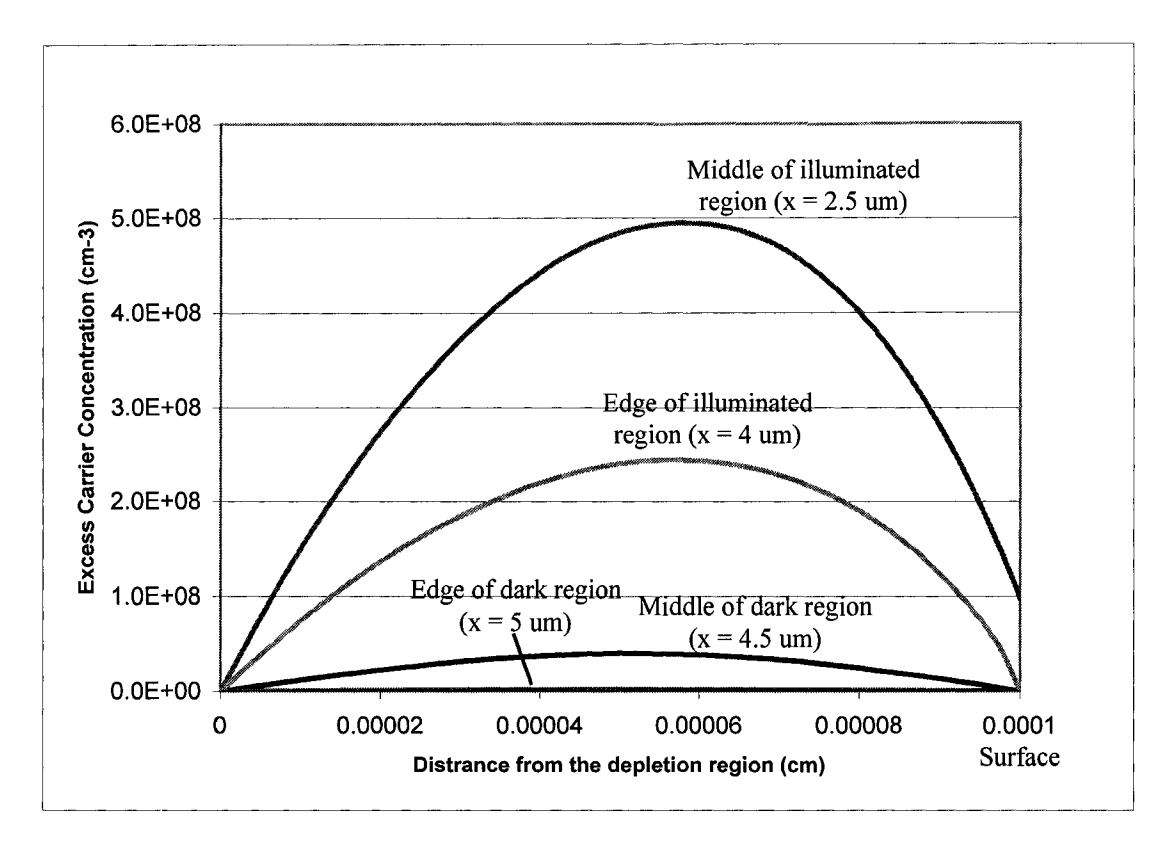


Figure 7.7: Variation of excess carrier concentration with distance in the p⁺ region.

Excess carrier concentration at a depth of 0.4 um (0.6 um from depletion region) and at the top surface of the p⁺ region are plotted in Figure 7.8. The plot indicates the rapid

decay of excess carrier concentration in the dark region. The low excess carrier concentration at the surface of the photodetector, even in the illuminated region, is due to the large surface recombination velocity.

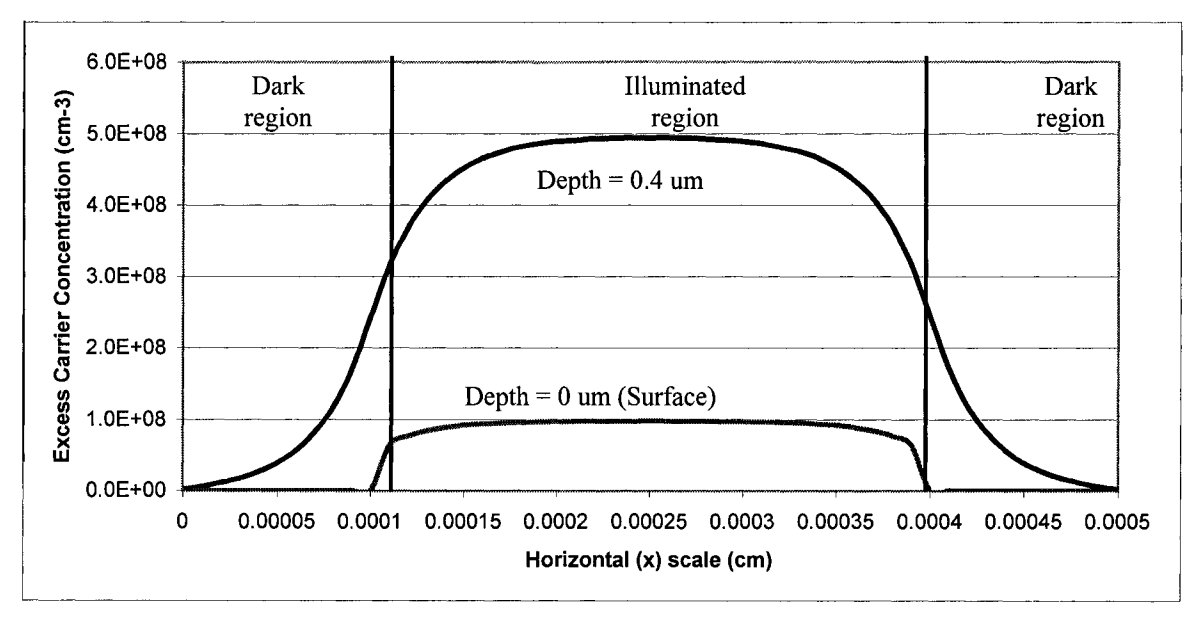


Figure 7.8: Variation of excess carrier concentration with distance at different depths in the p⁺ region.

7.3. SUMMARY

The simulation computes the distribution of excess carrier in a PIN photodetector under illumination according to the measured parameters. It helps to visualize the transport of carriers in the device in different regions and hence helps to design a better performance PIN photodetector.

8. DEEP LEVEL TRANSIENT SPECTROSCOPY

Deep level transient spectroscopy, DLTS, is a high-frequency capacitance transient thermal scanning method used to measure a wide variety of traps, deep states, in semiconductor materials [8.1]. This method is first introduced by D. V. Lang from Bell Laboratories in 1974 [8.2]. In the present work, DLTS technique is used to measure deep state energies and the corresponding densities in an InGaAs/InP photodetector.

8.1. THEORY

For a defect free crystalline semiconductor, the energy band diagram consists of a valence band and a conduction band separated by an energy band gap. When the periodicity of the single crystal is disturbed by foreign atoms or crystal defects, discrete localized energy levels are created within the band gap. These localized energy levels or defect states are generally categorized into two groups: shallow states and deep states.

8.1.1. SHALLOW STATES

Shallow states are generally introduced as dopant atoms to convert the type (n-type or p-type) of the host semiconductor. These states usually are related to substitutional impurities [4.2] where a dopant atom replaces an atom in a crystal structure. Shallow states are located near the band edges: near the conduction band for n-type dopant and near the valence band for p-type dopant. They are readily ionized at room temperature and the associated ionization energy can be approximated by a modified hydrogenic model [4.2]. Shallow state concentration can be determined electrically by using Hall effect measurements [8.3] and the energy levels are best measured optically due to their radiative nature.

8.1.2. DEEP STATES

Deep states refer to all the energy levels that reside deeper in the energy band gap then the hydrogenic states. Deep states can be used to reduce the carrier lifetime or to increase the material resistively by acting as a recombination center. However, most of the deep states are unintentionally incorporated during crystal growth and device fabrication. Deep states can be resulted from crystallographic point defects, structural defects or foreign impurities. The deep state energy levels as well as density can be determined using the DLTS measurements.

Deep states can be classified as acceptor-like or donor-like states. An acceptor-like state is a positively charged deep state when empty or a neutral deep state when occupied by an electron. A donor-like state is a negatively charged deep state when occupied by an electron or a neutral deep state when empty. There are four different transition methods for a carrier to transit between deep state and energy band. They are 1) electron capturing by a deep state from conduction band, 2) electron emission from a deep state to the conduction band, 3) hole capturing by a deep state from the valence band, and 4) hole emission from a deep state to the valence band. Figure 8.1 shows the four transition methods.

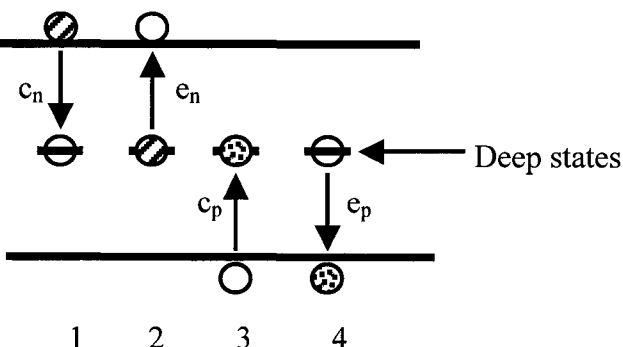


Figure 8.1: Four carrier transition methods between deep state and energy band. c_n is capture of electron, e_n is emission of electron, c_p is capture of hole and e_p is emission of electron.

A recombination event occurs when transition 1 followed by transition 3. A generation event occurs when transition 2 followed by transition 4. In such cases, the deep state acts as a recombination or generation center in the semiconductor material. An electron trapping occurs when transition 1 followed by transition 2 and a hole trapping occurs when transition 3 followed by transition 4. In these cases, a carrier is captured and emitted back to its original band.

8.1.3. DEEP STATE STATISTICS

The status of deep states and their interaction within energy band under thermal non-equilibrium conditions can be studied by Shockley-Read-Hall [6.16] recombination-generation statistics. A brief overview of the recombination-generation statistics [8.4] is shown in the following paragraph.

Assuming nondegenerate semiconductor material is used, the electron density in the conduction band can be reduced by increasing the electron capture process and can be increased by increasing the electron emission process. The rate of change of electron density in the conduction band is expressed by:

$$\frac{dn}{dt} = e_n n_T - c_n n p_T \tag{8.1}$$

where n is the electron density in conduction band, n_T is the electron occupied deep state density and p_T is the empty deep state density. The first term in Equation 8.1 represents the emission rate of electron while the second term represents the capture rate. The second term has an additional parameter, n, which indicates the capture rate is dependent on the electron density in the conduction band. The density of electron in the conduction band has to be greater than zero in order for a capture transition to occur. The first term does not has such parameter, it is because most of the energy levels is empty in the

conduction band and the emission process does not need to wait for an empty energy level most of the time. A similar equation for the rate of change of hole in valence band is expressed below:

$$\frac{dp}{dt} = e_p p_T - c_p p n_T \quad (8.2)$$

where p is the hole density in valence band. The rate of change of electron occupancy in a deep state can be expressed by comparing the rate of change of hole in valence band with the rate of change of electron in conduction band. It is given by:

$$\frac{dn_T}{dt} = \frac{dp}{dt} - \frac{dn}{dt} = (c_n n + e_p)(N_T - n_T) - (c_p p + e_n)n_T$$
 (8.3)

where N_T is the total deep state density and can be expressed as:

$$N_T = p_T + n_T \quad (8.4)$$

Assuming the electron and hole density, n and p, remain constant, Equation 8.3 can be solved and the solution is given as:

$$n_T(t) = n_T(0)e^{-t/\tau} + \frac{e_p + c_n n}{e_n + c_n n + e_p + c_n p} N_T(1 - e^{-t/\tau})$$
 (8.5)

and

$$\tau = \frac{1}{e_n + c_n n + e_n + c_n p}$$
 (8.6)

The electron occupied deep state density n_T in steady-state as $t \rightarrow \infty$ can be expressed as:

$$n_{T}(\infty) = \frac{e_{p} + c_{n}n}{e_{n} + c_{n}n + e_{p} + c_{n}p} N_{T}$$
 (8.7)

Equation 8.7 related the electron occupied deep state density n_T to the deep state density N_T and the capture and emission coefficients $c_{n/p}$ and $e_{n/p}$. However, these capture and emission coefficients are not constant and are related to each other. They are subjected to

temperature changes. According to the Principle of Detailed Balance [8.3], the capture and emission coefficients are related by the following equations:

$$e_p = c_p N_v \exp[(E_v - E_T)/kT]$$
 (8.8)

$$e_n = c_n N_c \exp[(E_T - E_c)/kT]$$
 (8.9)

where N_c and N_v are the effective state density in conduction and valence band, E_T is the deep state energy. Equations 8.8 and 8.9 are strictly valid under equilibrium conditions and are good approximately under non-equilibrium conditions. The capture coefficient $c_{p/n}$ is the ability for a deep level to capture an electron or a hole. A carrier is said to be captured if it travels into an imaginary sphere surrounding a deep level. The capture coefficients are expressed as:

$$c_n = \sigma_n v_{th} \quad (8.10)$$

$$c_p = \sigma_p v_{th} \quad (8.11)$$

where σ_e , σ_p are the imaginary capture sphere section for electron and hole. V_{th} is the carrier average thermal velocity and is expressed as:

$$V_{th} = \sqrt{\frac{3kT}{m_{n/p}^*}}$$
 (8.12)

where $m_{n/p}^*$ is the effective carrier mass. Combining Equations 8.8, 8.9, 8.10 and 8.11, a useful equation relating the emission coefficient, temperature and deep state energy is obtain and is shown below:

$$\frac{e_n}{T^2} = \gamma_n \sigma_n \exp[-(E_c - E_T)/kT] \qquad (8.13)$$

where γ_n is a material specific constant.

8.1.4. DEEP STATES IN A PIN PHOTODETECTOR

In the depletion region of a PIN photodetector, since the energy band diagram is bent (refer to Figure 4.1), thus the deep state energy levels in this region are distorted and are not uniform across the depletion region. Assuming the deep state energy levels are resided in the middle of the energy band gap for a one sided PIN photodetector, then in the depletion region, certain portion of the deep states are located above the quasi-Fermi energy level in the n⁻ region while the others are located below it. According to the solid-state theory [4.2], energy states are more likely to be occupied if they are below the quasi-Fermi energy level. Under thermal equilibrium and steady state conditions, the deep states occupation in the depletion region is described by Figure 8.2.

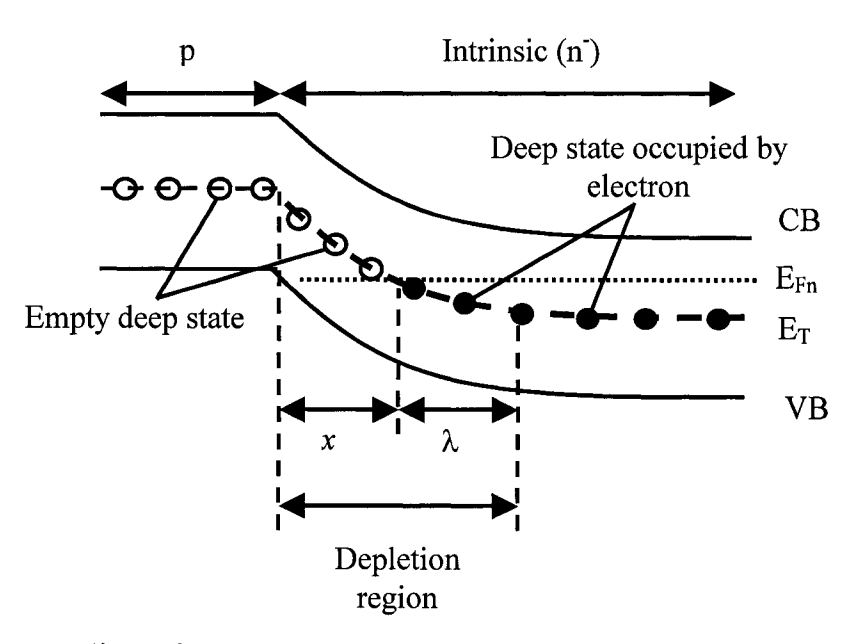


Figure 8.2: Deep state occupation in the depletion region of a PIN photodetector.

In the x region in Figure 8.2 where the deep state is resided above the quasi-Fermi level in the depletion region, the occupation density can be computed using Equation 8.7.

Assuming p and n are equal to zero in the depletion region, the deep state occupation density in the x region can be simplified to:

$$n_T = \frac{e_p}{e_n + e_p} N_T \tag{8.14}$$

In the λ region where the deep states are resided below the quasi-Fermi level within the depletion region, the deep states are mostly likely to be occupied. The length of λ can be computed if the deep state density is smaller than N_D and is expressed by:

$$\lambda = \sqrt{\frac{2\varepsilon_s(E_F - E_T)}{q^2 N_D}}$$
 (8.15)

8.1.5. TRANSIENT CAPACITANCE

Deep states can be negatively charged, positively charged or neutral depending on their status (refer to Figure 8.1). Transient capacitance measurements are ideal to measure the status of deep states. In such measurements, deep states are characterized by measuring a time-varying capacitance resulted when the bias voltage across a pn junction is changed [8.5]. The transient capacitance of a PIN photodetector with majority traps only (capture and emission of electrons) is described below:

- 1. Initially the PIN photodetector is under steady state reverse bias V_{rev} (Figure 8.3a). The depletion region in the device is w. The deep states in the region w- λ are empty.
- 2. A forward bias pulse V_{fill} is applied to the device to fill the empty deep states. The depletion region is reduced (Figure 8.3b).
- 3. The voltage drop back to reverse bias V_{rev} right after the pulse (Figure 8.3c). The depletion region extended back to its original width w in step one. But the charges

trapped in the deep states in the depletion region during the second step cannot inject back to the conduction band instantly and are remained in the deep state for a short period of time. Thus, the deep states occupation in this region is a time-dependence function in this step. This step is also known as the transient step, the deep state occupation density can be expressed as:

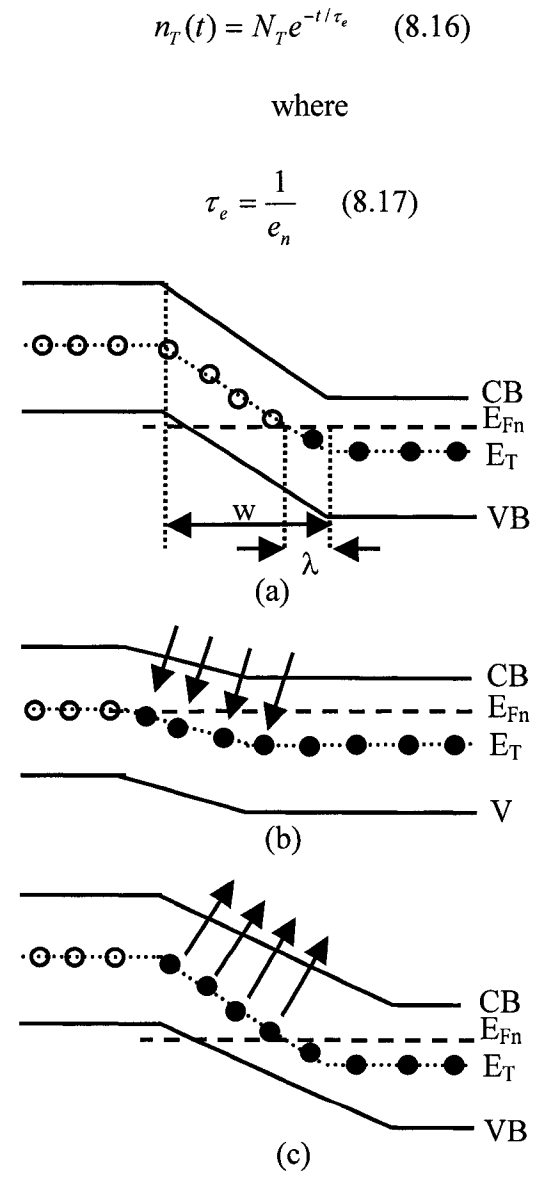


Figure 8.3: Deep state status under a) steady-state reverse bias, b) filling state and c) transient capacitance state.

The capacitance of a device is an indication of charge storage. Since the charge density in the depletion region is a time-dependence function in the transient step, thus the device capacitance is also a time-dependence function and is expressed as:

$$C(t) = C(v_{rev})[1 - \frac{N_T}{2N_D}e^{-t/\tau_e}]$$
 (8.18)

The magnitude of the capacitance transient due to n-type majority carrier emission is expressed as:

$$\Delta C_e = C(\infty) - C(0) = C(v_{rev}) \frac{N_T}{2N_D}$$
 (8.19)

Figure 8.4 shows the capacitance transient of a p⁺n and pn⁺ junction due to majority carrier emission.

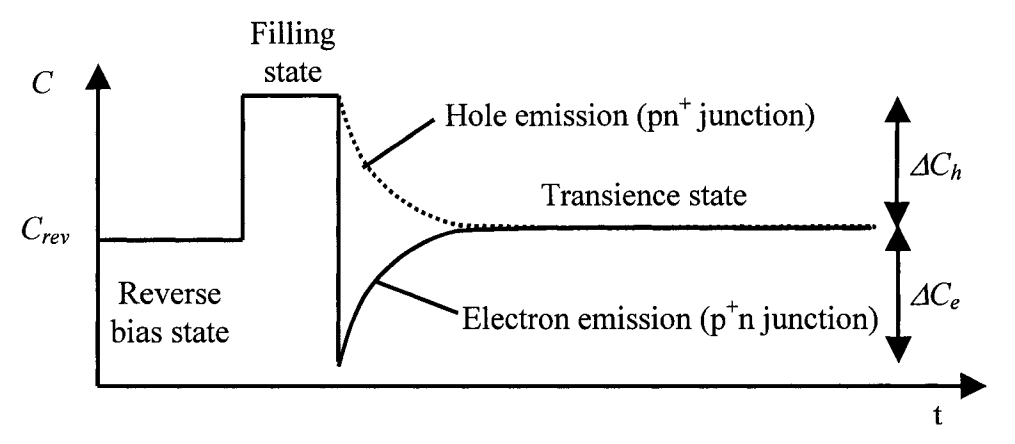


Figure 8.4: Capacitance transient due to majority carrier emission.

In a practical capacitance transient measurement, the transient capacitance may not follow exactly the exponential increases/decreases as described in Equation 8.18. There are several reasons for the non-ideal effect:

 Emission rate is electric field dependent and deep states in different areas in the depletion region emit at different rates.

- 2. Several deep state energy levels emit at the same time leads to an overlap of multiple exponentials increase in capacitance.
- 3. Deep state density is not negligible compared to the shallow level dopant concentration.

8.1.6. DEEP LEVEL TRANSIENT SPECTROSCOPY

Deep level transient spectroscopy (DLTS) is a dynamic technique which measures the transient capacitance. During the measurements, filling pulses are repeatedly applied (Figure 8.5a) while the temperature is increased/decreased at a constant rate. Since the deep state emission $e_{n/p}$ is thermally activated and the time constant of the transient will change with temperature, the shape of transient capacitance is different at different temperatures. A common method to measure the capacitance transient is the boxcar technique [8.6] (Figure 8.5b). The transient is measured between two sampling points at times t_1 and t_2 . The time period between the sampling points is referred to as the rate window. As the temperature increases, the shape of the transient changes in a manner characteristic of a particular deep state energy.

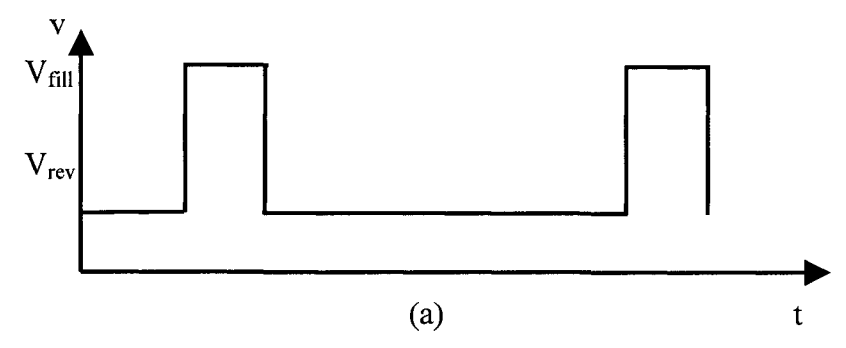


Figure 8.5s: DLTS measurement technique. The filling pulses are repeatedly applied.

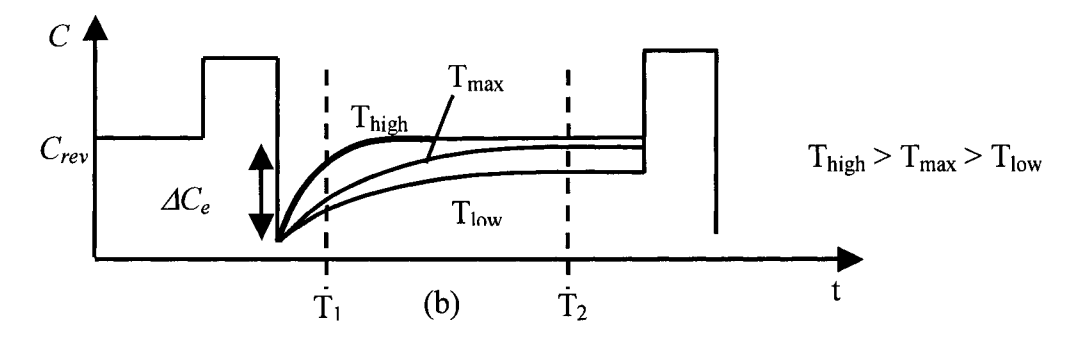


Figure 8.5b: DLTS measurement technique. The transient capacitance is measured between two sampling points at times t_1 and t_2 at different temperatures.

The capacitance transient \mathcal{E} between the sampling point t_1 and t_2 is measured and recorded as a function of temperature for a fixed rate window (Figure 8.6). \mathcal{E} can also be expressed mathematically using Equation 8.20. \mathcal{E} is small at high temperatures since all the deep states are readily ionized, and is small at low temperatures since few deep states are ionized.

$$\delta C = C(t_2) - C(t_1) = \Delta C_e \left[\exp(\frac{-t_1}{\tau_e(T)}) - \exp(\frac{-t_2}{\tau_e(T)}) \right]$$
 (8.20)

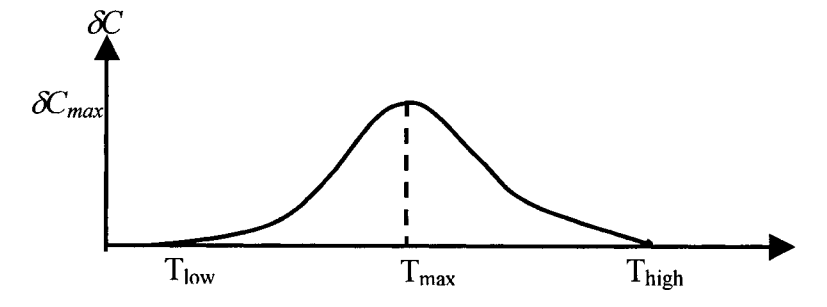


Figure 8.6: Capacitance transient δC between the sampling point t_1 and t_2 for different temperature for a fixed rate window.

The maximum transient capacitance occurs at temperature = T_{max} where the emission time constant of the deep level is:

$$\tau_e(T_{\text{max}}) = \frac{1}{e_n} = \frac{t_2 - t_1}{\ln(t_2 / t_1)}$$
(8.21)

Combining Equations 8.20 and 8.21, the relationship between ΔC_e , δC_{max} and the rate windows can be obtained and is expressed as:

$$\frac{\delta C_{\text{max}}}{\Delta C_e} = \frac{r - 1}{r^{r/(r - 1)}} \qquad (8.22)$$

where

$$r = \frac{t_2}{t_1} \quad (8.23)$$

From the DLTS measurements, one can retrieve the $\mathcal{E}C_e$ and thus the density of a particular deep state N_T can be computed using Equation 8.19. In addition, the deep state energy level can also be measured using multiple DLTS measurements at different rate windows. Sample DLTS spectra for different rate windows are shown in Figure 8.7.

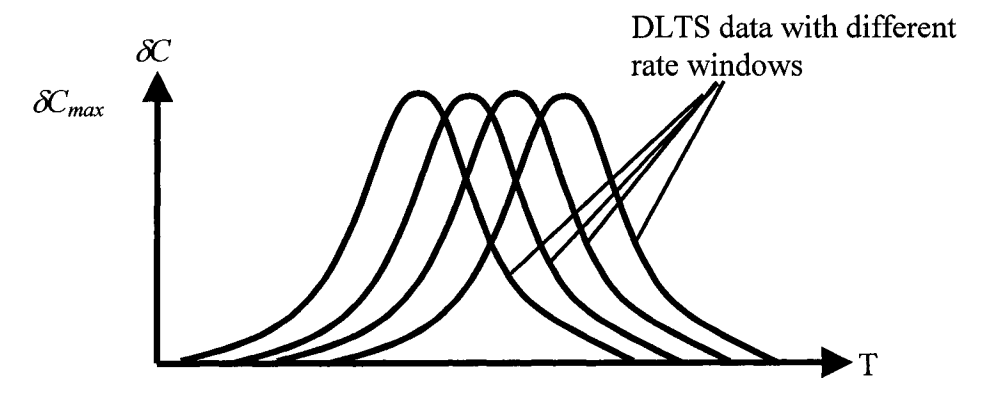


Figure 8.7: Sample DLTS spectra for different rate windows.

For each rate window, one δC_{max} and one T_{max} are obtained. Using Equation 8.21, a unique e_n for each rate window can be computed. Rewriting Equation 8.13 into Arrhenius format gives:

$$\ln(\frac{e_n}{T^2}) = \ln(\gamma_n \sigma_n) - (E_c - E_T)/kT \quad (8.24)$$

By plotting the DLTS results from different rate windows (Figure 8.8) using Equation 8.24, one can compute the deep state energy from the slope of the plot.

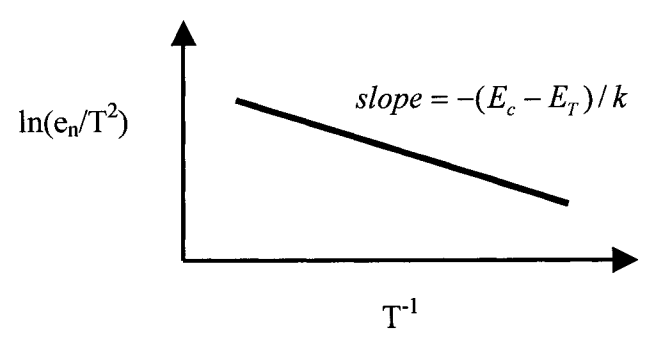


Figure 8.8: Deep state energy plot.

8.2. MEASUREMENTS

8.2.1. DLTS SYSTEM

DLTS measurements were carried out in a Polaron DL 4600 system from BIO-RAD laboratory [8.7]. The equipment integrated a Boonton 72B capacitance meter with a 100 mV test signal at a measuring frequency of 1 MHz. Four different ranges can be selected in the capacitance meter with different sensitivity. The sensitivity data is summarized in Table 8.1.

Table 8.1: Capacitance meter sensitivity data [8.8].

Range (pF)	Sensitivity (pF/100 mV)	
1 - 3	0.1	
10 - 30	1	
100 - 300	10	
1000 - 3000	100	

The capacitance meter also featured a capacitance-offset ability. By using the differential input from the capacitance meter with proper capacitance offset, the sensitivity of the measurements can be improved by choosing a smaller range. As described in section

8.1.6, the DLTS system used a boxcar approach to measure the transient capacitance. The pulse generator in the system sent three pulses to trigger the measurement in the transient state. By varying the timing sequence of these pulses, six rate windows can be obtained for the DLTS measurements. Table 8.2 summarized the timing for the six preset rate windows. Pulses t_1 and t_2 are used when rate windows A is desired and pulses t_2 and t_3 are used when rate window B is required.

Table 8.2: Pulse timing for the pre-set rate windows.

Rate window A	Rate window B	Pulse t ₁ timing	Pulse t ₂ timing	Pulse t ₃ timing
(1/s)	(1/s)	(ms)	(ms)	(ms)
1000	400	0.6	1.5	3.8
200	80	3.1	7.7	19.1
50	20	12.4	30.6	76.4

The DLTS system also featured a 12-bits signal processor to compute the measured data and a temperature controller to control the measurement temperature by adjusting the flow of liquid nitrogen to remove heat and controlling the current flow to a heater to supply heat. The DLTS system is controlled by a computer model HP9816 from Hewlett Packard Company.

8.2.2. MEASUREMENT RESULTS

InGaAs/InP PIN photodetector sample V1B-D4 was selected for the DLTS measurements due to its consistent C-V measurement results. The device had an active area of 0.09 mm², an n⁻ region doping concentration of 1x10¹⁶ cm⁻³, a reverse current of 5 nA at 6 V, and a n⁻ region width around 0.8 um. Two DLTS measurement runs were performed. The measurement setting is summarized in Table 8.3.

Table 8.3: DLTS measurement settings:

	Measurement 1	Measurement 2
Fill voltage (V _{fill})	0.2 V	0 V
Reverse voltage (V _{rev})	-2.5V	-3.5V
Fill pulses width	0.1s	0.1s
Temperature range	200 K – 300 K	200 K – 300 K
Capacitance meter range	100 pF	10 pF

In measurement 1, a small reverse bias, -2.5 V, was used. The small reverse bias was just large enough to fully deplete the intrinsic region in the PIN photodetector and without extending the depletion width into the buffer layer. In such case, only deep states in the intrinsic region will be characterized. The DLTS results from measurement 1 were shown in Figure 8.9.

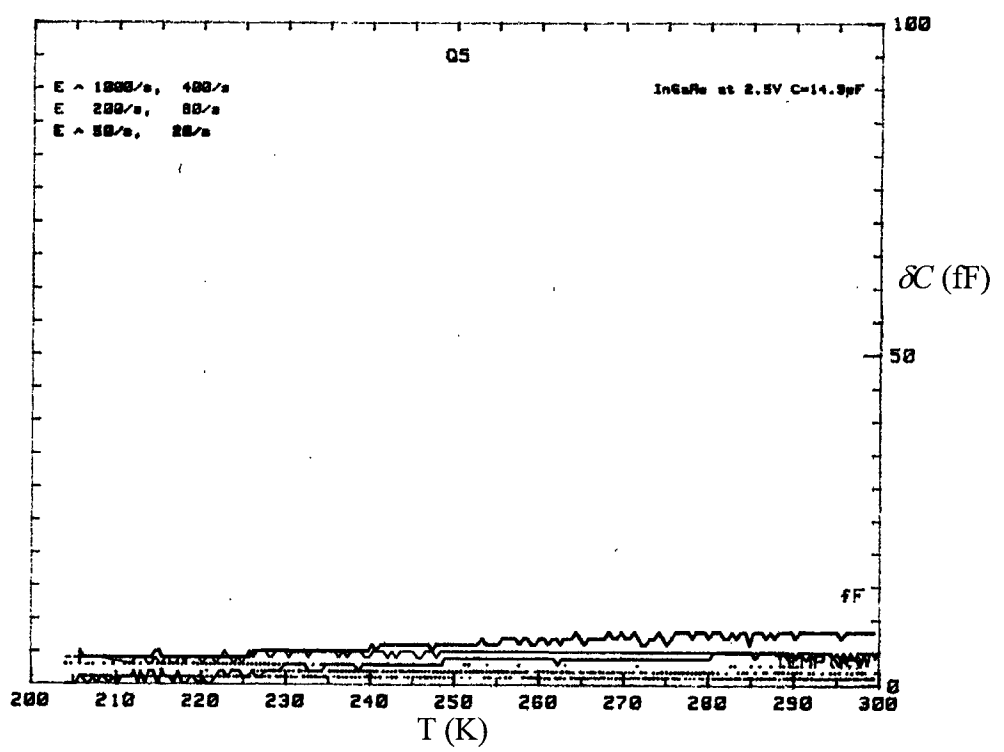


Figure 8.9: DLTS results from measurement 1.

The measured steady state capacitance under reverse bias was 14.9 pF. According to the measurement results, there was very small transient capacitance over the measured temperature range for all the rate windows. The flat data curve with no visible peak

indicated that there were no measurable majority (n type) deep states in the intrinsic, n, region of the photodetector. This close to ideal result was expected since the C-V measurements in Chapter 5 showed a smooth capacitance voltage plot.

In measurement 2, a large reverse bias, -3.5 V, was used. The used of a large reverse bias was to extend the depletion width into the InP buffer layer (refer to Figure 3.1) of the PIN photodetector. The buffer layer acts as a crystal-matching layer between the bulk InP substrate and the InGaAs epitaxy layer. Defects or deep states are likely to be found in the interfaces between the two layers or in the InP buffer layer. The DLTS results from measurement 2 are shown in Figure 8.10.

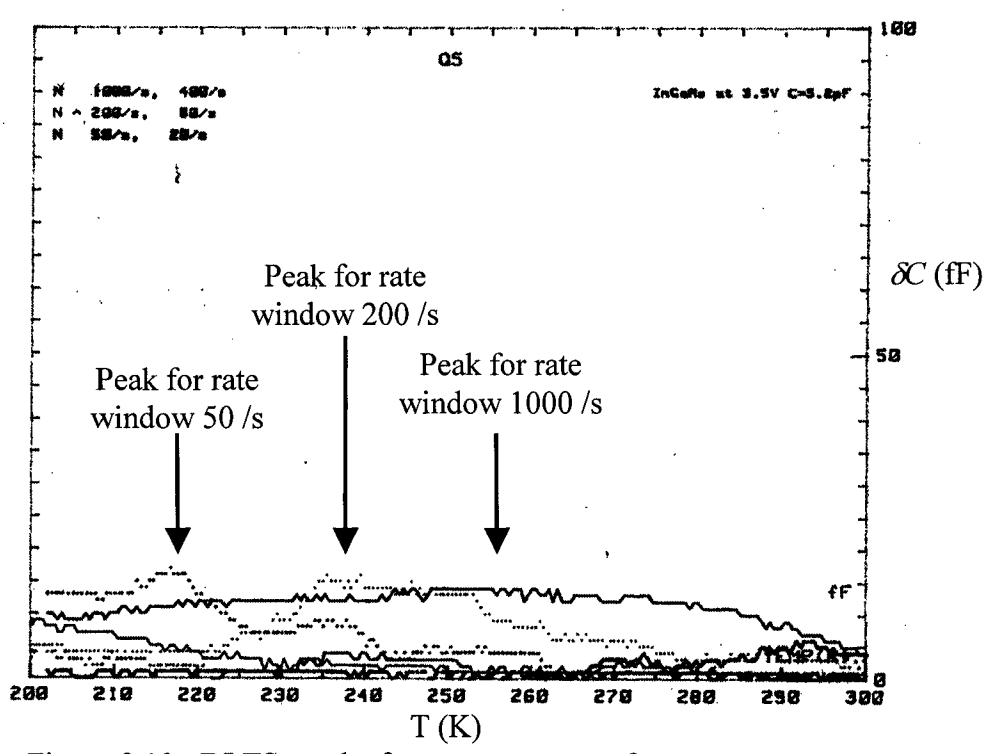


Figure 8.10: DLTS results from measurement 2.

The plot indicated that the steady state reverse bias capacitance for the device was 5.2 pF. Three capacitance transient peaks are visible at rate windows of 1000 /s, 200 /s and 50 /s and at temperature 255 K, 238 K and 218 K respectively. The maximum transient

capacitance \mathcal{E}_{max} is 15 fF for each rate window. ΔC_e was computed using the measurement data, yielding a value of 46 fF using Equation 8.22. The deep state density was computed using Equation 8.19 and had a value of 1.77×10^{14} cm⁻³. Since the doping concentration in the n⁻ region was 1.0×10^{16} cm⁻³, thus the ratio of deep state density to doping concentration in the InGaAs layer was around 1:53. The extracted data were summarized in Table 8.4.

Table 8.4: Extracted data from DLTS measurement 2.

Parameter	Value	
N_d	$1.0 \times 10^{16} \text{ cm}^{-3}$	
C _{rev} at 3.5 V	5.2 pF	
δC_{max}	15 fF	
ΔC_{e}	46 fF	
N_{T}	$1.77 \times 10^{14} \text{ cm}^{-3}$	

The energy level of deep states was also extracted based on the measurement data. The emission coefficients, C_e , corresponding to the three T_{max} were computed using Equation 8.21 and were summarized in Table 8.5. The Arrhenius plot using Equation 8.24 is shown in Figure 8.11.

Table 8.5: Emission coefficient data.

Temperature (K)	Pulse t ₁ timing (ms)	Pulse t ₂ timing (ms)	Emission coefficient, e _n
255	1.5	0.6	1.018
238	7.7	3.1	0.199
218	30.6	12.4	0.050

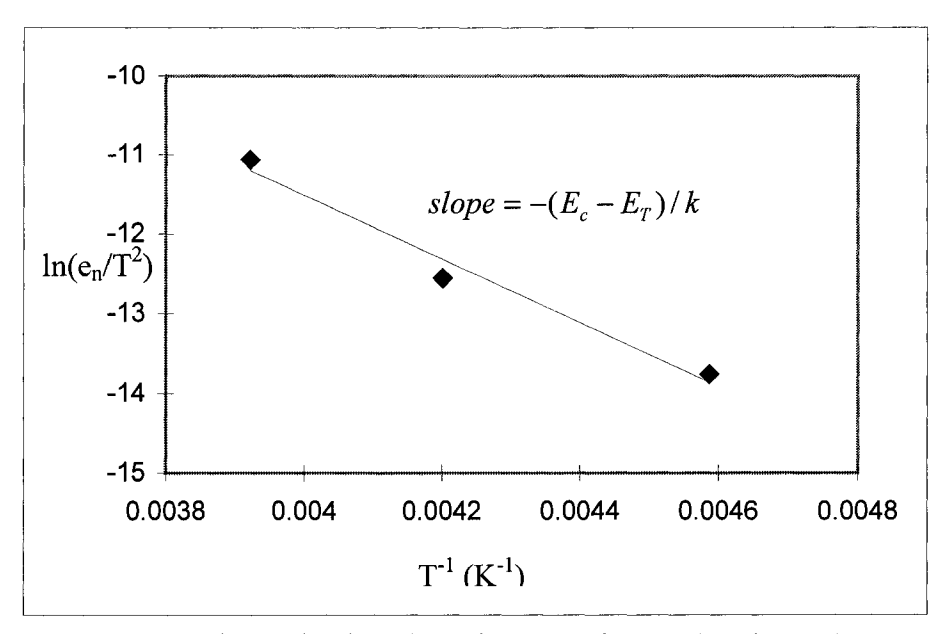


Figure 8.11: The Arrhenius plot using Equation 8.24 and DLTS measurement 2 data.

The slope of the plot is -3990. Using Equation 8.24, the E_c - E_T value was computed to be 0.34 eV, which indicated that the deep state energy levels are located 0.34 eV below the conduction band edge. These deep states could be resided at the interface between the InGaAs layer and the InP buffer layer or in the buffer layer since they were measured only when a large reverse bias was used. Similar work had been done by M. Ogura et al. [8.9]. In their work, three deep state energy levels were found at 0.17 eV, 0.37eV and 0.54 eV. The first energy level was found at the interface of the InGaAs/InP and the rest were found in the InP buffer layer. The present measurement results agreed with one of the deep state energy levels $(0.34 \text{ eV} \sim 0.37 \text{ eV})$ found in their work.

8.3. SUMMARY

In this chapter, the DLTS technique has been used to characterize the deep states in an InGaAs PIN photodetector. It was found that there are minimum measurable majority deep states in the intrinsic n region while a measurable deep states located in the InP buffer layer.

9. SUMMARY

In this thesis, several material characterization techniques were used to examine the material characteristics of InGaAs/InP PIN photodetectors. Four samples were fabricated in the laboratory and three of them were successful. All the working devices were examined using I-V and C-V measurement techniques and selected devices were used in the EBIC and DLTS measurements. In addition, a 2-dimensional simulation of excess minority carrier distribution was performed using a software package FlexPDE 3.

In the reverse I-V measurements, a small reverse current (in order of 0.1 nA) was measured in multiple devices under low reverse bias condition (< 4 V) while a slightly larger reverse current (in the order of 1 nA) was obtained under high bias (> 4 V). The measurement data suggested that reverse recombination current became significant only under high bias condition. In the forward I-V measurements, devices from sample V1A showed a smaller turn-on voltage compared to those from sample V2A. The results indicated that the doping concentration in the n⁻ region in the sample V2A was lower then that in sample V1A. All the fabricated devices showed a close to 1 ideality factor in the low forward bias region which suggested that the forward recombination current component was small and the defect density was small.

From the C-V measurement data, it was found that the doping concentrations in n⁻¹ region of sample V1A and V1B were high (close to 10^{16} cm⁻³) and it was reasonably low in sample V2A with a value in the order of 10^{14} cm⁻³. The n⁻¹ region width for the three samples V1A, V1B and V2A were 0.75 um, 0.75 um and 1.6 um respectively. The corresponding built-in voltages were 0.5 V, 0.5 V and 0.25 V.

From the EBIC measurement data, the depletion width in the device V1B-D4 was found to be 0.798 um. The value was slightly higher than that found using C-V measurement technique. It is believed that EBIC measurement method is a more accurate method and data from the C-V measurements might subject to parasitic components. The diffusion length of carriers for the photodetector was retrieved using three different methods and was in the range of 0.5 to 0.6 um. The surface recombination velocity was measured with a value of 40.2×10^6 cm/s.

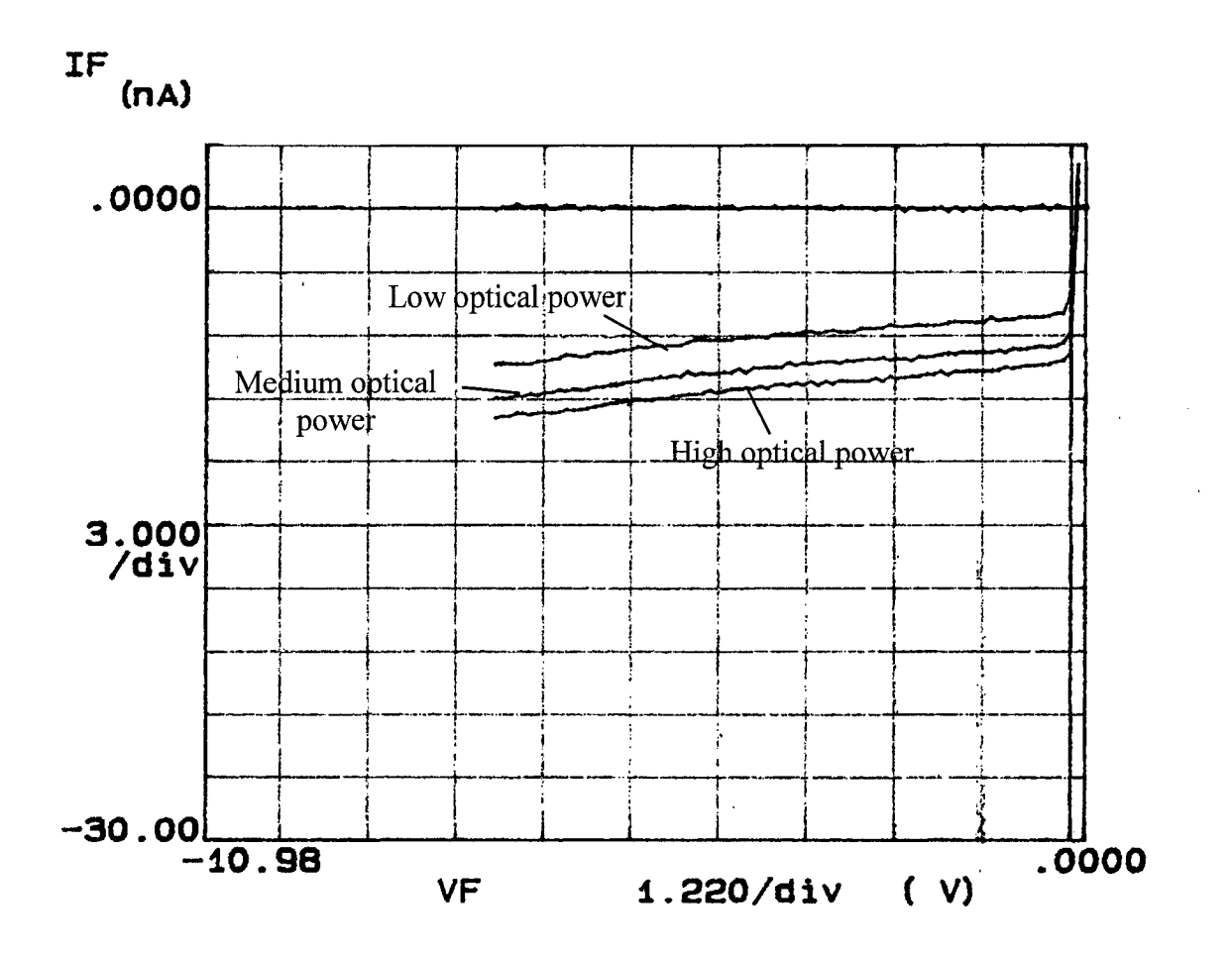
A computer simulation of the distribution of excess carrier in the p⁺ region of a PIN photodetector under illumination was performed using the software package FlexPDE 3 from PDE Soultion Inc. The excess carrier distribution was simulated according to the measured parameters. It helped to visualize the transport of carriers in the device in different regions.

From the DLTS measurement results, it was found that there were no significant majority (n type) deep states in the intrinsic n region. However, measurable majority deep states were detected in InP buffer layer. The deep state energy level was located 0.34 eV below the conduction band with a density of 1.77x10¹⁴ cm⁻³.

9.1. FUTURE WORK

Possible future work includes characterization of the optical properties of the InGaAs material such as absorption coefficient, sensitivity and responsivity at different wavelengths, quantum efficiency, noise performance...etc. Once the complete material parameters are gathered, a high-speed device with optimized device size and structure can be fabricated and the detector performance can also be characterized.

APPENDIX A: RESULTS OF REVERSE I-V MEASUREMENTS UNDER ILLUMINATION



APPENDIX B: RESULTS OF DIFFUSION LENGTH COMPUTATION USING METHOD 2

Distance x	I _{EBIC}	I _{EBIC} '	avg(I _{EBIC} ')	I _{EBIÇ} "	L=sqrt(I _{EBIC} /I _{EBIC} ")	avg L _e (um)
-1.60	3.71	-3.79	-4.36	0.00	#DIV/0!	
-1.54	3.49	-4.74	-4.36	4.51	0.85	
-1.50	3.30	-4.55	-4.18	14.21	0.46	
-1.45	3.07	-3.25	-3.47	6.19	0.68	
-1.38	2.84	-2.60	-3.03	-4.89	#NUM!	
-1.30	2.63	-3.25	-3.42	-2.26	#NUM!	
-1.23	2.41	-4.42	-3.58	-8.27	#NUM!	
-1.17	2.14	-3.08	-4.08	7.56	0.50	
-1.09	1.89	-4.74	-3.47	0.26	2.47	
-1.03	1.61	-2.60	-3.46	3.95	0.60	
-0.95	1.40	-3.03	-3.14	1.93	0.80	
-0.90	1.25	-3.79	-3.04	4.42	0.49	
-0.85	1.06	-2.32	-2.82	8.77	0.31	
-0.76	0.85	-2.37	-2.03	4.12	0.40	
-0.68	0.66	-1.42	-1.70	3.65	0.37	
-0.56	0.49	-1.33	-1.27	1.58	0.48	
-0.46	0.36	-1.05	-1.11	3.00	0.30	
-0.37	0.27	-0.95	-0.84	2.13	0.25	
-0.23	0.13	-0.52	-0.54	2.55	0.17	
-0.12	80.0	-0.16	-0.26	1.07	0.23	
0.00	0.06	-0.11	-0.13	0.44	0.29	
0.18	0.04	0.00	-0.05	0.26	0.38	
0.38	0.04					
						0.56

APPENDIX C: RESULTS OF DIFFUSION LENGTH COMPUTATION USING METHOD 3

Distance x	I _{EBIC}	In(I _{EBIC})	L=-(DIn(I _{EBIC}))^-1	avg L _e (um)
-1.60	3.71	1.31	0.95	
-1.54	3.49	1.25	0.72	
-1.50	3.30	1.19	0.70	
-1.45	3.07	1.12	0.91	
-1.38	2.84	1.04	1.05	
-1.30	2.63	0.97	0.78	
-1.23	2.41	0.88	0.51	
-1.17	2.14	0.76	0.65	
-1.09	1.89	0.64	0.37	
-1.03	1.61	0.48	0.58	
-0.95	1.40	0.34	0.44	
-0.90	1.25	0.22	0.30	
-0.85	1.06	0.06	0.41	
-0.76	0.85	-0.16	0.32	
-0.68	0.66	-0.41	0.40	
-0.56	0.49	-0.71	0.32	
-0.46	0.36	-1.02	0.29	
-0.37	0.27	-1.33	0.20	
-0.23	0.13	-2.02	0.20	
-0.12	0.08	- 2.58	0.42	
0.00	0.06	-2.87	0.44	
0.18	0.04	-3.27		
0.38	0.04			
				0.52

APPENDIX D: EXCESS CARRIER DISTRIBUTION SIMULATION CODE

```
title "P+ region of a PIN Photodetector"
definitions
               deep = 1e-4
               width = 5e-4
              openstart=1e-4
              open = 3e-4
D = 181
               S = 40.2e6
               L = 0.55e-4
               tau = 1.67E-11
              absorp = 10000
              photonflux = 7.8e17
              g = photonflux*absorp*exp(-absorp*(width-y))
variables
               n
equations
              n: div(grad(n)) + g/D - n/(tau*D) = 0
boundaries
 region 1
               start(0,0)
               line to (width,0)
               line to (width, deep)
               line to (0,deep)
               line to finish
 region 2
              start(openstart,0)
              start(openstart,0)
line to (openstart+open,0)
line to (openstart+open,deep)
line to (openstart,deep)
line to finish
Feature 1
              value(n) = 0
              start (0,0) line to (width,0)
Feature 2
              value(n)=0
              start (0,deep) line to (openstart,deep)
              start (openstart+open,deep) line to (width,deep)
Feature 3
              natural(n)=-S*n/D
              start(0,0) line to (0,deep)
Feature 4
              natural(n)=-S*n/D
              start(width,0) line to (width,deep)
Feature 5
              natural(n)=-S*n/D
              start (openstart,deep) line to (openstart+open,deep)
plots
 grid(x,y)
surface(n) Report n
contour(n)
surface(g)
vector (dx(n), dy(n))
 table(n) EXPORT FORMAT "#Y#B#X#B#1" file="data.txt"
```

REFERENCES

- 1.1) G. Keiser, "Optical Fiber Communications," 3rd edition, McGraw Hill, 2000.
- 1.2) H. Melchior, "Sensitive High Speed Photodetectors for the Demodulation of Visible and Near Infrared Light," J. Luminescence, vol. 7, pp. 390-414, 1973.
- 1.3) H. Melchior, "Detectors for lightwave communications," Phys. Today, vol. 30, pp 32-39, Nov. 1977.
- 1.4) F. Capasso, "Multilayer Avalanche Photodiodes and Solid-State Photomultipliers," Laser Focus/Electro-Optics, vol. 20, pp. 84-101, July 1984.
- 1.5) E. H. Putley, "The Pyro-Electric Detector," in R. K. Willardson and A. C. Beer, eds., Semiconductors and Semimetals, vol. 5, Academic, New York, 1970
- 1.6) S. R. Forrest, "Optical Detectors: Three Contenders," IEEE Spectrum, vol. 23, pp. 76-84, May 1986.
- 1.7) J. C. Palais, "Fiber Optic Communication (Fourth Edition)," Prentice Hall, 1998.
- 1.8) R. J. Hoss, "Fiber Optic Communications Design Handbook," Prentice Hall, 1990.
- 1.9) D. Pavlidis, "Metalorganic Chemical Vapor Deposition (MOCVD) Material Growth and Application to InP-Based Electronic Devices," 10th Intern. Conf. On Indium Phosphide and Related Materials, 11-15 May 1998, Tsukuba, Japan.
- 1.10) A. Micea, F. Alexandre, J. Decobert, L. Goldstein, J. C. Harmand, and A. Ougazzaden, "Review and Prospects for VPE, MOVPE, MBE and CBE (MOMBE) of InP and Related Materials," 0-7803-4432-4/98 IEEE.
- 2.1) C. Pollock, "Fundamentals of Optoelectronics," Irwin, 1995.
- 2.2) R. G. Smith, "Photodetectors for Fiber Transmission Systems," Proc. IEEE 68, no. 10 (Oct. 1980): 1247-53.
- 2.3) S. R. Forrest, "Optical Detectors: Three Contenders," Spectrum, 23, 76-84, May 1986.
- 2.4) M. C.Gupta, "Handbook of Photonics," CRC Press LLC, 1997.
- 2.5) P. Bhattacharya, "Semiconductor Optoelectronic Devices," 2nd Edition, Prentice Hall, 1997.
- 2.6) R. G. Seippel, "Optoelectronics," Reston, 1981.

- 2.7) S. R. Forrest, "Photodiodes for Long-Wavelength Communication Systems," Laser Focus 18, no. 12: 81-90.
- 2.8) B. C. Johnson, J. C. Campbell, A. G. Dentai, C. H. Joner and G. J. Qua, "Interaction of hole trapping and transit effects in the temporal response of InP/InGaAs p-type insulator n-type photodiodes", J. Appl. Phys. 68 (10), 15 November 1990.
- 2.9) "Application Note 1: Insights into High-Speed Detectors and High-Frequency Techniques," New Focus, <u>www.newfocus.com</u>.
- 2.10) R. A. Marsland, "Selection and Application of High-Speed Photodetectors," New Focus. Inc, the Photonics Design and Applications Handbook 1993.
- 2.11) W. Liu, "Handbook of III-V Heterojunction Bipolar Transistors," Wiley-Interscience.
- 3.1) R. C. Jaeger, "Introduction to Microelectronic Fabrication," Modular Series on Solid State Devices: Volume V," Addison-Wesley, 1988.
- 3.2) C.Y. Chang, S. M. Sze, "ULSI Technology," McGraw-Hill International Editions, Electrical Engineering Series.
- 3.3) S. Wolf, R. N. Tauber, "Silicon Processing for the VLSI Era," Volume 1 Process Technology 2nd edition, Lattice Press.
- 4.1) D. deCogan, "Solid State Devices: A Quantum Physics Approach," New York: Springer-Verlag, 1987.
- 4.2) R. F. Pierret, "Semiconductor Fundamentals (Second Edition), Modular Series on Solid State Devices: Volume I," Addison-Wesley, 1988.
- 4.3) D. A. Neamen, "Semiconductor Physics & Devices Basic Principles (Second Edition)," Irwin, 1997.
- 4.4) G. W. Neudeck, "The PN Junction Diode (Second Edition), Modular Series on Solid State Devices: Volume II," Addison-Wesley, 1988.
- 4.5) J. Vanhellemont, E. Simoen and C. Claeys, "Extraction of the Minority Carrier Recombination Lifetime from Forward Diode Characteristics," Appl. Phys. Lett. 66 (21), 22 May 1995.
- 4.6) T. Stellwag, M. Melloch, M. Lundstrom, M. Carpenter and R. Pierret, "Orientation-dependent Perimeter Recombination in GaAs Diodes," Appl. Phys. Lett. 56 (17), 23 April 1990.

- 5.1) A.M. Cowley, "Depletion Capacitance and Diffusion potential of Gallium Phosphide Schottky-barrier Diodes," J. Appl. Phys., vol. 37, no.8 p. 3024 (1966).
- 5.2) F. Perjeru, X. Bai, and M. E. Kordesch, "Electronic Characterization of n-ScN/p+Si Heterojunctions," Appl. Phys. Lett. 80 (6), 11 February 2002.
- 5.3) S. Wang, "Fundamentals of Semiconductor Theory and Device Physics," Prentice Hall Series in Electrical and Computer Engineering.
- 6.1) H.J. Leamy, "Charge Collection Scanning Electron Microscopy," J. Appl. Phys. 53(6), June 1982, R51.
- 6.2) C.W. Oatley, "The Scanning Electron Microscope Part I: The Instrument," Cambridge University, Cambridge.
- 6.3) Cohn, G. Caledonia, "Spatial Distribution of the Fluoresceent Radiation Emission Caused by an Electron Beam," J. Appl. Phys. 41(9), August 1970, pp. 3767-3775.
- 6.4) V.E. Cosslett, R.N. Thomas, Brit. J. Appl. Phys. 15, 1283, 1964.
- 6.5) B.E. Schumacher, in First International Conference on Electron and Ion Beam Science and Technology, edited by R. Bakish (Wiley, New York, 1965), pp. 5-70.
- 6.6) E. Gruen, "Lumineszenz-photometrische Messungen der Energieabsorption in Stralungsfeld von Electronenquellen: Eindimensionaler Fall in Luft," Z. Naturforsch. 12A, 89-95. 1957.
- 6.7) T.E. Everhart, P.H. Hoff, "Determination of Kilovolt Electron Energy Dissipation vs Penetration Distance in Solid Materilas," J. Appl. Phys. 42(13), December 1971, pp. 5837-5846.
- 6.8) R.d. Birkhoff, "in Handbuch der Physik," edited by E. Fluegge, (Springer, Berlin 1958). Eqs. (7.10) and (8.1).
- 6.9) M.J. Berger, S.M. Seltzer, Nat. Acad. Sci. -Natl. Res. Concil Publ. No. 1133 (1964), pp 205.
- 6.10) E. Miyazaki, K. Miyaji, "Enhancement of Reverse Current in Semiconductor Diodes by Electron Bombardment," Jpn. J. Appl. Phys. 2, 129-130.
- 6.11) M. Gallant, A. Zemel, "Photocarrier Spreading at a p-n Junction," J. Appl. Phys. 78 (8), 15 April 1993.
- 6.12) J. Wu, D. B. Wittry, "Investigation of Minority-carrier Diffusion Lengths by Electron Bombardment of Schottky Barriers," J. Appl. Phys. 49 (5), May 1978.

- 6.13) R. Hakimzadeh, S. G. Bailey, "Minority Carrier Diffusion Length and Edge Surface-Recombination Velocity in InP," J. Appl. Phys. 74, 1118 (1993).
- 6.14) V. K. S. Ong, D. Wu, "Determination of Diffusion Length from Within a Confined Region with the use of EBIC," IEEE Trans. on Electron Devices, VOL. 48, NO. 2, February 2001.
- 6.15) L. L. Keung, O. V. Roos, L. J. Cheng, "Quantification of the effects of generation volume, surface recombination velocity, and diffusion length on the electron-beam-induced current and its derivative: Determination of diffusion lengths in the low micron and submicron ranges," J. Appl. Phy. 57 (6), 15 March 1985.
- 6.16) W. Shockley, W. T. Read Jr., "Statistics of the Recombination of Holes and Electrons," Physical Review 87, no. 5 (September 1, 1952), pp. 835-42.
- 6.17) M. Watanabe, G. Actor, H. C. Gatos, "Determination of Minority-Carrier Lifetime and Surface Recombination Velocity with High Spacial Resolution," IEEE Trans. on Electron Devices, VOL. ED-24, No. 9, September 1977.
- 7.1) S. P. Wilson, S. J. Woods, A. B. Walker, "Modelling of PIN Photodiodes Under High Illumination Conditions," Int. J. of Numerical Modeling: Electronic Networks, Devices and Fields, Vol. 10, 139-151 (1997).
- 7.2) D. Levy, S. E. Schacham, "Three-Dimensional Excess Carrier Distribution in Semiconductor Imaging Arrays," J. Appl. Phys. 64(10) 15 Nov 1988.
- 7.3) P. D. Yoder, "Physical Modeling of High-Speed PIN Photodetectors," Proceedings of SPIE vol. 4283 (2001).
- 7.4) PDE Solutions Inc. (www.pdesolutions.com).
- 7.5) J. Gowan, "Optical Communication System," 2nd edition, Prentice Hall.
- 8.1) "DLTS, Its Role in Semiconductor Materials and Device Assessment," Application notes from Polaron Equipment Ltd.
- 8.2) D.V. Lang, "Deep-Level Transient Spectroscopy: A new method to characterize traps in semiconductors," J. Appl. Phys., Vol. 45, No. 7, July 1974.
- 8.3) B. G. Streetman, "Solid State Electronic Devices," 3rd edition, Prentice Hall International Editions, 1990.
- 8.4) R. F. Pierret, "Advanced Semiconductor Fundamentals (Second Edition), Modular Series on Solid State Devices: Volume VI," Addison-Wesley, 1988.

- 8.5) "Standard Test Method for Characterizing Semiconductor Deep Levels by Transient Capacitance Techniques," ASTM, Designation: F978 86, 27 March, 1986.
- 8.6) I. C. Mayes, M. N. Robinson, "An Introduction to Deep Level Transient Spectroscopy", Dio-Rad Semiconductor Notes, no401, May, 1987.
- 8.7) Bio-Rad laboratory: http://www.bio-rad.com
- 8.8) "DL4600 Deep Level Transient Spectrometer Operation Manual", Polaron Equipment Ltd.
- 8.9) M. Ogura, M. Mizuta, K. Onaka, H. Kukimoto, "A capacitance investigation of InGaAs/InP isotype heterojunction," J. J. Appl. Phys, vol.22, no.10, Oct 1983.